A New Strain Gage Technique for the Accurate Determination of Mode-I Notch Stress Intensity Factors of Sharp V-Notches

A Thesis submitted

In Partial Fulfilment of the Requirements

for the Degree of

DOCTOR OF PHILOSOPHY

by

Pranjol Paul

(10610302)

Department of Mechanical Engineering

Indian Institute of Technology Guwahati

Guwahati-781039, India

October, 2024

Certificate

It is certified that the work contained in the Thesis entitled "**A New Strain Gage Technique for the Accurate Determination of Mode-I Notch Stress Intensity Factors of Sharp V-Notches"** submitted by **Pranjol Paul** to the Indian Institute of Technology Guwahati for the award of the degree of Doctor of Philosophy has been carried out under our supervision in the Department of Mechanical Engineering, Indian Institute of Technology Guwahati. This work has not been submitted elsewhere for the award of any other degree.

(K. S. R. Krishna Murthy)
Professor
Department of Mechanical Engineering
Indian Institute of Technology Guwahati
Guwahati-781 039

(Debabrata Chakraborty)
Professor
Department of Mechanical Engineering
Indian Institute of Technology Guwahati
Guwahati-781 039

Dedicated to my spiritual mentor

Sri Sri Thakur Anukul Chandra ji

and

my parents

Mr. Bivash Chandra Paul and Ms. Annapurna Paul

Acknowledgements

This thesis is the outcome of my research work done in the Department of Mechanical Engineering, IIT Guwahati. The exercise was by no means an easy task and during this long period, I have been guided and supported by many people. My heartfelt acknowledgements are dedicated to all of them for their valuable help at various stages during this tenure. I, now, have the opportunity to acknowledge my gratitude to all of them.

At the outset, I wish to express my profound gratitude to my spiritual mentor **Sri Sri Thakur Anukul Chandra ji** who has been the consistent source of my inner strength and overall patience which helped me cope with all circumstances during this toilsome academic journey and kept me focused throughout.

I would like to express my sincere gratitude particularly to my supervisors **Dr. K.S.R. Krishna Murthy and Dr. Debabrata Chakraborty,** Department of Mechanical Engineering, IIT Guwahati, for their consistent academic guidance, valuable advice, motivation and strong support that shaped my work and helped me complete the same successfully.

I would like to offer my sincere thanks to my doctoral committee members, Prof. P. S. Robi, Prof. S. K. Kakoty and Prof. K. D. Singh for their valuable suggestions and needful recommendations.

My sincere appreciations are expressed to all the faculty members of the Mechanical Engineering Department, IIT Guwahati in general and the Head of the Mechanical Engineering Department in particular for providing a conducive environment to me for pursuing my research work. I am grateful to the entire technical staff of Central Workshop, IIT Guwahati for their help in specimen preparation on certain occasions. I would like to sincerely thank Mr. Jiten Basumatary, Sr. Technical Superintendent in the Advanced Manufacturing lab, IIT Guwahati for helping me fabricate my experimental specimens with the help of the CO_2 Laser cutting facility. I would like to sincerely thank Mr. Sanjib Sarma, Sr. Technical Superintendent in SOM lab, IIT Guwahati for his technical guidance while conducting the experiments. I would like to sincerely thank Mr. Nip Bora, Sr. Technical Superintendent, Seminar Hall In-Charge, Mechanical Engineering Department, IIT Guwahati for facilitating me with

technical setup during the progress seminars and other presentations. I would like to thank Dr. Rituraj Saikia, Technical Officer (Gr-I), Mechanical Engineering Department, IIT Guwahati, for encouraging me always. I am also thankful to my colleagues namely Mr. Amal Kalita (Technical Officer Gr-II), Dr. Dhruba Jyoti Bordoloi (Technical Officer Gr-II), Mr. Jyotirmoy Kakati (Technical Officer Gr-II), Mr. Monuranjan Dowarah (Technical Superintendent) and Mr. Saiffuddin Ahmed (Technical Superintendent) for their needful cooperation. In addition, I would like to thank Dr. Sushen (alumnus), Dr. Sajith (alumnus), Dr. Mirzaul (alumnus), Dr. Debaleena (alumnus), Dr. Shukla (alumnus), Mr. Anurag (alumnus), Mr. Ankan Hazra and other research scholars with whom I could discuss and share my research related issues.

I wish to express sincere gratitude to the Department of Mechanical Engineering and Academic Affairs Section, IIT Guwahati for giving me the privilege of pursuing my doctoral research at IIT Guwahati.

I wish to express my warm gratitude to my parents for their blessings and consistent moral support. In addition, I wish to express my sincere gratitude to my siblings, Mr. Bijitesh Paul (elder brother) and Ms. Bornali Paul Deb (younger sister), Ms. Baisakhi Dey Paul (spouse) and Mr. Souryadipi Deb (brother-in-law) for their needful cooperation. In addition, I would like to express my gratitude to Master Paritosh Paul (son), Ms. Sambita Deb (niece) and Master Soumyadeep Deb (nephew) whose existence always used to boost my spirits.

October 2024

IIT Guwahati Pranjol Paul

Table of Contents

Abstract

Many engineering components frequently feature stress raisers such as sharp V-notches, rounded tip V-notches, and re-entrant corners etc. affecting their static and fatigue load-carrying capacities, and leading to sudden fracture in components made of brittle and quasi-brittle materials. Amongst these notches, sharp V-notch has the strongest singularity. Many varieties of notches and defects can be modelled as sharp V-notch to obtain conservative solutions. Notch stress intensity factor (NSIF) of a sharp V-notch is a vital parameter in notch fracture mechanics whose limiting value is frequently used in assessing the fracture of V-notched components. The accuracy of NSIF values acts as a regulatory aspect for appropriately making use of principles of linear elastic fracture mechanics in predicting and preventing aforesaid failures.

Three approaches are generally available to estimate the NSIFs, viz., analytical, numerical, and experimental methods. Analytical or theoretical methods are generally restricted to simple configurations, while numerical and experimental methods are widely used in more complex configurations. Experimental methods also play an important role in the validation of analytical and numerical solutions. Amongst the available experimental methods, the strain gage techniques due to their associated advantages are frequently employed in experimental fracture mechanics.

However, in using strain gage techniques, several difficulties were identified by the researchers like (a) effects of three-dimensional (3D) stress-strain state (b) plasticity effects (c) strain gradient effects near the notch tip/crack tip, and (d) lack of methods for valid locations of strain gages for the accurate sampling of surface strains. Although significant contributions have been made for cracked specimens addressing these issues, only a few strain gage techniques are currently available for the sharp V-notched configurations, which are complex to implement, require a large number of gages, and are also affected by the above challenges. Therefore, a simple, efficient, and rugged strain gage technique specifically with a procedure to identify the valid gage locations is needed in view of the role of experimental methods in the notch fracture mechanics.

Thus, in the present work, for the first time a robust strain gage technique with an assessment procedure for the valid gage locations has been proposed for the accurate

determination of mode I NSIFs in sharp V-notched configurations made of homogeneous and isotropic materials under plane stress conditions, where only a single strain gage is sufficient. To achieve this, strains in an intermediate zone are represented as a multi-parameter strain series comprising of one singular term and a few non-singular higher-order terms of Williams' eigenfunction expansion. For accurate NSIF determination, it is important to know the proper or valid radial location of this single strain gage beforehand. Such a provision clearly avoids plasticity effects, three-dimensional (3D) effects, and strain gradient effects that are known to appear near the tip of a crack or sharp V-notch. The present work also proposes a theoretical and computational framework on the existence and estimation of the valid strain gage radial locations for accurate measurement of the NSIFs of sharp V-notches. The suggested procedure clearly indicates whether a chosen gage location is valid or invalid.

In order to validate the efficacy of the proposed single strain gage technique and to demonstrate the existence and usefulness of the valid strain gage locations, a series of experiments and finite element analyses have been carried out in the present investigation using different V-notched configurations. The valid or invalid radial gage locations given by finite element analyses have been substantiated by comparing the accuracy of mode I NSIFs obtained from experiments carried out on different sharp V-notched specimens made of PMMA (Polymethylmethacrylate) material. These NSIFs have been determined using the proposed single strain gage technique with gages located at the recommended radial locations given by the proposed approach.

Results from the present investigation clearly show that there exists a minimum and a maximum radial distance for pasting a strain gage. Pasting a strain gage in this range (valid location) only ensures the accurate determination of mode I NSIFs for sharp V-notched components. Results also revealed that pasting a strain gage outside this range resulted in a highly erroneous mode I NSIF. It was also observed that these bounds depend on the configurations of the V-notch and on the specimen thickness. Thus, the present work provides for the first time a simple and efficient strain gage technique with appropriate gage locations to the analysts in the field of experimental notch fracture mechanics for the accurate determination of the NSIFs.

Nomenclature

Latin Characters

a	notch length
$A'_n (n = 1, 2, 3, ...)$	complex Williams' coefficients of notch tip asymptotic field for mode I case
$A_n (n = 1, 2, 3, ...)$	real part of A'_n
$A^*_n (n = 1, 2, 3, ...)$	imaginary part of A'_n
A_0	Williams' coefficient corresponding to the rigid body motion
A_1	Williams' coefficient corresponding to the first term of the infinite series
A, B	constants related to the finite element displacements of the notch tip elements along the notch flanks
b	width of the notched plate
C_1	constant associated with notch opening displacement
E	Young's modulus
F_I	normalized mode I NSIF
$f_{ij}^{(I)}(\theta), f_{ij}^{(II)}(\theta), f_{ij}^{(III)}(\theta)$	angular functions that only depend on θ and loading mode
$F(a / w)$	form factor or normalized NSIF
G	shear modulus of rigidity
h	represents the height of the plate
K^V	generalised notch stress intensity factor

K_C^V	critical value of K^V
$K_I^V, K_{II}^V, K_{III}^V$	notch stress intensity factor of sharp V-notches under mode I, mode II and mode III
K_{IC}^V	critical value of K_I^V
L_N	length of the notch tip element
N	shape function of a finite element
r	radial distance from the notch tip
R	residual between the analytical notch opening displacement and the finite element notch opening displacement
r_{op}	optimum radius corresponding to the point substitution method
$r_{\min}$	minimum permissible radial distance of strain gage
$r_{\max}$	maximum permissible radial distance of strain gage
$[R]$	Reuter's matrix
t	thickness of notched plate
T_z	out-of-plane constraint factor
T_{z0}	value of T_z exactly at notch tip
$[T]$	transformation matrix
u, v	displacement components near the notch tip in the x and y directions respectively
u_R	integration constant representing rigid body translation part of the u-displacement field in the mode I loading

v^{FE}	finite element displacement near the notch tip
w	half of the width of the notched plate (this notation is used for 3D analysis)

Greek Characters

α	parameter associated with notch angle
β, θ	orientation angle of strain gage and orientation angle of gage line
ρ	notch tip radius/notch root radius
κ	Kolosov's constant
ν	Poisson's ratio
γ	included angle of the V-notch (also termed as notch angle)
θ	angular coordinate
σ	far field stress
σ_∞	remotely applied load
σ_x, σ_y	direct or normal stress components near the notch tip in Cartesian coordinate system
σ_r, σ_θ	direct or normal stress components near the notch tip in polar coordinate system
τ_{xy}	in-plane shear stress in Cartesian coordinate system
ϕ	Airy stress function
ε_a	normal strain along the longitudinal direction of strain gage

$\varepsilon_x, \varepsilon_y, \gamma_{xy}$	Strain components in Cartesian coordinate system
$\lambda_n'(n=1,2,3,...)$	complex eigen values for mode I case
$\lambda_n(n=1,2,3,...)$	real part of λ_n'
$\lambda_n^*(n=1,2,3,...)$	imaginary part of λ_n'
λ_1	first eigenvalue (i.e.,eigenvalue of the first term of the infinite series)
Δv	analytical notch opening displacement
Δv^{FE}	finite element notch opening displacement
(ξ,η)	natural coordinate system

Abbreviations

2D	two-dimensional
3D	three-dimensional
CNT	sharp center V-notched tensile configuration
DENT	sharp double edge V-notched tensile configuration
EPFM	elastic-plastic fracture mechanics
EPNFM	elastic-plastic notch fracture mechanics
FE	finite element
FEA	finite element analysis
FT	fracture toughness
LEFM	linear elastic fracture mechanics
LENFM	linear elastic notch fracture mechanics

LSY	large scale yielding
NE	number of elements in finite element mesh
NN	number of nodes in finite element mesh
NSIF	notch stress intensity factor
NOD	notch opening displacement
NTOD	notch tip opening displacement
NFT	notch fracture toughness
PMMA	polymethylmethacrylate
Q8	eight nodded isoparametric quadrilateral element
Q20	twenty nodded isoparametric quadrilateral element
%Rel. error	Percentage relative error in normalized NSIF F_I
SENT	sharp single edge V-notched tensile configuration
SIF	stress intensity factor
SSY	small scale yielding
SCB	semi-circular bend
SDZ	singularity dominated zone

This page is left blank intentionally

List of Figures

This page is left blank intentionally

List of Tables

This page is left blank intentionally

Chapter 1

Introduction

This chapter briefly introduces the background of notch fracture mechanics, the importance of notch fracture mechanics based design and the significance of accurate determination of notch stress intensity factor (NSIF) in design of engineering components. Eventually, the importance of valid location of strain gage in accurate determination of NSIF has been discussed in outlining the motivation of the present research work.

1.1 Fracture mechanics

Engineering components or structures are designed so that the maximum working stress is significantly lower than the material's design stress. The conventional strength-based design approach assumes that structure to be designed should not have cracks or flaws, and the design criterion only requires the calculated maximum stress to be less than the relevant strength of the material of the component appropriately reduced by the factor of safety. However, the above approach is inadequate, because structures may possess existing defects and flaws such as cracks, dislocations or impurities, etc., or they may have sharp corners, notches, or holes. These defects act as stress raisers or stress concentration zones. Such high stress concentration zones are often susceptible to crack initiation and propagation. Once a structure or component attains a sufficient applied load, depending on the material, they experience brittle fracture failure. Brittle fracture is a catastrophic failure mode with relatively less consumption of energy and occurs very often in brittle materials (e.g., ceramics), high-strength metallic materials (due to their low ductility) and ductile materials at low temperatures. Contrary to ductile fractures, brittle fractures generally occur at stress levels much lower than the expected levels and also occur much before the expected service life of a component. History has revealed that such failures always resulted in a great loss of human lives and capital investments.

Many devastating brittle fracture failures of major structures such as bridges, ships, aircraft, pipelines, and tanks have happened in past as a result of flaws in the structures, leading not only financial losses but also the loss of many human lives. A few infamous historical brittle fracture failures include the fracture of World War II's Liberty ships and several tankers, the fatigue failures of the De Havilland Comet aircrafts (1952 to 1954) due to the disintegration of pressurized cabin in the mid-air causing many casualties, the explosion of a liquid natural gas storage tank that took place in Cleveland in 1944 killing many people. In 1938, the welded Hasselt Bridge across the Albert Canal in Belgium suddenly collapsed and fell into the water. Further, two bridges, namely the Kings Bridge in Melbourne, Australia, and the Point Pleasant Bridge at Point Pleasant, West Virginia, in the US collapsed due to brittle fractures, costing many lives in the years 1962 and 1967 respectively.

Apart from the above typical cases, many disasters involving the failure of pipes, weapons, tanks, ships, railways, and aerospace structures occurred worldwide. All those failures essentially led to the development of a new subject known as ***Fracture mechanics*** which deals with fracture of engineering materials due to cracks. A crack can be envisaged as a fine slit with zero radius of curvature at its tip. It has been observed that most of these cracks originated from stress concentration zones or stress raisers such as notches and corrosion pits etc. Thus, the subject of fracture mechanics assumes that a structure or component contains crack(s) of sufficient length before it is subjected to service loads.

The first significant work in the development of fracture mechanics was the work of Inglis [1] which discussed the stress analysis of an elliptical hole in an infinite linear elastic plate and, the degeneration of the elliptical hole into a sharp crack. Using this work, Griffith [2] put forward an energy balance approach to study the brittle fracture phenomenon in cracked bodies. This could be considered as the first solution to understand the effect of crack length on the strength of a structure using continuum mechanics' approach. However, the development of fracture mechanics as an engineering discipline was mainly due to the contributions of Irwin and his co-workers [3] at the Naval Research Laboratory, Washington DC. In addition, the linear elastic analysis of cracked bodies in two-dimensions (2D) by Westergaard [4] and Williams [5] were also important milestones in the development of modern fracture mechanics. Based on the linear elastic analysis of cracked bodies in 2D by Westergaard [4] and

Williams [5], another turning point in the history of fracture mechanics was put forward by Irwin [6]. He showed that the displacements, strains and stress components near a crack tip could be described by a single parameter known as the stress intensity factor (SIF) which can be related to the strain energy release rate. Thus, SIF K became an important parameter in the linear elastic fracture mechanics (LEFM) to deal with the control and prevention of brittle fractures.

Fracture mechanics studies can be classified into two broad divisions viz., brittle fracture and ductile fracture, depending on the ability of the material to undergo plastic deformation before fracture. In brittle fracture, crack grows with little or no plastic deformation of the material ahead of a crack tip. In this type of fracture, the existing crack propagates very rapidly at the critical load, and complete failure of the structure occurs without giving any prior warning. Brittle fracture occurs in brittle and high-strength metallic materials. On the other hand, ductile fracture (also known as fibrous fracture or dimpled rupture) involves large plastic deformation of the materials at the crack tip, thus it will always have some amount of stable crack growth before reaching the unstable state.

1.2 Notch fracture mechanics

Fracture mechanics (mechanics of solids under the presence of cracks) is widely used in aerospace, naval, shipbuilding, nuclear, locomotive, armament technology, pressure vessel, and other industries. Practically, many engineering components contain geometric discontinuities (notches etc.) which act as stress concentration zones and very often these discontinuities are provided to ensure certain intended functions. Thus, although such notches are useful, however, they become a potential site for the origin of cracks [7-10]. Figure 1.1 shows two examples of fractures due to the presence of notches. Fracture mechanics introduces the essential concept of fracture toughness, which quantifies a material's resistance to the propagation of an existing crack.

(a)

(b)

Figure 1.1 (a) Failure of a bolt because of initial failure in thread root (Reitz [11]); (b) Crane gearbox failure (Reed [12]).

An important and evolving branch of fracture mechanics is the ***notch fracture mechanics***, which deals with the crack initiation and subsequent fracture phenomenon at various types of notches. This branch is an extension of the principles of the classical fracture mechanics of cracked bodies to the notched bodies and facilitates the notches being studied using the principles of notch fracture mechanics. Many of these notches are modelled as the sharp V-notch, rounded or blunt V-notch, U-notch and keyhole type notches, etc. Blunt V-notches with negligible notch tip radii are can be considered as a sharp V-notch.

Figure 1.2 shows schematic diagram of a V-notch and U-notch. Based on the root radius ρ, V-notches are classified into sharp V-notches and blunt or rounded V-notches, as shown in Figs.1.2(a) and 1.2(b), respectively. If ρ (Fig.1.2(b)) is significantly smaller than the length of a notch sides then it is known as a sharp V-notch or else it is considered as a blunt V-notch or rounded V-notch. Here, γ is the notch opening angle of the V-notches, ρ is the root radius of the blunt V-notch, and r_u is the radius of the U-notch. Thus, a crack can be visualized as a sharp V-notch having $\gamma = 0°$.

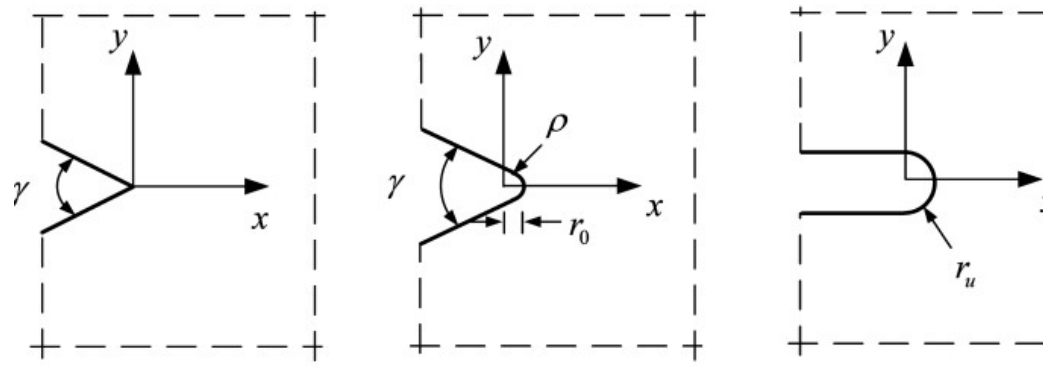

(a) **(b)** **(c)**

Figure 1.2 Schematics of (a) a sharp V-notch; (b) a blunt V-notch; (c) a U-notch.

Amongst the various notch shapes as shown in Fig.1.2, the sharp V-notch (Fig. 1.2(a)) has the strongest singularity than the other two (Figs.1.2(b) and 1.2(c)) and it gained more attention due to this severe singularity at its tip. As a consequence, the V-notched bodies are more prone to brittle fracture. In actual practice, V-notches are present in many machine components, such as root of a gear tooth, threads of screws and bolts, etc., to serve certain intended functions (Fig.1.3). On the other hand, V-notches also show up due to the nature of certain manufacturing methods [13-15]. Further, welded joints are also usually modelled as the V-notches [16-18] for meaningful results.

(a) **(b)**

Figure 1.3 Examples of V-notches (a) Bolt; (b) Gear.

Defects or flaws in many situations in an engineering component do not exactly resemble the theoretical crack. However, treating these defects as sharp cracks will provide excessively conservative solutions which is not desirable in the modern design of engineering components. Therefore, these defects are usually modelled as the sharp V-notches for conservative results. As stated earlier, a crack is a special case of the sharp V-notch with a notch angle $\gamma = 0°$. Therefore, developing new methods and extending existing methods of computing fracture parameters of a crack to a notch is highly relevant. This will encourage designers and analysts to compute fracture parameters of any general case of stress intensity, including the cracks.

Cracks originate from notches due to the high stress concentration at these zones. The nucleated crack thus propagates rapidly or slowly depending on the brittleness or ductility of materials under operational loads and finally leads to fracture failure. Therefore, it is of great interest to know the critical loads at which the crack initiation from a notch takes place. The theories that predict this critical load are known as brittle fracture criteria of the notches. It should be noted here that the conventional fracture mechanics deals only after a crack reaching a detectable size and it does not pay attention towards the conditions for the crack onset from the notches. In recent times, the notch fracture mechanics principles have been utilized to provide an answer to the above issue.

The basis of notch fracture mechanics is the pioneering work of Williams [19] on sharp V-notches. His eigenfunction expansion method provides stress analysis of a sharp V-notched 2D body subjected to arbitrary in-plane loading. Later it was extended to the three-dimensional (3D) configurations by Hartranft and Sih [20, 21]. Williams [19] examined the stress fields in the vicinity of a sharp V-notch for different boundary conditions and found that stresses at a sharp V-notch tip become infinite under all loading conditions. Further he also showed that the strength of the singularity depends only on the notch angle.

1.3 Notch fracture mechanics parameters

Fracture mechanics analyses have been classified into two divisions viz., linear elastic fracture mechanics (LEFM) and elastic-plastic fracture mechanics (EPFM). Likewise,

the notch fracture mechanics analyses can also be classified into linear elastic notch fracture mechanics (LENFM) and elastic-plastic notch fracture mechanics (EPNFM). LENFM is applicable under small scale yielding conditions (SSY). In these conditions, the plastic zone size at the notch tip is significantly smaller than the notch length and other associated geometric dimensions. The stress-strain behavior and load-displacement behavior is essentially linear in LENFM. Here, linear elastic analysis of notched bodies is typically carried out to obtain displacement and stress fields. As the plastic zone size is small at the notch tip in LENFM, the effects of the plastic deformation of notched components during the crack initiation are normally ignored. Most of the engineering designs based on the notch fracture mechanics approach are hooked to the brittle fracture involving brittle materials and high-strength materials with low fracture toughness.

EPNFM is very useful under large scale yielding (LSY) conditions as in the case of highly ductile materials used in the nuclear industry. This approach is mainly useful where the plastic zone size is proportionate to the notch length and other geometrical dimensions. Because of the presence of more plastic deformation, the specimens under LSY conditions will require more amount of energy for the crack initiation from the notch tip compared to the specimens under SSY conditions.

Based on whether LENFM or EPNFM is employed, various fracture parameters of the sharp V-notch are viz., energy release rate, notch stress intensity factor (NSIF), notch tip opening displacement (NTOD) and $J-$ integral. An appropriate parameter is chosen to analyse the given notch problem based on material and the notch tip conditions. The energy release rate G and NSIF, K^V are used in the LENFM analysis. The parameter K^V is more popular and widely employed in the LENFM than the parameter G. On the other hand, the $J-$ integral and NTOD are useful in the EPNFM studies. One can easily see that these parameters are derived from the crack problems of classical fracture mechanics.

1.4 Notch stress intensity factor (NSIF)

The notch stress intensity factor, K^V (where the superscript V stands for the V-notch) is the most important notch parameter of sharp V-notches in the LENFM. It is a grouped

parameter analogous to the stress intensity factor (SIF) used for cracked bodies under SSY conditions. It depends on geometry of a notched configuration (i.e., notch opening angle, notch length, and dimensions of the body) and boundary conditions. Contrary to the crack problems, the stress distribution around a sharp V- notch tip is generally more complicated. Williams [19] showed that stresses in a homogeneous notched body reaches infinite values asymptotically at the notch tip under any boundary conditions. Nevertheless, this stress singularity essentially depends on the notch angle [19].

The singular stress field at the tip of a sharp V-notch is in the form $\sigma_{ij} = K^V r^{\lambda-1} f_{ij}(\theta)$ where $f_{ij}(\theta)$ are angular functions, $\lambda - 1$ is the order of singularity, and K^V is NSIF [19]. In the LENFM, K^V completely characterizes the singular state of the stress field near the notch tip, akin to the case of crack problems. Many important brittle fracture characteristics of a sharp V-notch can be explained with the help of this parameter within the scope of LENFM.

Owing to the high stress gradients at the tip of a V-notch, crack initiation may occur at the notch tip. If the material is brittle or high-strength metals, then the crack propagates at high speed, and fracture would occur instantaneously. According to fracture mechanics, the mechanisms of crack initiation and propagation from a notch tip are fundamentally different for ductile and brittle materials. In brittle materials, the notch tip initiates cracks that consume a significant amount of the overall fracture energy, with crack propagation contributing minimally to this energy consumption. This is because the crack growth is such a rapid and unstable phenomenon that the final fracture occurs suddenly. Ductile materials, on the other hand, exhibit large plastic deformations around the notch tip; during ductile rupture, both crack initiation and propagation consume a considerable amount of energy.

To avoid crack initiation from the borders of notches or stress concentration regions in engineering components, recently, a notch fracture mechanics parameter known as the ***notch fracture toughness*** (NFT) or ***apparent toughness*** is found to be of great help [22]. NFT is found to be a material property like the fracture toughness (FT) in classical fracture mechanics and can be determined using experiments. Here NFT means the resistance of a notch against initiating crack(s) from its border, while the FT describes the propagation of a crack from an existing tip of a crack. A great deal of research shows that NSIFs, along with NFT, were found useful in solving the critical

loads at which cracks could originate from the notches. Excellent experimental verifications have been reported to treat the NFT as a material property.

Several failure criteria for brittle fracture in sharp V-notched components (i.e., a crack onset at a notch) have been proposed, mostly under the pure mode I loading conditions. Amongst them, theories based on the NSIF have become very popular. Some of these criteria are the mean stress criterion proposed by Seweryn [23], the critical notch stress intensity factor theory by Dunn et al. [14], the strain energy density approach by Lazzarin and Zambardi [24], the cohesive zone model by Gómez and Elices [25], J – integral based approach by Livieri [26], the strain energy release rate approach by Leguillon and Yosibash [27] and the point and mean stress theory by Ayatollahi and Torabi [28]. All these approaches present the failure criterion specifically for the mode I loading in the form $K_I^V = K_{IC}^V$, similar to that of the crack problems. Here K_I^V and K_{IC}^V are the mode I NSIF and critical value of K_I^V or the NFT, respectively. A major difference between FT and NFT is that, NFT defined as above, depends on the notch angle γ as NSIF also depends on the same. Different criteria are also available based on the NSIFs under mixed mode loading conditions [29].

All the above studies admit that the NSIF is the relevant and useful parameter to define a crack onset criterion at a notch tip and it could be employed for the determination of safe operating loads without cracks being initiated at the tip of a notch in notched components. Therefore, it is evident that the knowledge of accurate values of NSIFs of a notched configuration is one of the main requirements for the proper application of the above fracture criteria in practical applications. As a result, a large number of various methods for the accurate determination of NSIFs under general loading conditions have been developed in recent years. These works constitute an ongoing and active research field of the notch fracture mechanics.

1.5 NSIFs for different modes of loading

In line with the crack problems, NSIF, K^V is also usually designated based on the mode of loading. As shown in Fig.1.4, the three general cases of loading are

a) Opening mode or mode I

b) In-plane shear mode or sliding mode or mode II

c) Out-of-plane shear mode or tearing mode or mode III

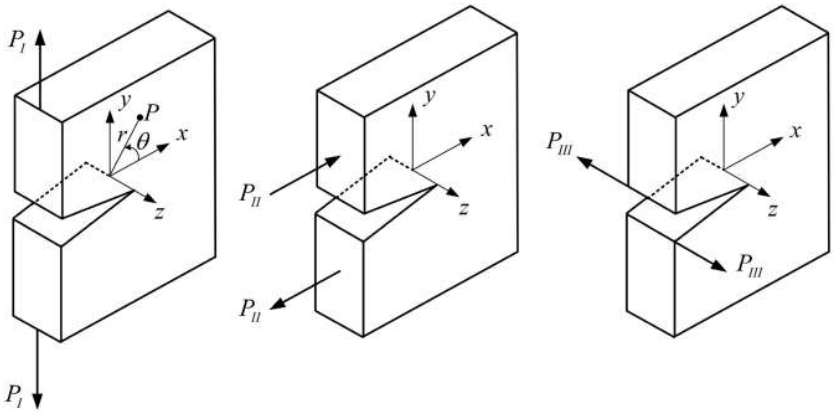

(a) (b) (c)

Figure 1.4 Three different modes of loading viz., (a) Mode I (Opening mode); (b) Mode II (In-plane shear mode); (c) Mode III (Out-of-plane shear mode).

In the mode I loading (Figure 1.4(a)), load is applied normally to the notch bisector plane which tends to open the notch. Mode II represents the loading in sliding mode and tends to slide one notch flank over the other. The displacement of the notch surface is perpendicular to the leading edge of the notch. Mode III represents the loading in tearing mode and the notch surfaces will have out of plane displacements. NSIFs corresponding to the mode I, mode II and mode III loading cases are designated as K_I^V, K_{II}^V and K_{III}^V, respectively.

A notched body can be loaded in any one of the aforesaid three modes or a combination of modes. Such loadings lead to mixed mode problems. Referring to the notch-tip local coordinate system in Fig.1.4, the stress field ahead of a notch tip for the case of linear elastic, isotropic materials under mode I, mode II and mode III loading conditions can be written as

$$\sigma_{ij}^{(I)} = \frac{K_I^V}{\sqrt{2\pi} r^{1-\lambda_1^I}} f_{ij}^{(I)}(\theta)$$
$$\sigma_{ij}^{(II)} = \frac{K_{II}^V}{\sqrt{2\pi} r^{1-\lambda_1^{II}}} f_{ij}^{(II)}(\theta) \qquad (1.1)$$
$$\sigma_{ij}^{(III)} = \frac{K_{III}^V}{\sqrt{2\pi} r^{1-\lambda_1^{III}}} f_{ij}^{(III)}(\theta)$$

where r and θ are the polar coordinates of a point P, as shown in Fig.1.4(a), and $f_{ij}(\theta)$ are angular functions that only depend on θ and loading mode. It can be noticed from Eq. (1.1) that $1/r^{1-\lambda_1}$ singularity prevails in stress components. Since strain components are functions of the stress components, therefore all strain components also tend to infinity in a similar fashion while approaching a sharp V-notch tip. Experience shows that the majorities of cracks are loaded in the opening mode compared to the other two modes (II and III) for isotropic materials. In the case of mixed mode problems (i.e., involving more than one loading mode), the individual contributions of the stress components are additive, i.e.,

$$\sigma_{ij}^{(Total)} = \sigma_{ij}^{(I)} + \sigma_{ij}^{(II)} + \sigma_{ij}^{(III)} \tag{1.2}$$

Clearly, this single parameter (i.e., NSIF) based description of notch tip conditions became one of the most important concepts in notch fracture mechanics. If K^V is accurately known, it is possible to determine all components of the stress, strain, and displacements ahead of a notch tip as a function of r and θ. The generalised expression of the NSIF is given by [30]

$$K^V = \sigma_\infty \sqrt{\pi} a^{1-\lambda_1} \cdot F\left(a/w\right) \tag{1.3}$$

where $F(a/w)$ is a non-dimensional parameter (also called as form factor or normalized NSIF) that depends on the overall geometry of the specimen and σ_∞ is the remotely applied load. Finally, a crack will nucleate from the tip of a sharp V-notch only if [23]

$$K^V > K_C^V \tag{1.4}$$

where K_C^V is the critical value of K^V.

1.6 Determination of NSIFs

From the previous discussion it clear that NSIFs play a pivotal role in the application of the principles of LENFM to practical problems for reliable design of the notched configurations. Therefore, accurate estimation of the NSIF is crucial for the successful application of the above principles to real-life components. Various analytical, numerical, and experimental methods have been developed over the years to determine NSIF.

1.6.1 Analytical methods

Very limited number of analytical methods are available in the literature for the sharp V-notches. Researchers attempted to derive NSIFs of notch problems from the existing solutions of SIFs of cracked bodies or stress concentration factors of the notched bodies. These are mostly limited to idealized geometries, loading and boundary conditions. However, analytical methods provide accurate solutions for relatively simple geometries and certain idealized material behaviour and could be used as benchmark problems for the validation of numerical methods and experimental methods.

1.6.2 Numerical methods

Numerical methods are extremely useful for the accurate determination of NSIFs of complex geometries with complex boundary conditions. Finite element method (FEM) and boundary element methods (BEM) are widely used for the numerical estimation of NSIFs of various notched configurations under mixed mode loading conditions. The use of numerical methods, particularly FEM, has vastly broadened the range of problems that can be solved by computational approaches. There has been a growing interest to develop new post-processing techniques for the accurate computation of NSIFs using numerical techniques. They can be estimated using either displacement-based, stress-based or energy-based methods, etc.

1.6.3 Experimental methods

In determining NSIFs, experimental methods provide new alternatives and opportunities. Due to many reasons, they become indispensable in notch fracture mechanics. Experimental works are very useful (a) under complex loading conditions, (b) for verifying the correctness of the numerical and analytical solutions and (c) for ascertaining the importance of assumptions made in various analyses. Several experimental techniques such as caustics, photoelasticity, digital image correlation, strain gage technique etc., have been developed over the years to determine mode I and mixed mode NSIFs of various notched configurations.

1.6.3.1 The method of caustics

The caustics or shadow spot method relies on the deflection of light rays caused by a gradient in the stress field. Caustics are three-dimensional surfaces in space enclosing a dark region and along which a high intensity of light occurs [31, 32]. A uniform light beam, incident on a reflective surface containing geometric nonlinearities, reflects and changes its intensity spatially, forming the caustic. Under load, light reflects from the area around the tip of a notch in a polished specimen. We can observe the caustic by placing a screen in the path of the reflected light. A thin ring of high intensity lights the caustic, surrounding a dark spot will be observed. The size and shape of the ring, or caustic can be related to the magnitude of NSIFs. The diameter of the caustic, the thickness of the specimen, the distance between the reference plane and the specimen, as well as the Young's modulus and Poisson's ratio of the specimen, all influence the NSIF.

The caustics method has the advantage of being applicable to both transparent and opaque materials. It can also be used with a variety of materials, such as isotropic, anisotropic, and composite materials, for the determination of NSIFs under static and dynamic loading conditions. This method is also widely employed for the determination of mixed-mode NSIFs.

1.6.3.2 Photoelasticity

The method of photoelasticity is one of the most popular experimental techniques for studying cracked and notched bodies. It is an optical method of experimental stress analysis that results in a whole-field representation of the principal stress difference [31]. The difference in the principal stresses is associated with the fringe order, material fringe constant, and the length of the light path. This method determines the NSIF by measuring the fringe order and position parameters on a fringe loop. Researchers have also applied this method to determine mixed-mode NSIFs [33, 34]. Although the idea of using the photoelasticity technique for the notch problems seems to be fascinating, many difficulties may encounter during measurements due to the high concentration of the isochromatic fringes near the notch tip.

1.6.3.3 Digital image correlation

The digital image correlation (DIC) method is an optical technique that compares two images before and after a component is subjected to a load or displacement [35]. Both opaque and transparent materials can utilize this method. The initial step in the DIC study involves properly preparing the surface, typically by spraying black speckles onto the white-painted specimen surface, which enables an appropriate visual contrast for processing. After the surface preparation, two images should be captured from the specimen before and after exerting load or displacement on the component. After taking the two images, the post-processing stage begins. To achieve a correlation between the undeformed and deformed images in the post-processing stage, initially, a few parameters associated with the digital image correlation (DIC) method should be defined in the DIC software or code being used. The fundamental parameters include the area of interest (AOI), the subset size, the step size, and the correlation criterion.

Although the DIC technique is promising to be a powerful tool for the experimental determination of NSIFs, depending on the number of deformation images to be processed, computation time may be a huge factor when analysing 3D-DIC datasets.

1.6.3.4 Electrical resistance strain gage

Experimental methods based on electrical resistance strain gage is one of the widely used techniques for the determination of SIFs and NSIFs because these techniques are relatively simple, easy to use, and inexpensive [31]. These techniques are extensively employed in fracture behavior of cracks [36]. The change in resistance of a conductor with its change in length forms the basis for strain measurement using strain gages.

Strain gauges are thin foils that are pasted to the body's surface and become an integral part of it. When the body undergoes certain deformation, the gage also gets subjected to the same amount of deformation. Consequently, the resistance of the gage material changes due to changes in its length following the deformation. This change in the resistance due to the deformation is measured in terms of change in voltage using a Wheatstone bridge circuit. The output voltage of the Wheatstone bridge circuit can be calibrated to give the axial strain along the strain gage. The measured strain is then related to SIF or NSIF by employing appropriate analytical equations. Strain gage methods are as powerful as photoelastic methods and are also cost-effective. Several static as well as dynamic studies of the cracked have been reported by many investigators using strain gage techniques. These techniques are also used for the experimental determination of mixed-mode SIFs. On the other hand, only a few studies are available on use of the strain gage techniques for notch problems. Due to inexpensive setup, these techniques are mostly employed in the development of standard methods of measuring the dynamic initiation, propagation and arrest toughness of cracked bodies.

1.7 Principle of operation of electrical resistance strain gage

The electrical resistance strain gage is the most versatile sensors to measure the surface strains of machine components and structural members. In 1856, Lord Kelvin reported that certain metal wires exhibited a change of electrical resistance with the change in strain. The resistance R of a uniform conductor with a length L, cross-sectional area A and specific resistance ρ is given by

$$R = \rho \frac{L}{A} \tag{1.5}$$

Therefore, when a conductor is pulled in the axial direction, a change in electrical resistance occurs due to the change in length of the conductor. This is the fundamental principle behind the operation of electrical resistance strain gauges. Usually, the change in resistance is a tiny quantity. The variation in resistance with the conductor's length is referred to as the strain sensitivity of the conductor. Because the resistance changes so little with a change in the conductor's length, special bridge circuits like the Wheatstone bridge or potentiometer bridge circuits are widely used in practice. The output voltage of the bridge circuit is proportional to the change in resistance of strain gages and hence proportional to the axial strain. Foil gages are the most widely used strain gages.

1.8 Bonded metallic foil strain gages

Current strain gages are typically provided in the form of bonded metal foil strain gages, even though it is theoretically possible to measure strain reliably and correctly utilizing just one length of wire as the strain gage's sensing element. A metallic foil strain gage is made of incredibly thin foil that has been rolled and placed in a grid pattern. The grid pattern maximizes the amount of metallic wire subject to strain in the parallel direction. Figure 1.5 shows a typical foil strain gage.

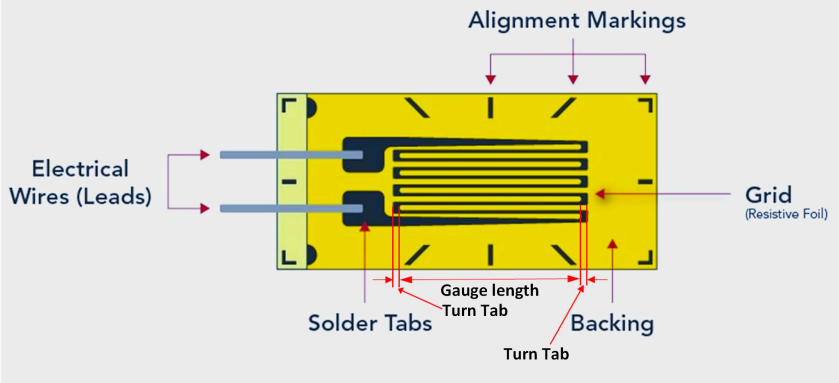

Figure 1.5 Typical foil strain gage.
(https://www.bing.com/images/blob?bcid=qGjRaZ.L9GAHbw)

The gage length, which is the basic measuring length of a strain gauge, is the dimension measured between the ends of the grid. From now on, the bonded metallic foil gages shall be referred to as strain gages. Most general-purpose strain gages produced today are fabricated from the copper-nickel alloy known as Advance or Constantan. The cross-sectional area of the grid is minimized to reduce the effect of shear strain and Poisson's effect. The grid is bonded to a thin backing, called the carrier, which is attached directly to the test specimen. As a result, the strains that the test specimen experiences are immediately communicated to the strain gage, which responds with a linear change in electrical resistance.

A variety of strain gages such as single element gage, two and three element rosettes, shear gage, strip gage and stress gage, etc., are commercially available for use in various situations. As discussed earlier, the change in resistance is so small that a highly sensitive circuit such as the Wheatstone bridge circuit is widely employed along with the metallic foil gages to measure the strains. The output voltage of the bridge can be directly related to the surface strains. The overall output of the strain sensor depends on gage resistance, lead wire resistance, type of lead wire connection, transverse sensitivity, thermal sensitivity, gage length, gage factor, type of strain gage and excitation voltage of the bridge circuit.

Optimizing the above parameters can reduce errors in strain measurement and ensure accurate surface strain measurement. In addition, it is essential to employ the proper adhesive and bonding procedures to achieve precise strain measurements. The most widely available strain gages are 120 Ω, 350 Ω and 1000 Ω. Commercially available dedicated strain gage data acquisition systems can further improve and simplify the accuracy of strain measurement. Some of the basic requirements of a strain gage are

- Linear strain sensitivity in the elastic range – for accuracy and repeatability.
- High resistivity – for the smallest size.
- Low hysteresis – for repeatability and accuracy.
- High strain sensitivity –for maximum electrical output for a given strain.
- Low and controllable temperature coefficient of resistance – for good temperature compensation.
- Wide operating temperature range – for the widest range of applications.
- Good fatigue life – for dynamic measurements.

1.9 Motivation

The phenomenon of brittle fracture of engineering components attributed to cracks and notches is considered to be a subject of significant importance in the design of engineering components. The geometrical discontinuities due to various notches give rise to localized stress concentration, leading to crack initiation and subsequent catastrophic failure of the component. Many times, engineers deliberately introduce these notches [35] to meet specific functions. The literature on notch fracture mechanics reveals extensive ongoing research on a variety of criteria for crack initiation at V-notches, and U-notches etc. Of these various notch types considered, modeling of certain geometric discontinuities as a sharp V-notch is found to provide practically useful and conservative solutions. Current research admitted that NSIF and its limiting value NFT have been found useful in crack initiation criteria under LENFM conditions for the sharp V-notch problems and thus NSIFs extensively employed for the critical load computations. It has been found that NSIF, K^V helps to provide a complete description of stress distribution in the singularity-dominated zone (SDZ) around a notch tip. For successful application of the above criteria, an accurate determination of NSIFs, therefore, is critical.

Experimental determination of NSIFs of sharp V-notches plays an indispensable role in the area of notch fracture mechanics. Among the various techniques available, the strain gage-based techniques are cost-effective, accurate, and easy to use. They can be used on components made of both metallic and non-metallic materials. Despite the many advantages and popularity of strain gage techniques in the experimental fracture mechanics domain, very limited techniques are currently available for determining NSIFs of the sharp V-notched configurations. The existing techniques are complex and require a large number of strain gages for even mode I NSIF determination. It is well-known that three-dimensional (3D) state of stress and transition zones from 3D to plane stress state prevails near the tip of a crack or a sharp V-notch. Further due to the plastic zone formation at the tip of a crack or V-notch, the measurements are affected by plasticity. It is also well-known that steep strain gradients in the vicinity of a crack or V-notch tips, strain measurements could be erroneous due

to the finite size of the strain gages. Clearly the radial location of strain gage for determination of NSIFs strongly influenced by the above effects. However, the existing techniques, apart from their inherent limitations, do not suggest or attempt to recommend appropriate gage locations for accurate determination of NSIFs. Clearly, such a provision (based on strong theoretical foundations) avoids plasticity effects, three-dimensional (3D) effects, and strain gradient effects that are known to appear near the tip of a crack or sharp V-notch [36]. Due to the lack of valid gage locations, researchers are compelled to guess the radial locations of gages which can lead to erroneous NSIFs.

Some of the factors influencing the simplicity of a strain gage technique and the accurate determination of NSIFs are (a) the strain series employed, (b) the number of gages required to determine NSIFs, (c) the orientation of the gages with respect to the notch axis, and (d) appropriate radial location (r) from a notch tip to the centre of a gage. Many of these requirements can be simplified by proper formulation of the strain gage technique using an appropriate strain expression(s) and manipulations, however, the most difficult and challenging problem is in deciding the appropriate radial distance (r) for each of the selected number of strain gages.

If the gages are pasted in the vicinity of a notch tip, 3D effects, strain gradient effects and plasticity effects will induce erroneous strain measurements and hence, errors in NSIF values. Alternatively, if the strain gages are pasted far from the notch tip, then the measured strains could not be represented by the selected strain expressions. Further the stress singularity may not prevail at those distant locations. It is clear that quantitative recommendation of the valid radial locations (r) for the strain gages is extremely important for the accurate determination of NSIFs using a strain gage technique.

From the above discussion, it is evident that a simple, practically efficient, and rugged strain gage technique with recommendations on valid strain gage radial locations for accurate determination of mode I NSIFs of sharp V-notched configurations is desirable. This requirement forms the motivation of the present work, and the next chapter outlines the objectives of the present investigation accordingly.

1.10 Organization of the thesis

The present thesis has been organized as follows:

Chapter 1 introduces the importance of notch fracture mechanics and its importance in the design of structures. A brief introduction of the strain gage technique for the determination of stress intensity factors is also presented.

Chapter 2 presents a thorough literature review on the use of strain gage techniques for accurate NSIF determination of the sharp V-notched configurations.

Chapter 3 provides a brief presentation of the theoretical background necessary to comprehend current contributions.

In **Chapter 4**, the formulations of the proposed single strain gage technique and valid gage locations for accurate determination of the mode I NSIFs of sharp V-notched configurations are presented with examples.

Chapter 5 describes the development of a finite element-based methodology for obtaining the maximum permissible gage locations, along with benchmark examples. This chapter also demonstrates the variation of these permissible locations with the change in geometric parameters of the V-notched configurations.

Chapter 6 presents the relevant experimental procedures along with a detailed description of the present experimental setup.

Chapter 7 provides a detailed study of the extent of various stress-strain zones around a notch tip and also experimentally substantiates the minimum permissible radial distance of strain gages r_{min} for accurate measurement of mode I notch stress intensity factors.

Chapter 8 of the thesis demonstrates the experimental determination of mode I NSIFs using valid gage locations (obtained using r_{max} and r_{min}) for several sharp V-notched configurations. The importance of valid gage locations is also discussed here with the help of the experimental results.

Chapter 9 concludes the thesis by outlining the important conclusions drawn from the present work and it also discusses the scope for future work.

Chapter 2

Literature Review

This chapter presents a detailed review of the literature on the application of NSIFs in studies of sharp V-notched bodies, as well as the determination of these factors using experimental methods. Due to the success of estimating the notch fracture toughness in terms of NSIFs and its widespread use in brittle fracture studies, there has been significant effort towards developing various numerical and experimental methods for the accurate NSIF estimation. Indeed, it is one of the current research directions in the notch fracture mechanics.

2.1 Brittle fracture criteria using NSIF

Certain stress raisers, such as flaws, the root of a gear, welds, and threads, are usually modelled as a sharp V-notch to arrive at a conservative solution. Theories of the sharp V-notch have also found applications in other engineering disciplines [13, 37, 38]. Investigating stress, strain, and displacement fields in the vicinity of a sharp notch tip plays an important role as they greatly affect the load-bearing capacity of the structures. In linear elastic theories of sharp V-notches, the main attention is typically on the first term of the Williams' series expansion [19], which is a singular term and directly proportional to the notch stress intensity factor (NSIF).

Williams [19] determined the form of plane stress distribution near the vertex of a wedge in terms of eigenfunction expansion for various conditions at the edge of the wedge. He was the first to investigate the analytical form of singularities resulting at a notch tip under general in-plane loading. He investigated three different boundary conditions, viz., (a) free-free, (b) clamped-clamped, and (c) clamped-free. He showed that the stresses in a homogeneous notched body become infinite at the notch tip under any boundary conditions.

Due to the presence of sharp V-notches, the static and fatigue load-carrying capacities of engineering components decrease, and sudden fracture is also a major failure mode in components made of brittle and quasi-brittle materials. This is mainly

due to the crack initiation at the worst notches, such as a sharp V-notch. Several studies have been reported attempting to propose a brittle fracture criterion at the sharp V-notches [23, 39-48]. All these criteria address the required conditions for the onset of crack initiation at the notch tip.

Carpinteri [39] was the first to experimentally estimate the critical loads of the sharp V-notches for various notch angles under mode I loading conditions using PMMA specimens. He also computed the critical values of NSIFs for a broad range of notch opening angles using averaged critical failure loads derived from experiments. Later, Seweryn [23] developed a brittle fracture criterion based on the critical values of NSIFs. This criterion states that when NSIFs approaches a certain value, a crack will start to spread from the notch tip. He then presented a general brittle fracture criterion for the sharp V-notched bodies as in Eq. (1.4).

Dunn et al. [40] provided evidence in favor of the theory that the critical NSIFs can correlate brittle fracture initiation at the sharp V-notches, by determining the critical NSIF under mode I loading from the critical loads observed in the tests. Using finite element analyses, they came to the conclusion that LENFM conditions apply since the plastic zone size is lower than the singularity dominated zone. Dunn et al. [41] conducted additional experimental experiments to support the use of NSIF's critical value to correlate brittle failure. According to their findings, applying the critical stress intensity yields excellent failure correlation in mode I, mode II, and mixed mode (I/II) loading.

Ayatollahi and Torabi [28], as well as Ayatollahi et al. [29], developed a crack initiation criterion in rounded and sharp V-notched bodies based on the well-known maximum tangential stress (MTS) in terms of NSIFs for mixed mode (I/II) loading conditions. Such mixed-mode criteria predict both the critical load and crack deflection angle. Yosibash et al. [42, 43] re-examined the validity of a number of established brittle crack initiation criteria that depend on NSIF. Comparison studies were carried out for mode I [42] and mixed mode (I/II) [43] loading conditions. Their predictions were compared to experimental observations made on V-notched specimens made of PMMA and alumina-7% zirconia (ceramic). The results of various experiments showed good agreement with the experimental results.

In addition, recent studies [47] established a relationship between the NSIF and energy release rate for sharp V-notches, further strengthening these criteria. As a result,

it is critical to obtain accurate NSIF values to deal with the crack initiation aspect at the tip of a sharp V-notch.

2.2 Determination of NSIFs

Due to the practical importance of NSIFs, significant research has been conducted over the past few years to accurately determine these factors in various notched configurations subjected to complex loading using various analytical [30, 49-53], numerical [54-70], and experimental methods [33, 34, 71-94]. These methods are briefly reviewed in the following subsections.

2.2.1 Analytical methods

Because of the complex nature of sharp V-notch problems, only a few analytical/semi-analytical methods are available for determining NSIFs. Only a few researchers [49-53] attempted to directly determine the NSIFs of V-notched configurations from existing solutions of other problems, such as the stress concentration factor of a sharp V-notch [49] and the SIF of crack problems [50-52]. Hasebe and Kutana [49] showed that the mode I NSIFs of the V-notches with a small tip radius could be determined from the corresponding SCF. These SCF expressions can be obtained either from the experiments or from the handbooks. Alternatively, other researchers [50–52] tried to provide a correlation between the values of NSIF of a V-notch and a linear crack for which the SIF solutions are readily available. Recently, Loua and Barltrop [53] proposed a simple methodology to determine the NSIFs of V-notched plates, both with and without cracks emanating from the notch, using the available formulas for finite width cracked plates. However, Loua and Barltrop's approach is only applicable to configurations with edges cracked or notched.

2.2.2 Numerical methods

For intricate notched geometries with complex loading and boundary conditions, numerical methods such as the boundary collocation method, body force method, finite

element (FE) method, boundary element method, etc., are frequently employed. It can be observed that, among all available numerical methods, the FE method has been extensively used in practice. A large number of post-processing methods, such as displacement-based, stress-based, and energy-based [54–70], have been developed, and it is an active area of research in the notch fracture mechanics. Some of these methods, which were developed in conjunction with the finite element method, are reviewed here.

Ju and Chung [69] developed a least-square method (LSM) for the evaluation of the NSIFs of the sharp V-notches by minimizing the errors in the stresses at the nodes around the notch tip. They have suggested that higher-order stress terms should be considered for the NSIFs to be more accurate. Another stress-based method, described by Liu et al. [67], uses a series of nodes spaced out along a radial line just outside the notch tip in a chosen direction to find the mixed mode (I/II) NSIFs. They evaluated the NSIFs by minimizing the errors in the analytical and FE stresses at the selected nodes along the radial line. Meneghetti and Lazzarin [58] extended the peak stress method to determine mode I NSIFs at the tip of sharp V-notches for a wide range of notch opening angles ranging from $0°$ to $135°$. The PSM is an FE stress-based method used to estimate NSIFs from the elastic peak stress. Later, this PSM was used to estimate the mode I, mode II, and mode III NSIFs of 2D and 3D configurations [68].

To the knowledge of the author, only a few displacement-based methods are available for the determination of NSIFs. Ayatollahi and Nejati [65] proposed an overdeterministic method with displacements as the sampling points along a circular arc. They proposed a method for computing the NSIFs and higher-order coefficients of the Williams [19] series expansion using FE displacements from the nodes around the notch tip. Recently, Hussain and Murthy [54, 55] proposed two new methods, namely the point substitution method and the notch-flank displacement collocation method. The point substitution method computes mode I and mixed mode NSIFs using a displacement component at an optimal point on sharp V-notch flanks. In another method [55], a collocation method was developed based on the notch opening and sliding displacements. After comparing existing methods [56], they concluded that displacement methods are easy to implement and provide highly accurate NSIFs in all complex loading conditions.

The strain energy density concept was utilized by many researchers to calculate NSIFs of a sharp V-notch [24, 70]. These works computed the NSIFs for sharp and rounded notches based on the averaged strain energy density over a control volume around the notch tip. Lazzarin and Zambardi [24] determined the NSIFs of isotropic homogeneous notches under the pure mode I loadings. This method was improved by Lazzarin et al. [70], who used it to find the mixed mode (I/II) NSIFs by taking samples of the field variable on two concentric volumes around the notch tip. Nevertheless, this method [70] cannot be used for the crack problems under mixed mode loading conditions. Moreover, researchers used the strain energy density to calculate NSIFs of notched plates of orthotropic materials [62].

2.2.3 Experimental methods

Experimental investigations are necessary for the substantiation and reliability of theoretical and numerical solutions and to recognise the limitations and assumptions made in various analyses. Over the years, researchers have developed several experimental techniques to determine NSIFs of notched bodies, including the strain gage technique [71-73], caustics [74-80], photoelasticity [33, 34, 81-83], digital image correlation (DIC) technique [35, 84-91], digital gradient sensing technique [92, 93], and coherent gradient sensing technique [94]. Within these techniques, strain gage techniques have several advantages due to their simplicity, accuracy, and ease of use in almost every environment [31, 95]. Furthermore, they are applicable to a wide range of experimental specimen materials, including both metals and non-metals. They also allow localized measurements within a steep strain gradient zone. The following sections provide reviews of some of these experimental techniques. A separate section has been devoted for review of the works using strain gage techniques.

2.2.3.1 Determination of NSIFs using caustics

The NSIFs of sharp V-notched symmetrically loaded plates were determined using the caustics method by Prassianakis and Theocaris [77]. They developed an experimental solution for determining NSIFs based on reflected caustics theory. Another study, Xu et al. [76], used an optical caustics method to determine the mode I NSIFs of the sharp

V-notches of specimens under three-point bending. Yazdanmehr and Soltani [78] developed another experimental caustic method to calculate the mixed mode (I/II) NSIFs for the rounded V and U-notches. All the above-mentioned researchers used specimens made of PMMA material in their experiments. Recently, Yang et al. [79] determined the mode II (pure shear) NSIF using the caustics method. They conducted experiments on specimens made of PMMA material. They also derived a formula for mode II NSIF and length of the caustic curve. The experimental results demonstrated good accuracy when compared to the available pure mode II NSIF results. In addition, Liu et al. [79] used the transmitted caustics method to determine mode I NSIFs of blunt V-notches in polymeric materials. They tested several three-point bend specimens with varying notch tip root radii. Their findings are in good agreement with the FE results.

2.2.3.2 Determination of NSIFs using photoelasticity

Mahinfalah and Zackery [33] employed the photoelastic and digital image analysis techniques to determine stress intensity factors for $90°$ reentrant corners. They obtained NSIFs by combining the overdeterministic least squares method with the Newton-Raphson method. Ayatollahi and Nejati [34] used higher order terms in photoelasticity to determine the NSIFs of V-notched specimens under pure mode I, pure mode II, and mixed mode (I/II) loading conditions. Further higher-order non-singular terms were also evaluated using their technique. Recently, Liu et al. [81] used photoelasticity to determine the NSIFs of blunt V-notches under mode I loading conditions. The experimental values demonstrated a strong agreement with the numerical estimations. Murthy and Rao [83] used photoelasticity to determine mode I NSIFs under bending and tensile loading conditions.

2.2.3.3 Determination of NSIFs using DIC technique

Over the last decade, there has been a growing interest in determining V-notches' NSIFs using the DIC technique. Torabi et al. [84, 85] used the DIC technique to determine mode I NSIFs of sharp V-notched [84] and blunt V-notched specimens [85]. Both studies utilized an overdeterministic method to determine the NSIFs. Bahrami et al. [86], on the other hand, used the DIC technique to determine mixed mode (I/II) NSIFs

of sharp V-notched configurations. Recently, Shi and Oyadiji [35] used a three-dimensional digital image correlation experimental method and a finite element overdeterministic method to measure mode I NSIFs with sharp V-notched configurations. In a subsequent study, Shi and Oyadiji [87] utilized the 3D DIC technique to assess its feasibility in terms of the accuracy of the measured mode I NSIFs of sharp V-notched configurations. Ju et al. [90] used a least squares technique along with the 2D DIC technique to determine mode I NSIFs of sharp V-notched specimens, and they compared the experimental results with finite element estimations. Dehnavi et al. [91] employed digital image correlation to analyze the displacement field around the edge of sharp V-notches in PMMA samples with and without tip cracks. They also determined mode I NSIFs for different notch opening angles and notch length.

2.3 Strain gage techniques for the determination of NSIFs

Dally and Sanford [36] first developed a practically feasible, simple, and robust strain gage technique for the determination of mode I SIF near a crack tip, several decades after Irwin's [6] recommendation. They used a truncated strain series comprising three unknown coefficients (multi-parameter strain series) to represent the strains in the experimental specimens. The multi-parameter representation of the strain field allowed for the placement of the strain gauges at greater radial distances from the crack tip, rather than in the crack tip's vicinity. In addition, with clever manipulation of the selected multi-parameter strain expressions, they developed a robust technique for experimental determination of the mode I SIF using only one strain gage. The main benefit of their technique [36] is that only one strain gage is enough to accurately determine mode I SIF. Many researchers [96–102] preferred this technique for measuring mode I SIF in different contexts due to various advantages. This technique has become the most popular strain gage for crack problems in both static and dynamic loading conditions.

While strain gage techniques became popular for crack problems [96-108], only a limited number of techniques are available for sharp V-notched bodies [71-73]. Kondo et al. [71] were the first to propose a strain gage technique for determination of NSIFs under mixed mode loading conditions. They considered a singular term and a

non-singular term for representation of the strain field. Their method necessitates placing a large number of strain gages in more than two directions. They invoked a least squares approach to determine the mixed mode NSIFs using the measured strains at different locations. They did not provide any guidelines or methodology regarding the placement of strain gauges in their approach. The location of strain gages in their experiments was based on the locations used by Dally and Sanford [36] for crack problems, which ranged from approximately 1.5 mm to 10.5 mm from the notch tip. Their findings show measured NSIFs with a 10% error.

In another work, Kondo et al. [72] extended their strain gage technique to the problems of plate bending for the determination of mixed mode generalized NSIFs. Plates with sharp V-notches under transverse loading were considered. Here also, no recommendations were provided on the possible locations of the strain gages. Again, their method necessitates the use of a large number of gages for determining even mode I NSIFs. Their experimental results agreed with the theoretical results in this study, with an error of nearly 20%.

Peng et al. [73] used strain gauges and dynamic caustics on sharp V-notched three-point bend specimens to test the crack initiation toughness and crack propagation toughness of PMMA material. Only singular strain terms defined by NSIF were considered for the determination of NSIFs. However, an empirical formula suggested positioning the strain gages between 0.25 mm and 2.3 mm from the notch tip. Peng et al. [73] stated that these locations keep a strain gage beyond the singularity-dominated zone. The strain gage measurements produced NSIF results that were consistent with those calculated using the dynamic caustics method. Peng et al. [73] did not suggest any procedure or methodology for the appropriate location of strain gages.

2.4 Review on strain gage locations

The above existing strain gage techniques (Section 2.3) have various drawbacks, such as the use of a large number of strain gages even for determination of one NSIF and the lack of any methodology supported by the theory for appropriate placement of selected numbers of strain gages. As a result, the placement of the gages depends on past experience, guesswork, or empirical expressions. Clearly, such approaches lead to large

errors in the measured NSIFs. On the other hand, Dally and Sanford [36] have proposed a simple, rugged, and efficient single strain gage technique for the cracked geometries, which allows for the accurate determination of mode I SIFs. This method enables the placement of a single gage at greater distances from the crack tip, thereby neatly avoiding crack tip complications.

Sarangi et al. [100-102] significantly enhanced the Dally and Sanford [36] technique by proposing reliable strain gage locations backed by sound theory. These works have garnered significant attention because they enable the use of gages without relying on guesswork or speculation, leading to extremely accurate SIFs using the well-known Dally and Sanford [36] technique. Their approach to the estimation of valid gage locations essentially depends on two parameters viz., the minimum radial distance and the maximum allowable radial strain gage location, which are backed by strong theoretical foundations. The later depends strongly on the geometry of the cracked configuration.

Similar to cracks, the vicinity of the tip of a sharp V-notch is subject to various effects, including (a) three-dimensional effects [109, 110], (b) strain gradient errors due to steep variation of strains, and (c) plasticity effects [36]. Research on cracked bodies reveals that employing small strain gauges [36, 111–113] and positioning them at a suitable distance from the singularity can significantly reduce these effects. However, gages placed at a large distance from the notch tip will not be able to capture the singular solution, which does not prevail at such distances. Moreover, the selected strain expressions may not be valid at those distant locations. Therefore, the gage's radial location should be neither too close nor too far from the notch tip, and it should be positioned such that the measured strains fall within the validity of the selected strain equation used to represent the strain field near the notch tip.

Previous research [114–119] using extensive numerical and experimental studies conclude that there is a 3D state of stress with a transition zone from 3D to 2D state of stress near a crack or a sharp V-notch tip. These studies also show that the 3D state of stress and transition zones terminate at a radial distance of 1.5 times the thickness of the plate for the cracked panels [114, 115] and 1.25 times the thickness of the plate for the sharp V-notched panels [116, 119]. It is evident that strain gauges should not be placed below these limits, as they set a minimum radial distance for their location. This is because experiments typically test specimens under plane stress

conditions, requiring 2D asymptotic solutions to determine NSIFs. If a strain gage is located either in a 3D or transition zone, the resulting NSIFs contain a large error due to the substitution of the measured strain (which is not a 2D strain) in 2D solutions. The former limit was substantiated by the experimental studies [113], and the recommended value has been used in experiments with cracked bodies. However, no experimental substantiation is available till date for sharp V-notches on the value recommended by Li et al. [116] i.e., 1.25 times thickness of the plate. Indeed, Li et al. [116] used finite element analyses to study the extents of 3D, 3D-2D, and 2D zones in various notched configurations, including the sharp V-notch. Similarly, Li and Guo [119] presented the detailed nature of the elastic field in front of U and V-notched panels subjected to far-field tensile stresses based on the 3D finite element analyses. Further, Góes et al. [117] verified numerically the results given by Li and co-workers [116, 119]. None of these works reported experimental substantiation of the extent of 3D and transition zones suggested.

2.5 Summary of the literature review and objectives

2.5.1 Summary of the literature review

The present literature review could be summarised as follows.

- For several years, great effort has been devoted to understand the behavior of different types of notches under different loading conditions in the notch fracture mechanics.
- Sharp V-notch is found more useful in modelling varieties of notches and defects than a crack as it provides conservative solutions instead of providing excessively conservative solutions.
- One of the main thrusts of the notch fracture mechanics is to find appropriate crack initiation criteria under complex loading conditions for sharp V-notches.
- Several classical works substantiated that notch stress intensity factor (NSIF) based failure criteria are very useful. The critical value of the notch stress intensity factor, which manifests as the fracture toughness for crack onset from the V-notch, is a property of the material.

- For several years a great deal of effort has been devoted in devising the methods for the accurate determination of the NSIFs of sharp V-notched configurations.
- Strain gage techniques are found extremely useful in experimental determination of the NSIFs under complex loading conditions.
- Several publications have been reported on the notch tip complications that pose challenges for the measurement of surface strains using strain gages. These complications or effects influences the location of placement of a strain gage for the accurate determination of the NSIFs.
- Simple and efficient strain gage techniques are scarcely available till date for the accurate determination of the NSIFs of the sharp V-notched configurations. No recommendations or suggestions on the valid radial locations of the strain gages have been made by the existing techniques.
- Li and Guo [119] determined the extent of 3D, and 3D to 2D transition zones for a sharp V-notched configurations using finite element analyses. However, till date no experimental verification of these extents have been made. The extent of these zones is one of the factors for selection of the valid gage locations in strain gage techniques.

2.5.2 Objectives of the present investigation

Considering the motivation behind the present investigation, summary and gaps in the literature review on the current knowledge of the strain gage techniques for the sharp V-notches, the following objectives have been laid down for the present work.

1. To develop a simple and efficient new strain gage technique that allows pasting of a strain gage at distant locations from the notch tip for the accurate determination of mode I NSIF (K_I^V) of 2D sharp V-notched bodies made of isotropic materials.
2. To develop a procedure based on strong theoretical foundations for *a priori* assessment of the valid or appropriate strain gage locations for the accurate measurement of the mode I NSIFs of the sharp V-notched configurations. This objective includes development of methodologies for assessment of the minimum and maximum allowable radial locations of the strain gages and to

understand behaviour of these limits on the geometry of the notched configuration.

3. To substantiate numerically and experimentally the extent of 3D stress-strain states and 3D to 2D transition zones ahead of a sharp V-notch proposed by Li and Guo [119] in order to quantify the minimum allowable radial location of a strain gage.
4. To conduct numerous experiments on different sharp V-notched configurations for the substantiation of efficacy of the proposed strain gage technique and to demonstrate the existence and usefulness of the proposed valid strain gage locations.

Chapter 3

Theoretical background and formulations

This chapter describes field equations around the tip of a sharp V-notch and other important mathematical background required for understanding the contributions of the present work presented in the subsequent chapters. The present investigation employs 2D and 3D finite element analyses of notched configurations using commercial software ANSYS®, and therefore a brief description of elements used in the current investigation is also presented in this chapter.

3.1 Williams' eigenfunction expansion method

Let us consider an arbitrary 2D body containing a sharp V-notch with apex angle or notch angle γ (having stress free notch surfaces) and subjected to pure mode I loading as shown in Fig.3.1.

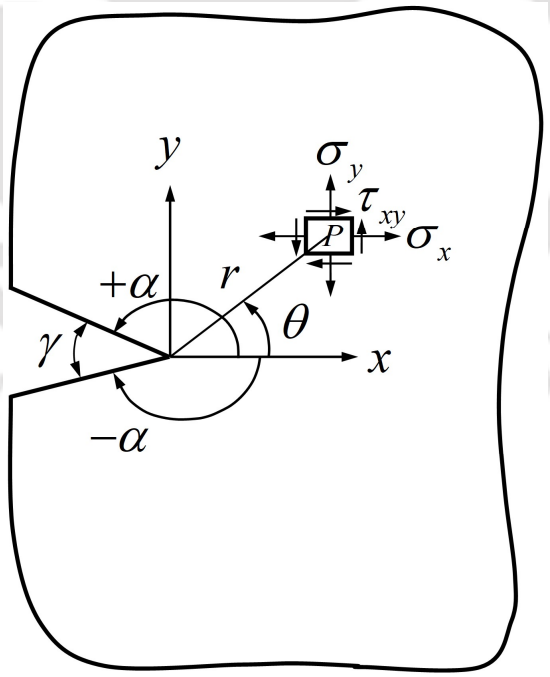

Figure 3.1 An arbitrary 2D body with a sharp V-notch subjected to pure mode I loading.

P is a point at a distance r from the notch tip subtending an angle θ with the positive x-axis. The stress function must satisfy the bi-harmonic equation in polar coordinates as shown below

$$\nabla^4\phi = \left(\frac{\partial^2}{\partial r^2}+\frac{1}{r}\frac{\partial}{\partial r}+\frac{1}{r^2}\frac{\partial^2}{\partial\theta^2}\right)\left(\frac{\partial^2}{\partial r^2}+\frac{1}{r}\frac{\partial}{\partial r}+\frac{1}{r^2}\frac{\partial^2}{\partial\theta^2}\right)\phi = 0 \tag{3.1}$$

where r and θ are as shown in Fig.3.1. According to Williams [19], the Airy stress function ϕ with λ' as the order of the singularity is

$$\phi = r^{\lambda'+1} f(\theta) \tag{3.2}$$

Eq. (3.1) can be rewritten as

$$\nabla^2\left(\frac{\partial^2}{\partial r^2}+\frac{1}{r}\frac{\partial}{\partial r}+\frac{1}{r^2}\frac{\partial^2}{\partial\theta^2}\right)\phi = 0 \tag{3.3}$$

Substituting Eq. (3.2) in Eq. (3.3),

$$\left\{(\lambda'+1)^2+\frac{\partial^2}{\partial\theta^2}\right\}\left\{(\lambda'-1)^2+\frac{\partial^2}{\partial\theta^2}\right\} r^{\lambda'-3} f(\theta) = 0 \tag{3.4}$$

Since $r^{\lambda'-3} \neq 0$, therefore

$$\left\{(\lambda'+1)^2+\frac{\partial^2}{\partial\theta^2}\right\}\left\{(\lambda'-1)^2+\frac{\partial^2}{\partial\theta^2}\right\} f(\theta) = 0 \tag{3.5}$$

Eq. (3.5) will be satisfied when either

$$\left\{(\lambda'+1)^2+\frac{\partial^2}{\partial\theta^2}\right\} f(\theta) = 0 \tag{3.6}$$

$$\text{or } \left\{(\lambda'-1)^2+\frac{\partial^2}{\partial\theta^2}\right\} f(\theta) = 0 \tag{3.7}$$

Solving Eq. (3.6) yields

$$f(\theta) = A_1 \cos(\lambda' + 1)\theta + A_3 \sin(\lambda' + 1)\theta \tag{3.8}$$

and solving Eq. (3.7) yields

$$f(\theta) = A_2 \cos(\lambda' - 1)\theta + A_4 \sin(\lambda' - 1)\theta \tag{3.9}$$

Combining Eq. (3.8) and Eq. (3.9), the generalized solution can be derived as

$$f(\theta) = A_1 \cos(\lambda' + 1)\theta + A_3 \sin(\lambda' + 1)\theta + A_2 \cos(\lambda' - 1)\theta + A_4 \sin(\lambda' - 1)\theta \tag{3.10}$$

where A_1, A_2, A_3 and A_4 are constants. Substituting Eq. (3.10) into Eq. (3.2), the Airy stress function ϕ can be rewritten as

$$\phi = r^{\lambda'+1}\left\{A_1 \cos(\lambda' + 1)\theta + A_2 \cos(\lambda' - 1)\theta + A_3 \sin(\lambda' + 1)\theta + A_4 \sin(\lambda' - 1)\theta\right\} \tag{3.11}$$

The stress components in polar coordinates (neglecting the body forces) at any point $P(r,\theta)$ in terms of ϕ can be written as

$$\sigma_r = \frac{1}{r^2}\frac{\partial^2 \phi}{\partial \theta^2} + \frac{1}{r}\frac{\partial \phi}{\partial r} \tag{3.12}$$

$$\tau_{r\theta} = \frac{1}{r^2}\frac{\partial \phi}{\partial \theta} - \frac{1}{r}\frac{\partial^2 \phi}{\partial r \partial \theta} \tag{3.13}$$

$$\sigma_\theta = \frac{\partial^2 \phi}{\partial r^2} \tag{3.14}$$

Substituting Eq. (3.11) into Eqs. (3.12) - (3.14) yields

$$\sigma_r = r^{\lambda'-1}\begin{Bmatrix} -\lambda'(\lambda'+1)A_1\cos(\lambda'+1)\theta - \lambda'(\lambda'-3)A_2\cos(\lambda'-1)\theta - \\ \lambda'(\lambda'+1)A_3\sin(\lambda'+1)\theta - \lambda'(\lambda'-3)A_4\sin(\lambda'-1)\theta \end{Bmatrix} \quad (3.15)$$

$$\tau_{r\theta} = r^{\lambda'-1}\begin{Bmatrix} \lambda'(\lambda'+1)A_1\sin(\lambda'+1)\theta + \lambda'(\lambda'-1)A_2\sin(\lambda'-1)\theta - \\ \lambda'(\lambda'+1)A_3\cos(\lambda'+1)\theta - \lambda'(\lambda'-1)A_4\cos(\lambda'-1)\theta \end{Bmatrix} \quad (3.16)$$

$$\sigma_\theta = \lambda'(\lambda'+1)r^{\lambda'-1}\begin{Bmatrix} A_1\cos(\lambda'+1)\theta + A_2\cos(\lambda'-1)\theta + \\ A_3\sin(\lambda'+1)\theta + A_4\sin(\lambda'-1)\theta \end{Bmatrix} \quad (3.17)$$

As the notch edges are free surfaces (Fig.3.1), then the boundary conditions are

$$\sigma_\theta = \tau_{r\theta} = 0 \text{ at } \theta = \pm\alpha \quad (3.18)$$

Substituting Eq. (3.17) in Eq. (3.18) at $\theta = +\alpha$, (Fig.3.1) we get

$$A_1\cos(\lambda'+1)\alpha + A_2\cos(\lambda'-1)\alpha + A_3\sin(\lambda'+1)\alpha + A_4\sin(\lambda'-1)\alpha = 0 \quad (3.19)$$

Similarly, substituting Eq. (3.17) in Eq. (3.18) at $\theta = -\alpha$, we get

$$A_1\cos(\lambda'+1)\alpha + A_2\cos(\lambda'-1)\alpha - A_3\sin(\lambda'+1)\alpha - A_4\sin(\lambda'-1)\alpha = 0 \quad (3.20)$$

Adding Eq. (3.19) and Eq. (3.20) and simplifying, we get

$$A_1\cos(\lambda'+1)\alpha + A_2\cos(\lambda'-1)\alpha = 0 \quad (3.21)$$

Next, substituting Eq. (3.16) in Eq. (3.18) at $\theta = +\alpha$, we get

$$(\lambda'+1)A_1\sin(\lambda'+1)\alpha + (\lambda'-1)A_2\sin(\lambda'-1)\alpha - (\lambda'+1)A_3\cos(\lambda'+1)\alpha - (\lambda'-1)A_4\cos(\lambda'-1)\alpha = 0 \quad (3.22)$$

Similarly, substituting Eq. (3.16) in Eq. (3.18) at $\theta = -\alpha$, we get

$$\begin{aligned}&(\lambda'+1)A_1\sin(\lambda'+1)\alpha+(\lambda'-1)A_2\sin(\lambda'-1)\alpha+(\lambda'+1)A_3\cos(\lambda'+1)\alpha\\&+(\lambda'-1)A_4\cos(\lambda'-1)\alpha=0\end{aligned} \tag{3.23}$$

Adding Eq. (3.22) and Eq. (3.23) and simplifying, we get

$$(\lambda'+1)A_1\sin(\lambda'+1)\alpha+(\lambda'-1)A_2\sin(\lambda'-1)\alpha=0 \tag{3.24}$$

Subtracting Eq. (3.20) from Eq. (3.19) yields

$$A_3\sin(\lambda'+1)\alpha+A_4\sin(\lambda'-1)\alpha=0 \tag{3.25}$$

Subtracting Eq. (3.22) from Eq. (3.23), we get

$$(\lambda'+1)A_3\cos(\lambda'+1)\alpha+(\lambda'-1)A_4\cos(\lambda'-1)\alpha=0 \tag{3.26}$$

Eq. (3.21), Eq. (3.24), Eq. (3.25) and Eq. (3.26) can be written in a matrix form as

$$\begin{pmatrix}(\lambda'+1)\sin(\lambda'+1)\alpha & (\lambda'-1)\sin(\lambda'-1)\alpha\\ \cos(\lambda'+1)\alpha & \cos(\lambda'-1)\alpha\end{pmatrix}\begin{pmatrix}A_1\\A_2\end{pmatrix}=0 \tag{3.27}$$

and

$$\begin{pmatrix}(\lambda'+1)\cos(\lambda'+1)\alpha & (\lambda'-1)\cos(\lambda'-1)\alpha\\ \sin(\lambda'+1)\alpha & \sin(\lambda'-1)\alpha\end{pmatrix}\begin{pmatrix}A_3\\A_4\end{pmatrix}=0 \tag{3.28}$$

Solving Eq. (3.27) for the non-trivial solution results into

$$\lambda'\sin 2\alpha+\sin 2\lambda'\alpha=0 \tag{3.29}$$

Similarly, solving Eq. (3.28) for the non-trivial solution gives

$$\lambda' \sin 2\alpha - \sin 2\lambda'\alpha = 0 \tag{3.30}$$

Now generalising the characteristics equations Eq. (3.29) and Eq. (3.30), we get [65]

$$\begin{aligned} &\lambda_n' \sin 2\alpha + \sin 2\lambda_n'\alpha = 0 \quad \text{for mode I} \\ &\lambda_n' \sin 2\alpha - \sin 2\lambda_n'\alpha = 0 \quad \text{for mode II} \end{aligned} \tag{3.31}$$

where λ_n' is the n^{th} eigenvalue for mode I and mode II. Therefore, from Eq. (3.24)

$$A_{1,n} = \frac{-(\lambda_n' - 1)\sin(\lambda_n' - 1)\alpha}{(\lambda_n' + 1)\sin(\lambda_n' + 1)\alpha} A_{2,n} \qquad \text{(for mode I)} \tag{3.32}$$

and from Eq. (3.26)

$$A_{3,n} = \frac{-(\lambda_n' - 1)\cos(\lambda_n' - 1)\alpha}{(\lambda_n' + 1)\cos(\lambda_n' + 1)\alpha} A_{4,n} \qquad \text{(for mode II)} \tag{3.33}$$

3.1.1 Stress components in polar coordinate system for mode I

Now, Airy's stress function ϕ can be separated as a sum of even and odd functions as, $\phi = \phi_{\text{even}} + \phi_{\text{odd}}$. Here, ϕ_{even} represents mode I (symmetric loading condition) and ϕ_{odd} represents mode II (anti-symmetric loading condition) [66]. For symmetric loading condition (mode I), we have

$$\phi_{\text{even}} = \sum_{n=1}^{\infty} r^{\lambda_n'+1}[A_{1,n}\cos(\lambda_n' + 1)\theta + A_{2,n}\cos(\lambda_n' - 1)\theta] \tag{3.34}$$

where n is the order of the term in the infinite series, λ_n' is the n^{th} eigenvalue of the mode I and the terms $A_n' = A_{1,n}', A_{2,n}' \ldots$ etc., are the Williams' coefficients. From Eq. (3.32),

$$\frac{A_{1,n}}{A_{2,n}} = \frac{-1}{(\lambda_n' + 1)}(\lambda_n' \cos 2\alpha + \cos 2\lambda_n'\alpha) \tag{3.35}$$

Substituting Eq. (3.35) in Eq. (3.34), we get (for only real parts)

$$\phi_{\text{even}} = \sum_{n=1}^{\infty} \text{Re}\left[r^{\lambda_n'+1} A_{2,n} \left\{ \cos(\lambda_n' - 1)\theta - \frac{(\lambda_n' \cos 2\alpha + \cos 2\lambda_n'\alpha)}{(\lambda_n' + 1)} \cdot \cos(\lambda_n' + 1)\theta \right\} \right] \tag{3.36}$$

Using Eq. (3.36) in Eq. (3.12), Eq. (3.13) and Eq. (3.14), we get the following expressions of stress components σ_r, σ_θ and $\tau_{r\theta}$

$$\sigma_r = \sum_{n=1}^{\infty} \text{Re}\left[\frac{\lambda_n' A_{2,n}}{r^{1-\lambda_n'}} \left\{ \begin{matrix} (3 - \lambda_n') \cdot \cos(\lambda_n' - 1)\theta + (\lambda_n' \cos 2\alpha \\ + \cos 2\lambda_n'\alpha) \cdot \cos(\lambda_n' + 1)\theta \end{matrix} \right\} \right] \tag{3.37}$$

$$\sigma_\theta = \sum_{n=1}^{\infty} \text{Re}\left[\frac{\lambda_n' A_{2,n}}{r^{1-\lambda_n'}} \left\{ \begin{matrix} (\lambda_n' + 1) \cdot \cos(\lambda_n' - 1)\theta - (\lambda_n' \cos 2\alpha + \\ \cos 2\lambda_n'\alpha) \cdot \cos(\lambda_n' + 1)\theta \end{matrix} \right\} \right] \tag{3.38}$$

$$\tau_{r\theta} = \sum_{n=1}^{\infty} \text{Re}\left[\frac{\lambda_n' A_{2,n}}{r^{1-\lambda_n'}} \left\{ \begin{matrix} (\lambda_n' - 1) \cdot \sin(\lambda_n' - 1)\theta - (\lambda_n' \cos 2\alpha + \\ \cos 2\lambda_n'\alpha) \cdot \sin(\lambda_n' + 1)\theta \end{matrix} \right\} \right] \tag{3.39}$$

Finally, stress components for symmetric loading condition (mode I) in the vicinity of the notch tip can be summarized as (after replacing $A_{2,n}$ by A_n)

$$\begin{Bmatrix} \sigma_r \\ \sigma_\theta \\ \tau_{r\theta} \end{Bmatrix} = \sum_{n=1}^{\infty} \text{Re}\left[\frac{\lambda_n' A_n}{r^{1-\lambda_n'}} \begin{Bmatrix} [(3 - \lambda_n') \cdot \cos(\lambda_n' - 1)\theta + (\lambda_n' \cdot \cos 2\alpha + \cos 2\lambda_n'\alpha) \cdot \cos(\lambda_n' + 1)\theta] \\ [(\lambda_n' + 1) \cdot \cos(\lambda_n' - 1)\theta - (\lambda_n' \cdot \cos 2\alpha + \cos 2\lambda_n'\alpha) \cdot \cos(\lambda_n' + 1)\theta] \\ [(\lambda_n' - 1) \cdot \sin(\lambda_n' - 1)\theta - (\lambda_n' \cdot \cos 2\alpha + \cos 2\lambda_n'\alpha) \cdot \sin(\lambda_n' + 1)\theta] \end{Bmatrix} \right] \tag{3.40}$$

3.1.2 Stress components in Cartesian coordinate system for mode I

Stress components in polar coordinates can be converted into a Cartesian coordinate system with the help of a transformation matrix $[T]$ as follows

$$\begin{Bmatrix}\sigma_x\\ \sigma_y\\ \tau_{xy}\end{Bmatrix}=\begin{bmatrix}\cos^2\theta & \sin^2\theta & -2\sin\theta\cos\theta\\ \sin^2\theta & \cos^2\theta & 2\sin\theta\cos\theta\\ \sin\theta\cos\theta & -\sin\theta\cos\theta & \cos^2\theta-\sin^2\theta\end{bmatrix}\begin{Bmatrix}\sigma_r\\ \sigma_\theta\\ \tau_{r\theta}\end{Bmatrix} \tag{3.41}$$

From Eq. (3.41) the stress components in the Cartesian coordinate system in mode I are

$$\sigma_x=\sigma_r\cos^2\theta+\sigma_\theta\sin^2\theta-2\tau_{r\theta}\sin\theta\cos\theta \tag{3.42}$$

$$\sigma_y=\sigma_r\sin^2\theta+\sigma_\theta\cos^2\theta+2\tau_{r\theta}\sin\theta\cos\theta \tag{3.43}$$

$$\tau_{xy}=\sigma_r\sin\theta\cos\theta-\sigma_\theta\sin\theta\cos\theta+\tau_{r\theta}\cos2\theta \tag{3.44}$$

Using Eq. (3.40), we have

$$\sigma_r\cos^2\theta=\sum_{n=1}^{\infty}\mathrm{Re}\left[\frac{A_n\lambda_n'}{r^{1-\lambda_n'}}\begin{pmatrix}\frac{(3-\lambda_n')}{4}\{\cos(\lambda_n'+1)\theta+2\cos(\lambda_n'-1)\theta+\cos(\lambda_n'-3)\theta\}\\ +\frac{X}{4}\{\cos(\lambda_n'+3)\theta+2\cos(\lambda_n'+1)\theta+\cos(\lambda_n'-1)\theta\}\end{pmatrix}\right] \tag{3.45}$$

where, the term $X=\lambda_n'\cos2\alpha+\cos2\lambda_n'\alpha$. Then,

$$\sigma_\theta\sin^2\theta=\sum_{n=1}^{\infty}\mathrm{Re}\left[\frac{A_n\lambda_n'}{r^{1-\lambda_n'}}\begin{pmatrix}\frac{(\lambda_n'+1)}{4}\cdot\{2\cos(\lambda_n'-1)\theta-\cos(\lambda_n'+1)\theta-\cos(\lambda_n'-3)\theta\}\\ -\frac{X}{4}\cdot\{2\cos(\lambda_n'+1)\theta-\cos(\lambda_n'-1)\theta-\cos(\lambda_n'+3)\theta\}\end{pmatrix}\right] \tag{3.46}$$

and

$$2\tau_{r\theta}\sin\theta\cos\theta=\sum_{n=1}^{\infty}\mathrm{Re}\left[\frac{A_n\lambda_n'}{r^{1-\lambda_n'}}\begin{pmatrix}\frac{(\lambda_n'-1)}{2}\cdot\{\cos(\lambda_n'-3)\theta-\cos(\lambda_n'+1)\theta\}-\\ \frac{X}{2}\cdot\{\cos(\lambda_n'-1)\theta-\cos(\lambda_n'+3)\theta\}\end{pmatrix}\right] \quad (3.47)$$

Finally, substituting Eq. (3.45), Eq. (3.46) and Eq. (3.47) in Eq. (3.42), we get

$$\sigma_x=\sum_{n=1}^{\infty}\mathrm{Re}\left[\frac{A_n\lambda_n'}{r^{1-\lambda_n'}}\begin{Bmatrix}(2+\lambda_n'\cdot\cos2\alpha+\cos2\lambda_n'\alpha)\cdot\cos(\lambda_n'-1)\theta-\\ (\lambda_n'-1)\cdot\cos(\lambda_n'-3)\theta\end{Bmatrix}\right] \quad (3.48)$$

Again using Eq. (3.40)

$$\sigma_r\sin^2\theta=\sum_{n=1}^{\infty}\mathrm{Re}\left[\frac{A_n\lambda_n'}{r^{1-\lambda_n'}}\begin{pmatrix}\frac{(3-\lambda_n')}{4}\cdot\{2\cos(\lambda_n'-1)\theta-\cos(\lambda_n'+1)\theta-\cos(\lambda_n'-3)\theta\}+\\ \frac{X}{4}\cdot\{2\cos(\lambda_n'+1)\theta-\cos(\lambda_n'+3)\theta-\cos(\lambda_n'-1)\theta\}\end{pmatrix}\right] \quad (3.49)$$

$$\sigma_\theta\cos^2\theta=\sum_{n=1}^{\infty}\mathrm{Re}\left[\frac{A_n\lambda_n'}{r^{1-\lambda_n'}}\begin{pmatrix}\frac{(\lambda_n'+1)}{4}\cdot\{\cos(\lambda_n'+1)\theta+2\cos(\lambda_n'-1)\theta+\cos(\lambda_n'-3)\theta\}-\\ \frac{X}{4}\cdot\{\cos(\lambda_n'+3)\theta+2\cos(\lambda_n'+1)\theta+\cos(\lambda_n'-1)\theta\}\end{pmatrix}\right] \quad (3.50)$$

Finally, by substituting Eq. (3.49), Eq. (3.50) and Eq. (3.47) in Eq. (3.43) and after simplifying, we get

$$\sigma_y=\sum_{n=1}^{\infty}\mathrm{Re}\left[\frac{A_n\lambda_n'}{r^{1-\lambda_n'}}\begin{pmatrix}\{2-\lambda_n'\cos2\alpha-\cos2\lambda_n'\alpha\}\cdot\cos(\lambda_n'-1)\theta\\ +(\lambda_n'-1)\cdot\cos(\lambda_n'-3)\theta\end{pmatrix}\right] \quad (3.51)$$

Again, using Eq. (3.40)

$$(\sigma_r - \sigma_\theta)\cdot\sin\theta\cdot\cos\theta = \frac{(1-\lambda_n')}{2}\cdot\{\sin(\lambda_n'+1)\theta - \sin(\lambda_n'-3)\theta\} + \frac{X}{2}\cdot\{\sin(\lambda_n'+3)\theta - \sin(\lambda_n'-1)\theta\} \tag{3.52}$$

also,

$$\tau_{r\theta}\cdot\cos 2\theta = \frac{(\lambda_n'-1)}{2}\cdot\sin(\lambda_n'-3)\theta + \frac{(\lambda_n'-1)}{2}\cdot\sin(\lambda_n'+1)\theta - \frac{X}{2}\cdot\sin(\lambda_n'-1)\theta - \frac{X}{2}\cdot\sin(\lambda_n'+3)\theta \tag{3.53}$$

Finally, by substituting Eq. (3.52) and Eq. (3.53) in Eq. (3.44), and simplifying again, we get

$$\tau_{xy} = \sum_{n=1}^{\infty}\mathrm{Re}\left[\frac{A_n\lambda_n'}{r^{1-\lambda_n'}}\left((\lambda_n'-1)\cdot\sin(\lambda_n'-3)\theta - \{\lambda_n'\cdot\cos 2\alpha + \cos 2\lambda_n'\alpha\}\cdot\sin(\lambda_n'-1)\theta\right)\right] \tag{3.54}$$

Hence, Cartesian stress components in mode I are

$$\begin{Bmatrix}\sigma_x\\ \sigma_y\\ \tau_{xy}\end{Bmatrix} = \sum_{n=1}^{\infty}\mathrm{Re}\left[\frac{A_n\lambda_n'}{r^{1-\lambda_n'}}\begin{Bmatrix}[(2+\lambda_n'\cdot\cos 2\alpha + \cos 2\lambda_n'\alpha)\cdot\cos(\lambda_n'-1)\theta - (\lambda_n'-1)\cdot\cos(\lambda_n'-3)\theta]\\ [(2-\lambda_n'\cdot\cos 2\alpha - \cos 2\lambda_n'\alpha)\cdot\cos(\lambda_n'-1)\theta + (\lambda_n'-1)\cdot\cos(\lambda_n'-3)\theta]\\ [-(\lambda_n'\cdot\cos 2\alpha + \cos 2\lambda_n'\alpha)\cdot\sin(\lambda_n'-1)\theta + (\lambda_n'-1)\cdot\sin(\lambda_n'-3)\theta]\end{Bmatrix}\right] \tag{3.55}$$

3.1.3 Strain components in Cartesian coordinate system in mode I

Assuming plane stress conditions, the relationship between stresses and strains are given by

$$\varepsilon_x = \frac{\sigma_x}{E} - \frac{\nu}{E}\sigma_y = \frac{1}{E}(\sigma_x - \nu\sigma_y) \tag{3.56}$$

$$\varepsilon_y = \frac{1}{E}\left(\sigma_y - \nu\sigma_x\right) \tag{3.57}$$

$$\gamma_{xy} = \frac{\tau_{xy}}{G} \tag{3.58}$$

Substituting Eq. (3.55) in Eq. (3.56), Eq. (3.57) and Eq. (3.58), the strain components under mode I condition at any point $P(r,\theta)$ (Figure 3.1) are given by

$$\begin{aligned}
2G\varepsilon_x &= \sum_{n=1}^{\infty}\mathrm{Re}\left[\frac{A_n'\lambda_n'}{r^{1-\lambda_n'}}\begin{Bmatrix}2\kappa\cos\left(\lambda_n'-1\right)\theta+\lambda_n'.\cos 2\alpha.\cos\left(\lambda_n'-1\right)\theta+\\ \cos 2\lambda_n'\alpha.\cos\left(\lambda_n'-1\right)\theta-\left(\lambda_n'-1\right).\cos\left(\lambda_n'-3\right)\theta\end{Bmatrix}\right]\\
2G\varepsilon_y &= \sum_{n=1}^{\infty}\mathrm{Re}\left[\frac{A_n'\lambda_n'}{r^{1-\lambda_n'}}\begin{Bmatrix}2\kappa\cos\left(\lambda_n'-1\right)\theta-\lambda_n'.\cos 2\alpha.\cos\left(\lambda_n'-1\right)\theta-\\ \cos 2\lambda_n'\alpha.\cos\left(\lambda_n'-1\right)\theta+\left(\lambda_n'-1\right).\cos\left(\lambda_n'-3\right)\theta\end{Bmatrix}\right]\\
2G\gamma_{xy} &= \sum_{n=1}^{\infty}\mathrm{Re}\left[\frac{A_n'\lambda_n'}{r^{1-\lambda_n'}}\begin{Bmatrix}2\left(\lambda_n'-1\right).\sin\left(\lambda_n'-3\right)\theta-\\ 2\left(\lambda_n'\cos 2\alpha+\cos 2\lambda_n'\alpha\right).\sin\left(\lambda_n'-1\right)\theta\end{Bmatrix}\right]
\end{aligned} \tag{3.59}$$

where Kolosov's constant $\kappa = (1-\nu)/(1+\nu)$ for plane stress and $3-\nu$ for plane strain conditions and G is the shear modulus of rigidity. The strain series in Eq. (3.59) contains an infinite number of terms. For complete understanding of Eq. (3.59), it is important to know the characteristics of the Williams' coefficients A_n' and λ_n'. Their nature has been explained in detail in the next chapter.

3.2 Point substitution displacement technique

The point substitution displacement technique proposed by Hussain and Murthy [54] is briefly presented here. This technique has been used for computation of NSIFs of various configurations of the present work. The displacement field around the notch tip for mode I loading can be given as,

$$u = \sum_{n=1}^{\infty} Re\left[\frac{A_n'}{2G} r^{\lambda_n'} \{(\kappa + \lambda_n' \cos 2\alpha + \cos 2\alpha \lambda_n') \cos \lambda_n' \theta - \lambda_n' \cos(\lambda_n' - 2)\theta\}\right] + u_R \quad (3.60)$$

and

$$v = \sum_{n=1}^{\infty} Re\left[\frac{A_n'}{2G} r^{\lambda_n'} \{(\kappa - \lambda_n' \cos 2\alpha - \cos 2\alpha \lambda_n') \sin \lambda_n' \theta + \lambda_n' \sin(\lambda_n' - 2)\theta\}\right] \quad (3.61)$$

where u and v are the displacement components in the x and y directions, κ is the Kolosov constant and λ_n' is the mode I eigenvalue. The term u_R in Eq. (3.60) is an integration constant representing rigid body translation part of the u -displacement field in the mode I loading. No such term exists in the v -displacement field of the mode I loading. The term u_R can be expressed as

$$u_R = \frac{\kappa + 1}{2G} A_0 \quad (3.62)$$

where A_0 is the Williams' coefficient corresponding to the rigid body motion.

Taking into account only the first term of the infinite series, the notch opening displacement (NOD) for mode I loading can be obtained as

$$\begin{aligned} \Delta v = v_{\theta=+\alpha} - v_{\theta=-\alpha} = 2v_{\theta=+\alpha} &= 2\frac{A_1}{2G} r^{\lambda_1} \begin{bmatrix} (\kappa - \lambda_1 \cos 2\alpha - \cos 2\alpha \lambda_1) \sin \lambda_1 \alpha \\ + \lambda_1 \sin(\lambda_1 - 2)\alpha \end{bmatrix} \\ &= 2A_1 C_1 r^{\lambda_1} \end{aligned} \quad (3.63)$$

where Δv is the notch opening displacement, C_1 is a constant which is dependent on the notch angle, eigenvalue and κ. Thus, at any loading condition, A_1 can be determined from the NOD equation (Eq. (3.63)).

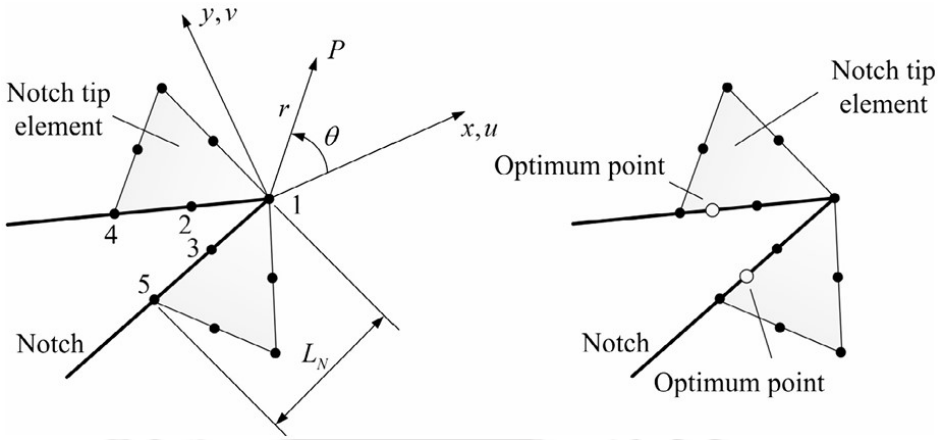

(a) **(b)**

Figure 3.2 A typical mesh around a notch tip.

Considering one of the notch tip elements that contains the notch flanks as shown in Fig.3.2, the finite element displacement distribution along the line say 1–2–4 in the notch tip local coordinate system can be expressed as

$$v^{FE}_{\theta=+\alpha} = Ar^2 + Br \tag{3.64}$$

where r is the distance from the notch tip $(0 \le r \le L_N)$, L_N is the length of the notch tip element, and A and B are constants which can be determined from the nodal displacements at nodes 2 and 4 as

$$\begin{Bmatrix} A \\ B \end{Bmatrix} = \begin{bmatrix} r_2^2 & r_2 \\ r_4^2 & r_4 \end{bmatrix}^{-1} \begin{Bmatrix} v_2^{FE} \\ v_4^{FE} \end{Bmatrix} \tag{3.65}$$

where r_2 and r_4 are radial distances from the notch tip to nodes 2 and 4 respectively. Therefore, the FE value of NOD can be expressed as

$$\Delta v^{FE} = 2Ar^2 + 2Br \tag{3.66}$$

Now, the residual R between the analytical NOD (Eq. (3.63)) and the FE NOD (Eq. 3.66) can be expressed as

$$R = (\Delta v - \Delta v^{FE})^2 = (2A_1C_1r^{\lambda_1} - 2Ar^2 - 2Br)^2 \tag{3.67}$$

For minimum value of R

$$\frac{\partial R}{\partial r} = 0 \tag{3.68}$$

which simplifies to two simultaneous equations as

$$Ar^2 + Br = A_1C_1r^{\lambda_1} \tag{3.69}$$

and

$$2Ar + B = \lambda_1 A_1 C_1 r^{\lambda_1 - 1} \tag{3.70}$$

By solving the above two equations, r and A_1 can be obtained as

$$r = r_{op} = -\frac{B(1-\lambda_1)}{A(2-\lambda_1)} \tag{3.71}$$

$$A_1 = \frac{Ar_{op}^2 + Br_{op}}{C_1 r_{op}^{\lambda_1}} = \frac{\Delta v^{FE}|_{r=r_{op}}}{C_1 r_{op}^{\lambda_1}} \tag{3.72}$$

In the above equation, A and B can be determined using Eq. (3.65). Using the value of A_1 from Eq. (3.72), mode I NSIF can be calculated as shown using Eq. (4.12) in the next chapter. Thus, after determining the r_{op} using Eq. (3.71) and $\Delta v^{FE}|_{r=r_{op}}$ at a single point r_{op} (optimum radius), the mode I NSIF can be estimated. Here, $\Delta v^{FE}|_{r=r_{op}}$ can be

interpolated at r_{op} using the shape functions and nodal displacements or using Eq. (3.66). It has been shown [54] that very accurate mode I NSIFs can be determined even with the coarse FE meshes by simple substitution of Δv^{FE} at r_{op} in Eq. (3.72).

3.3 A brief description of the finite elements employed

In the present work, linear elastic 2D and 3D finite element analyses of several V-notched configurations have been carried out using displacement-based FE method. For this purpose, commercial software ANSYS® has been utilized. In the present investigation two types of elements have been used viz., PLANE 183 and SOLID 186. These two elements are widely used in fracture mechanics for 2D and 3D elastic analysis, respectively. The PLANE 183 element is a higher-order, two-dimensional and eight nodded isoparametric quadrilateral element (Q8) as shown in Fig.3.3. This element can be used for both the plane stress and plane strain conditions. It has two degrees of freedom per node.

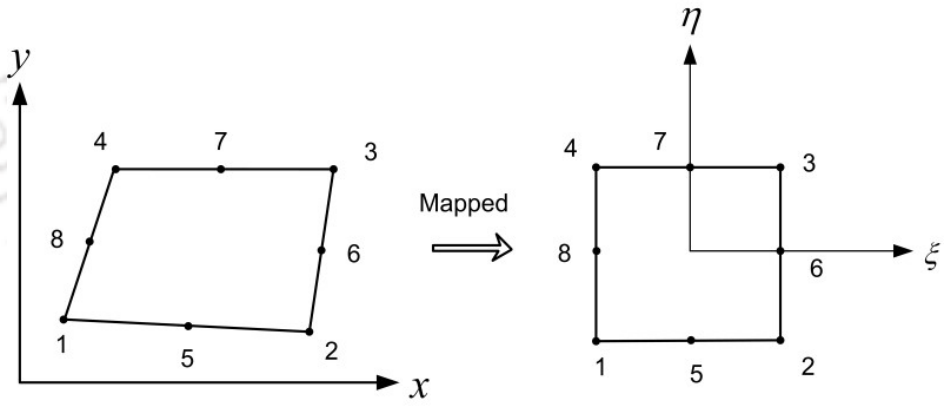

Figure 3.3 Eight nodded quadrilateral isoparametric element.

Shape function must be expressed in a natural coordinate system for numerical integration. Natural coordinate systems (ξ,η) are dimensionless and possess a maximum absolute magnitude of unity. They are defined with respect to the element rather than with respect to the global coordinate system (x,y) encompassing the element (Fig.3.3). The shape functions for a Q8 element are expressed in terms of natural coordinates (ξ,η) as

$$
\begin{aligned}
N_1 &= \frac{1}{4}(1+\xi)(1-\eta)-\frac{1}{2}(N_8+N_5) & N_5 &= \frac{1}{2}(1-\xi^2)(1-\eta)\\
N_2 &= \frac{1}{4}(1-\xi)(1+\eta)-\frac{1}{2}(N_5+N_6) & N_6 &= \frac{1}{2}(1+\xi)(1-\eta^2)\\
N_3 &= \frac{1}{4}(1-\xi)(1-\eta)-\frac{1}{2}(N_6+N_7) & N_7 &= \frac{1}{2}(1-\xi^2)(1-\eta)\\
N_4 &= \frac{1}{4}(1+\xi)(1-\eta)-\frac{1}{2}(N_7+N_8) & N_8 &= \frac{1}{2}(1+\xi)(1-\eta^2)
\end{aligned}
\tag{3.73}
$$

Another element employed in the present investigation is SOLID 186 which is twenty nodded quadrilateral isoparametric elements (Q20) having three degrees of freedom (DOF) per node (Fig.3.4). It is very widely employed in 3D elastic FE analysis of components. Q20 elements are often used when a high degree of accuracy is needed to model complex stress distributions, large deformations, or other detailed phenomena within the material. The twenty-nodded isoparametric quadrilateral element (Fig.3.4) has the following nodes (a) 4 bottom-face corner nodes (1, 2, 3, 4), (b) 4 top-face corner nodes (5, 6, 7, 8), (c) 8 edge nodes (9, 10, 11, 12, 13, 14, 15, 16) and (d) 4 internal nodes (17, 18, 19, 20).

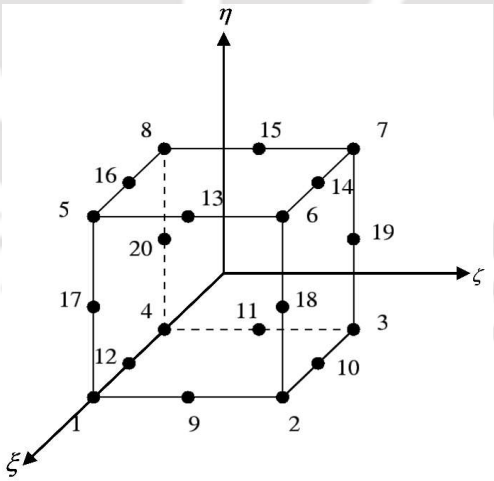

Figure 3.4 Twenty nodded quadrilateral isoparametric element.

The shape functions are quadratic in nature. The shape functions $N_{i(i=1,2,3,...)}$ for the twenty-nodded element are given by

- **Bottom-face corner nodes (Nodes 1, 2, 3, 4):**

$$\begin{aligned} N_1 &= \frac{1}{4}(1-\xi)(1-\eta)(-\xi-\eta-\xi\eta-1) \\ N_2 &= \frac{1}{4}(1+\xi)(1-\eta)(\xi-\eta+\xi\eta-1) \\ N_3 &= \frac{1}{4}(1+\xi)(1+\eta)(\xi+\eta-\xi\eta-1) \\ N_4 &= \frac{1}{4}(1-\xi)(1+\eta)(-\xi+\eta+\xi\eta-1) \end{aligned} \tag{3.74}$$

- **Top-face corner nodes (Nodes 5, 6, 7, 8):**

$$\begin{aligned} N_5 &= \frac{1}{2}(1-\xi^2)(1-\eta)(1-\eta) \\ N_6 &= \frac{1}{2}(1+\xi)(1-\eta^2)(1+\xi) \\ N_7 &= \frac{1}{2}(1-\xi^2)(1+\eta)(1+\eta) \\ N_8 &= \frac{1}{2}(1-\xi)(1-\eta^2)(1-\xi) \end{aligned} \tag{3.75}$$

- **Edge nodes (Nodes 9, 10, 11, 12, 13, 14, 15, 16):**

$$\begin{aligned} N_9 &= \frac{1}{2}(1-\xi^2)(1-\eta)(1+\xi)(1-\eta) \\ N_{10} &= \frac{1}{2}(1+\xi)(1-\eta^2)(1-\xi)(1-\eta) \\ N_{11} &= \frac{1}{2}(1-\xi^2)(1+\eta)(1-\xi)(1+\eta) \\ N_{12} &= \frac{1}{2}(1-\xi)(1-\eta^2)(1+\xi)(1+\eta) \\ N_{13} &= \frac{1}{2}(1-\xi)(1-\eta^2)(1+\xi) \\ N_{14} &= \frac{1}{2}(1+\xi)(1-\eta^2)(1-\xi) \\ N_{15} &= \frac{1}{2}(1-\xi^2)(1+\eta)(1-\xi) \\ N_{16} &= \frac{1}{2}(1-\xi^2)(1-\eta)(1+\eta) \end{aligned} \tag{3.76}$$

- **Internal nodes (Nodes 17, 18, 19, 20):**

$$
\begin{aligned}
N_{17} &= \frac{1}{2}(1-\xi^2)(1-\eta^2)(1-\xi)(1+\eta) \\
N_{18} &= \frac{1}{2}(1-\xi^2)(1-\eta^2)(1+\xi)(1+\eta) \\
N_{19} &= \frac{1}{2}(1-\xi^2)(1-\eta^2)(1-\xi)(1-\eta) \\
N_{20} &= \frac{1}{2}(1-\xi^2)(1-\eta^2)(1+\xi)(1-\eta)
\end{aligned}
\tag{3.77}
$$

Finite element formulation for 2D and 3D elastic analysis of a body remains same and is available in any standard textbooks on finite element analysis and therefore not repeated here.

3.4 Summary

This chapter discussed the theoretical background required for determining the state of the stress at the notch tip by using the generalized Williams' eigenfunction expansion approach. The notch tip's stress field exhibits $1/r^{1-\lambda}$ singularity, which is characterized by the notch stress intensity factor (NSIF) K_I^V. The generalized formulations for the state of the stress under the mode I loading condition at any point around the notch tip have been shown in the form of infinite series followed by the corresponding strain formulations. Subsequently, brief details of the finite element analyses and numerical determination of the NSIFs incorporated in the presented thesis work, have also been provided at the end of the chapter.

Chapter 4

Proposed single strain gage technique and valid gage locations

This chapter presents the mathematical formulations of the proposed strain gage technique aimed to determine accurate mode I NSIFs of sharp V-notched bodies. Detailed mathematical formulations of (a) the proposed single strain gage technique and (b) valid gage locations are presented in this chapter. Finally, a self-explanatory flowchart has been shown for better understanding of the proposed technique.

4.1 Formulation of the proposed single strain gage technique

The proposed strain gage technique for the sharp V-notched bodies is developed consistent with the approach outlined by Dally and Sanford [36] for the crack problems. As a consequence, as shown later, only a single strain gage is sufficient for the accurate determination of the mode I NSIF by placing it at distant locations from the notch tip. Such a provision, as stated previously, avoids neatly the notch tip complications.

Let us consider an arbitrary 2D body having a sharp V-notch and subjected to mode I loading as shown in Fig.4.1(a). The material of the body is homogenous and isotropic. Referring to Fig.4.1(a), the direction a represents the axis of the strain gage and β is the orientation of the gage with respect to the axis of the notch at point a $P(r,\theta)$. The normal strain ε_a in the direction of β at $P(r,\theta)$ can be obtained using strain transformation law as

$$\begin{Bmatrix} \varepsilon_a \\ \varepsilon_{a'} \\ \gamma_{aa'} \end{Bmatrix} = [R][T][R]^{-1} \begin{Bmatrix} \varepsilon_x \\ \varepsilon_y \\ \gamma_{xy} \end{Bmatrix} \tag{4.1}$$

where,

$$[R]=\begin{bmatrix}1 & 0 & 0\\ 0 & 1 & 0\\ 0 & 0 & 2\end{bmatrix} \tag{4.2}$$

and

$$[T]=\begin{bmatrix}c^2 & s^2 & 2sc\\ s^2 & c^2 & -2sc\\ -sc & sc & c^2-s^2\end{bmatrix} \tag{4.3}$$

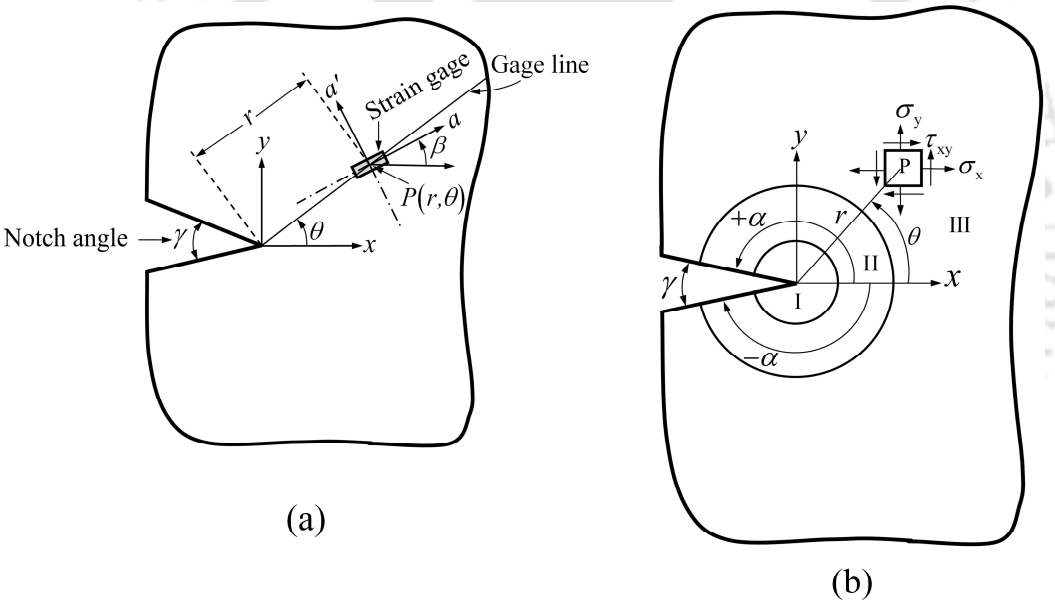

Figure 4.1 (a) Coordinate system and orientation of a strain gage in a sharp V-notched body; (b) different zones ahead of a notch tip.

Using Eq. (4.2) and Eq. (4.3)

$$[R][T][R]^{-1}=\begin{bmatrix}c^2 & s^2 & sc\\ s^2 & c^2 & -sc\\ -2sc & 2sc & c^2-s^2\end{bmatrix} \tag{4.4}$$

Substituting Eq. (4.4) in Eq. (4.1)

$$\begin{Bmatrix} \varepsilon_a \\ \varepsilon_{a'} \\ \gamma_{aa'} \end{Bmatrix} = \begin{bmatrix} c^2 & s^2 & sc \\ s^2 & c^2 & -sc \\ -2sc & 2sc & c^2 - s^2 \end{bmatrix} \begin{Bmatrix} \varepsilon_x \\ \varepsilon_y \\ \gamma_{xy} \end{Bmatrix} \tag{4.5}$$

Thus, the normal strain in the direction of β at any point $P(r,\theta)$ can be obtained as

$$\varepsilon_a = \cos^2\beta.\varepsilon_x + \sin^2\beta.\varepsilon_y + \sin\beta.\cos\beta.\gamma_{xy} \tag{4.6}$$

Multiplying by $2G$ on both sides of the Eq. (4.6)

$$2G\varepsilon_a = \cos^2\beta.(2G\varepsilon_x) + \sin^2\beta.(2G\varepsilon_y) + \sin\beta.\cos\beta.(2G\gamma_{xy}) \tag{4.7}$$

Expanding all three strain series of Eq. (3.59) up to two terms and then substituting in Eq. (4.7), and subsequently rearranging the term, we get

$$\begin{aligned}
2G\varepsilon_a = {} & \cos^2\beta.\mathrm{Re}\left[\frac{A_1'\lambda_1'}{r^{1-\lambda_1'}}\begin{Bmatrix} 2\kappa\cos(\lambda_1'-1)\theta + \lambda_1'.\cos(2\pi-\gamma).\cos(\lambda_1'-1)\theta + \\ \cos\lambda_1'(2\pi-\gamma).\cos(\lambda_1'-1)\theta - (\lambda_1'-1).\cos(\lambda_1'-3)\theta \end{Bmatrix}\right] \\
& + \sin^2\beta.\mathrm{Re}\left[\frac{A_1'\lambda_1'}{r^{1-\lambda_1'}}\begin{Bmatrix} 2\kappa\cos(\lambda_1'-1)\theta - \lambda_1'.\cos(2\pi-\gamma).\cos(\lambda_1'-1)\theta - \\ \cos\lambda_1'(2\pi-\gamma).\cos(\lambda_1'-1)\theta + (\lambda_1'-1).\cos(\lambda_1'-3)\theta \end{Bmatrix}\right] \\
& + \frac{1}{2}\sin 2\beta.\mathrm{Re}\left[\frac{A_1'\lambda_1'}{r^{1-\lambda_1'}}\left\{2(\lambda_1'-1).\sin(\lambda_1'-3)\theta - 2\begin{pmatrix} \lambda_1'\cos(2\pi-\gamma) + \\ \cos\lambda_1'(2\pi-\gamma) \end{pmatrix}.\sin(\lambda_1'-1)\theta\right\}\right] \\
& + \cos^2\beta.\mathrm{Re}\left[\frac{A_2'\lambda_2'}{r^{1-\lambda_2'}}\begin{Bmatrix} 2\kappa\cos(\lambda_2'-1)\theta + \lambda_2'.\cos(2\pi-\gamma).\cos(\lambda_2'-1)\theta + \\ \cos\lambda_2'(2\pi-\gamma).\cos(\lambda_2'-1)\theta - (\lambda_2'-1).\cos(\lambda_2'-3)\theta \end{Bmatrix}\right] \\
& + \sin^2\beta.\mathrm{Re}\left[\frac{A_2'\lambda_2'}{r^{1-\lambda_2'}}\begin{Bmatrix} 2\kappa\cos(\lambda_2'-1)\theta - \lambda_2'.\cos(2\pi-\gamma).\cos(\lambda_2'-1)\theta - \\ \cos\lambda_2'(2\pi-\gamma).\cos(\lambda_2'-1)\theta + (\lambda_2'-1).\cos(\lambda_2'-3)\theta \end{Bmatrix}\right] \\
& + \frac{1}{2}\sin 2\beta.\mathrm{Re}\left[\frac{A_2'\lambda_2'}{r^{1-\lambda_2'}}\left\{2(\lambda_2'-1).\sin(\lambda_2'-3)\theta - 2\begin{pmatrix} \lambda_2'\cos(2\pi-\gamma) + \\ \cos\lambda_2'(2\pi-\gamma) \end{pmatrix}.\sin(\lambda_2'-1)\theta\right\}\right]
\end{aligned} \tag{4.8}$$

As mentioned in the previous chapter, it is worth studying here the characteristics of the Williams' coefficients A_n' and λ_n'. The characteristic equation under mode I conditions (Eq. 3.31) is given by

$$\lambda_n' \sin 2\alpha + \sin 2\lambda_n'\alpha = 0 \tag{4.9}$$

The positive root of the above equation λ_n' defines the order of singularity ahead of the notch tip in mode I loading which depends on the value of α (Fig. 4.1(b)) and therefore is a function of the notch angle γ. Usually, numerical methods are employed to solve Eq. (4.9). The eigenvalue, λ_n' can be a real or a complex number depending on the notch angle and can be written as

$$\lambda_n' = \lambda_n + i\lambda_n^* \tag{4.10}$$

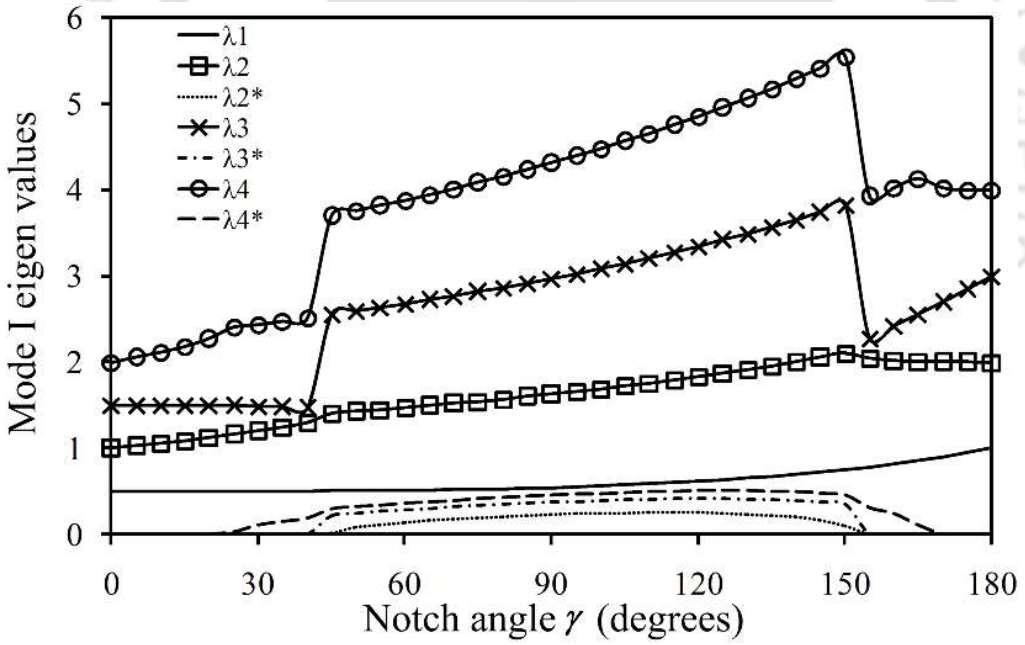

Figure 4.2 First four mode I eigenvalues as a function of notch angle γ.

Figure 4.2 shows the variation of the first four eigenvalues with the notch angle. It can be noticed from the Fig. 4.2 that the first eigenvalue λ_1' is always real (i.e., $\lambda_1' = \lambda_1$ and $\lambda_1^* = 0$) and less than unity until $\gamma < 180°$ indicating singular stress behavior, and

$\gamma = 180°$ represents a solid with no notch i.e., $1-\lambda_1 = 0$ in Eq. (3.40). As shown in Fig. 4.2, the second and higher-order values of λ_n' will be a real or complex number depending on the notch angle. Since the stresses must be real values, the coefficients of Williams' expansion A_n' can be either real or complex numbers depending on the notch eigenvalues. Indeed, it can be shown that [65] real and complex values of coefficients A_n' can be acquired for real and complex values of λ_n' respectively. Therefore, the Williams coefficients A_n' can also be written as

$$A_n' = A_n + iA_n^* \tag{4.11}$$

For $n=1$, the coefficient $A_1' = A_1$ ($A_1^* = 0$ because $\lambda_1^* = 0$ for $n=1$) represents the singular term and is related to the NSIF K_I^V as follows [65]

$$K_I^V = \lim_{r\to 0}(\sqrt{2\pi} r^{1-\lambda_1}\sigma_y(\theta=0)) = \sqrt{2\pi}\lambda_1(1+\lambda_1-\lambda_1\cos 2\alpha - \cos 2\alpha\lambda_1)A_1 \tag{4.12}$$

For $n>1$, A_n' are non-singular higher order coefficients. Referring to Eq. (3.59), the strain components containing terms corresponding to $n=1$ and $n=2$ can be expressed as

$$\begin{aligned}
2G\varepsilon_x &= r^{\lambda_1-1}A_1 g_1^x(\lambda_1,\nu,\theta,\gamma) + r^{\lambda_2-1}A_2 g_2^x(r,\lambda_2^*,\lambda_2,\theta,\gamma,\nu) + r^{\lambda_2-1}A_2^* g_2^{x*}(r,\lambda_2^*,\lambda_2,\theta,\gamma,\nu)\\
2G\varepsilon_y &= r^{\lambda_1-1}A_1 g_1^y(\lambda_1,\nu,\theta,\gamma) + r^{\lambda_2-1}A_2 g_2^y(r,\lambda_2^*,\lambda_2,\theta,\gamma,\nu) + r^{\lambda_2-1}A_2^* g_2^{y*}(r,\lambda_2^*,\lambda_2,\theta,\gamma,\nu)\\
2G\gamma_{xy} &= r^{\lambda_1-1}A_1 g_1^{xy}(\lambda_1,\theta,\gamma) + r^{\lambda_2+1}A_2 g_2^{xy}(r,\lambda_2^*,\lambda_2,\theta,\gamma) + r^{\lambda_2+1}A_2^* g_2^{xy*}(r,\lambda_2^*,\lambda_2,\theta,\gamma)
\end{aligned} \tag{4.13}$$

It can be noticed from the above equation that the real-valued strain components now contain three unknown coefficients A_1, A_2 and A_2^* for a given notched body. It is worth mentioning here that, while obtaining the real-valued series in Eq. (4.13) from the complex-valued series in Eq. (3.59), the expansion of the complex number $r^{1-\lambda_n'}$ leads to the appearance of the term $\lambda_n^* \ln(r)$ in Eq. (4.13). As a consequence, the function g_2 in Eq. (4.13) is also a function of r. Unlike the function g_2, the function g_1 in the first

term of expressions in Eq. (4.13) is independent of r as the first eigenvalue is always real (i.e., $\lambda_1' = \lambda_1$).

For practical measurement of surface strains using strain gages, it is necessary to identify an appropriate zone around the notch tip. A small zone around the notch tip such as zone I (Fig.4.1(b)) is not a suitable zone for practical measurement of strains due to the high strain gradients, plasticity effects and 3D state of stress. The farthest zone such as zone III is also not a feasible zone for the strain measurements. This is because, large number of unknown coefficients has to be employed in the strain series for representation of the strains at those distant locations and which may also require large number of strain gages. Moreover, singular field may not prevail at such distances. Therefore, the intermediate zone or zone II (Fig.4.1(b)) is a practically feasible region for strain measurements. In the present investigation, it is assumed that zone II is the region around the notch tip in which strains can be accurately represented by the multiparameter strain series given by Eq. (4.8) which comprises a singular term (A_1) plus two non-singular higher-order terms (A_2 and A_2^*). Accordingly, the normal strain component ε_a along the direction a subtending an angle β with the notch axis at a point P can be expressed as

$$2G\varepsilon_a = r^{\lambda_1-1}A_1 f_1\left(\theta,\beta,\lambda_1,\nu,\gamma\right) + r^{\lambda_2-1}A_2 f_2\left(\theta,\beta,\lambda_2,\lambda_2^*,\gamma,\nu,r\right) + r^{\lambda_2-1}A_2^* f_2^*\left(\theta,\beta,\lambda_2,\lambda_2^*,\gamma,\nu,r\right) \tag{4.14}$$

where the functions f_1, f_2 and f_2^* are given in **Appendix-A.** If A_1 is measured using Eq. (4.14), then the mode I NSIF K_I^V can then be determined using Eq. (4.12). One straightforward approach is to use three strain gages corresponding to the three unknown coefficients A_1, A_2 and A_2^* such that three simultaneous equations can be obtained using Eq. (4.14) to solve for A_1, A_2 and A_2^* and hence the mode I NSIF K_I^V.

Nevertheless, the measurement of K_I^V can be simplified by an efficient manipulation of Eq. (4.14) as follows. Eq. (4.14) can be further simplified by making the coefficient of the term A_2

$$f_2\left(\theta,\beta,\lambda_2,\lambda_2^*,\gamma,\nu,r\right)=0 \tag{4.15}$$

and term A_2^*

$$f_2^*\left(\theta,\beta,\lambda_2,\lambda_2^*,\gamma,\nu,r\right)=0 \tag{4.16}$$

Two distinct cases are possible while solving Eq. (4.15) and Eq. (4.16). It is important to observe from Fig.4.2 that for the notch angles less than or equal to 40° (approximately), λ_2' is real (i.e. $\lambda_2'=\lambda_2$) and hence λ_2^* and consequently A_2^* vanish in Eq. (4.14). Thus, ε_a in Eq. (4.14) contains only the coefficients associated with the terms A_1 and A_2. As a consequence, Eq. (4.15) alone needs to be satisfied for $\gamma \le 40°$ and Eq. (4.16) is automatically satisfied due to $\lambda_2^*=0$. For $\gamma \le 40°$, for a given value of Poisson's ratio ν, infinite sets of θ and β can result as a solution of Eq. (4.15). Figure 4.3 shows the values of β after solving Eq. (4.15) for selected values of $\nu(=1/3)$ and θ.

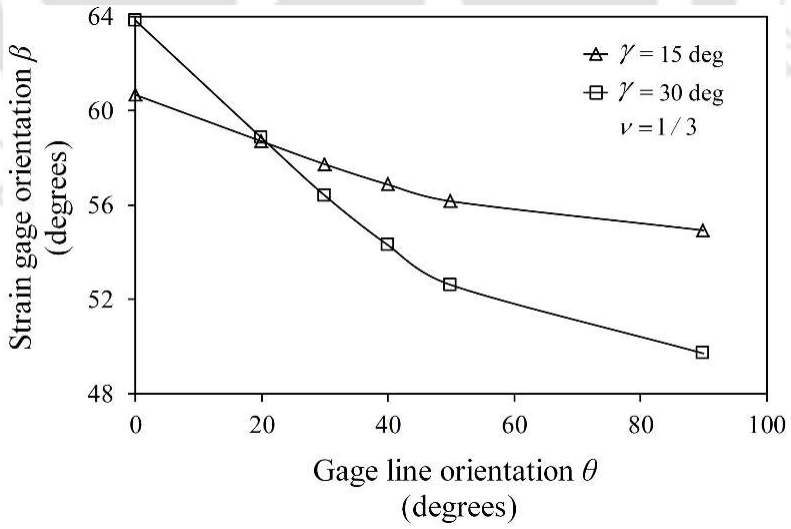

Figure 4.3 Variation of strain gage orientation β with gage line orientation θ for notch angles $\gamma = 15°$ and $30°$, and Poisson's ratio $\nu = 1/3$.

It can be noticed from Fig.4.3 that as θ increases β decreases. The $\ln(r)$ term in the function f_2 (corresponding to term A_2) in Eq. (4.15) does not affect the solution as it is multiplied by λ_2^* everywhere, which is zero for $\gamma \le 40°$ and thus the normal strain ε_a (with $f_2 = 0$ and $f_2^* = 0$) for a particular set of θ and β values is given by

$$2G\varepsilon_a = r^{\lambda_1 - 1} A_1 f_1(\theta, \beta, \lambda_1, \nu, \gamma) \tag{4.17}$$

where,

$$f_1(\theta,\beta,\lambda_1,\nu,\gamma) = \lambda_1 \begin{Bmatrix} \cos^2\beta\left[\cos\theta(\lambda_1-3)+\cos\theta(\lambda_1-1)\left[2\kappa+\cos\lambda_1(6.2832-\gamma)\right]\right]- \\ \cos\theta(\lambda_1-3)\sin^2\beta+2\kappa\cos\theta(\lambda_1-1)\sin^2\beta- \\ \cos\theta(\lambda_1-1)\cos\lambda_1(6.2832-\gamma)\sin^2\beta- \\ \sin\theta(\lambda_1-3)\sin 2\beta-\cos\lambda_1(6.2832-\gamma)\sin\theta(\lambda_1-1)\sin 2\beta- \\ \lambda_1\cos^2\beta\cos\theta(\lambda_1-3)+\lambda_1\cos^2\beta\cos\gamma\cos\theta(\lambda_1-1)+ \\ \lambda_1\cos\theta(\lambda_1-3)\sin^2\beta-\lambda_1\cos\gamma\cos\theta(\lambda_1-1)\sin^2\beta+ \\ \lambda_1\sin\theta(\lambda_1-3)\sin 2\beta-\lambda_1\cos\gamma\sin\theta(\lambda_1-1)\sin 2\beta \end{Bmatrix} \tag{4.18}$$

Eq. (4.17) now contains only one unknown coefficient A_1 which can be measured using a single strain gage laid upon the gage line as shown in Fig.4.1(a). Here we define the gage line as the line which makes an angle θ with the notch axis and on which strain gage needs to be pasted in the direction of β at a radial distance r from the notch tip (Fig.4.1(a)). Thus, using a single strain gage, by placing it at a point defined by (r,θ) along the gage line and orienting it at an angle of β to the notch axis, one can easily determine the mode I notch SIF K_I^V using Eq. (4.17) and Eq. (4.12). It should be noted that though Eq. (4.17) contains only one coefficient, but the equation on the right-hand side is indeed a three-parameter representation of ε_a as shown in the Eq. (4.14). As a result, a strain gage can be placed at longer distances from the notch tip which would minimize various effects arising at the notch tip in the strain gage techniques.

Now considering the case of $\gamma > 40°$, both the Eqs. (4.15) and (4.16) need to be solved simultaneously for the unique values of θ and β for a given Poisson's ratio ν. This is because, λ_2^* does not vanish for $\gamma > 40°$ and ε_a (Eq. (4.14)) contains all the

three terms A_1, A_2 and A_2^*. In the present investigation, Mathematica® is employed to solve these transcendental equations (Eqs. (4.15) and (4.16)). It is important to note that as $\lambda_2^* \neq 0$ for $\gamma > 40°$, the $\ln(r)$ term multiplied by λ_2^* in Eqs. (4.15) and (4.16) does not vanish. However, it has been observed that, for a given Poisson's ratio, the same values of θ and β can be obtained irrespective of the values of r chosen in Eqs. (4.15) and (4.16) for $\gamma > 40°$. Thus, similar to the case of $\gamma \leq 40°$, the term $\ln(r)$ does not affect the solution even when $\gamma > 40°$ and in fact, it is not necessary to provide any value of r for solving Eqs. (4.15) and (4.16) simultaneously.

Figure 4.4 shows the plot of θ and β as a function of notch angle $\gamma(> 40°)$ for a typical value of Poisson's ratio $\nu(=1/3)$.This is obtained from the solution of Eqs. (4.15) and (4.16). Thus, for $\gamma > 40°$, with this set of θ and β, Eq. (4.14) will get reduced once again to Eq. (4.17) containing only one unknown coefficient A_1. Clearly, once again using a single strain gage by locating it at a point $P(r,\theta)$ along the gage line defined by θ and orienting the gage along the direction defined by β to the notch axis, A_1 coefficient can be easily measured upon equating the measured strain with Eq. (4.17) for $\gamma > 40°$. Then by using Eq. (4.12), the mode I NSIF K_I^V can be determined. It can be noticed that, in the proposed strain gage technique only a single strain gage is sufficient to measure K_I^V of sharp V-notches for all the values of notch angles. Further, due to the use of multiparameter strain series, the gage can now be placed at a considerable distance away from the notch tip to avoid notch tip complications mentioned previously. It is worth noticing here that same strains can be measured using Eq. (4.17) for positive $(+\theta)$ and negative orientation $(-\theta)$ of the gage line.

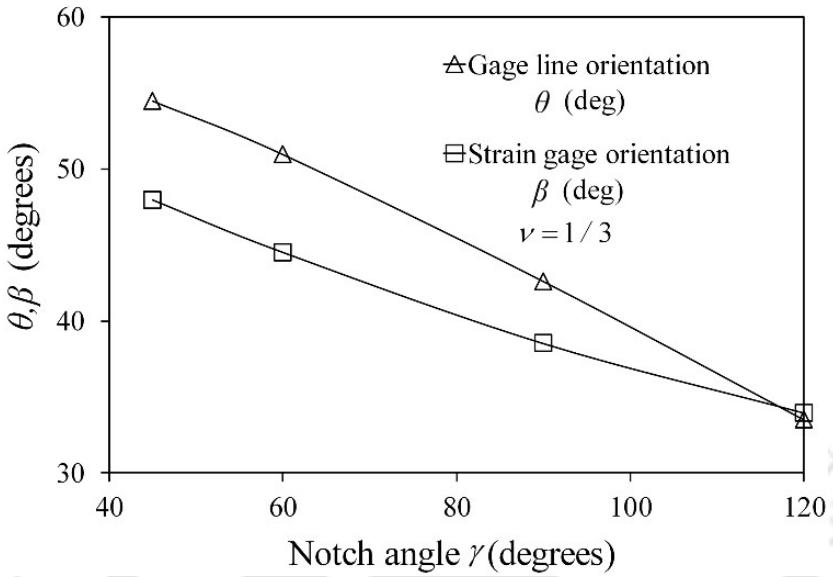

Figure 4.4 Variation of gage line orientation θ and strain gage orientation β with notch angle ($\gamma > 40°$) for Poisson's ratio ν (= 1 / 3).

4.2 Assessment of the valid gage locations

As discussed in the preceding section, the angular position and orientation for the single strain gage (θ and β) are suitably defined by either solving Eq. (4.15) alone ($\gamma \leq 40°$) or by solving Eq. (4.15) and Eq. (4.16) simultaneously ($\gamma > 40°$) depending on the notch angle. It is evident from Eq. (4.17) that prior knowledge of the valid radial location of the strain gage or radial distance r at which the gage needs to be pasted is also extremely important for the accurate determination of NSIF K_I^V. Further, Eq. (4.13) only assures qualitatively that the gages can be placed far away from the notch tip but doesn't provide explicitly the radial locations. This section presents the mathematical background showing the existence and determination of valid gage radial locations of the strain gage.

To ensure accurate measurement of the strain ε_a, strain gages should be located within the region of validity of the selected strain series (Eq. (4.14)) and this constitutes the basis for the determination of valid gage locations. Clearly, the maximum permissible radial distance of a strain gage depends on the extent of validity of the

selected strain series on the radial line where gages are to be pasted i.e., on the gage line defined by angle θ (Fig.4.1(a)). In the present investigation this maximum permissible radial distance is designated as $r_{\max}$.

For a given sharp V-notched configuration (i.e., with a specific value of γ) and material properties ν and G the terms associated with θ, β, κ and λ_1 will remain constant in Eq. (4.17). Therefore, under these conditions, Eq. (4.17) can be re-written as

$$\varepsilon_a = \frac{C}{r^{1-\lambda_1}} \tag{4.19}$$

where C is the constant. Taking logarithms on both sides of Eq. (4.19)

$$\ln \varepsilon_a = (\lambda_1 - 1)\ln r + \ln C \tag{4.20}$$

Along the gage line (Fig.4.1(a)), Eq. (4.20) is valid within a radial distance from the notch tip to say $r \le r_{\max}$. According to the nature of Eq. (4.20), a plot of $\ln(\varepsilon_a)$ versus $\ln(r)$ depicts a straight line of slope equal to $(\lambda_1 - 1)$ with an intercept of $\ln(C)$. As λ_1 ranges from 0.5 to 1, the above slope is always negative. Theoretically, the above straight-line property shall break down beyond $r > r_{\max}$ on the gage line. This is because more than three Williams' coefficients (other than A_1, A_2 and A_2^*) are needed in Eq. (4.14) to represent strain ε_a for $r > r_{\max}$ and as a result, at $r > r_{\max}$ Eq. (4.20) does not display a straight-line property. Thus, the $r_{\max}$ can be viewed as the extent of validity of Eq. (4.17) along the gage line and it is the maximum permissible radial distance for the single strain gage in the proposed technique.

Using the straight-line property exhibited by the Eq. (4.20), the value of $r_{\max}$ can be accurately estimated from the plots of $\ln(\varepsilon_a)$ versus $\ln(r)$. The foregoing discussion indicates that theoretically, the graph of $\ln(\varepsilon_a)$ versus $\ln(r)$ should have an initial straight-line portion of slope equals $(\lambda_1 - 1)$ followed by a non-linear portion as shown schematically in Fig.4.5. Evidently, the $r_{\max}$ is then the radial distance at

which the straight-line portion terminates and the non-linear portion begins as shown in Fig.4.5. This r_{max} can now be employed to assess the valid gage locations. Even though plane stress conditions are employed in the present study, however, it may be noted that an equation similar to Eq. (4.19) can also be developed considering plane strain conditions.

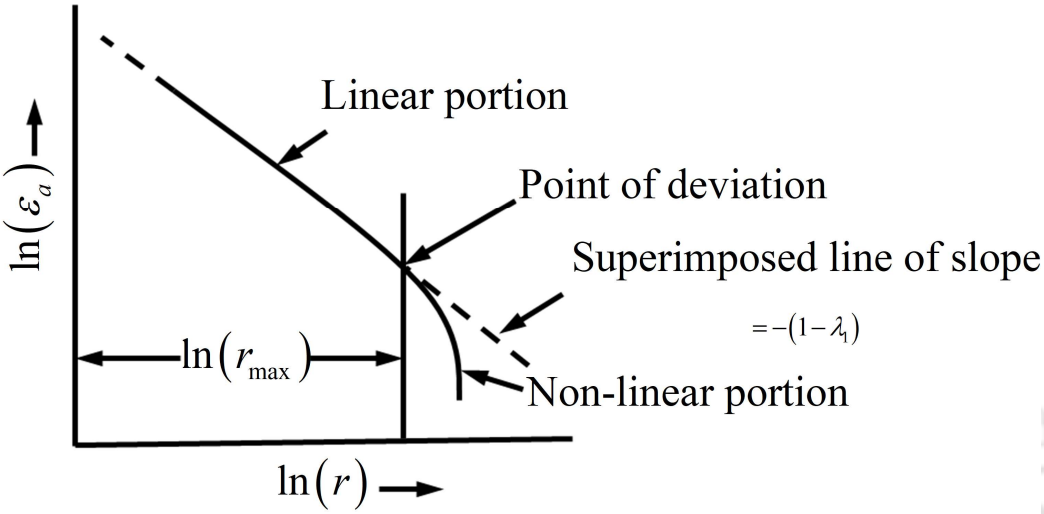

Figure 4.5 Schematic representation of variation of $\ln(\varepsilon_a)$ with $\ln(r)$ along a gage line.

It is well-known that in the vicinity of a crack and a V-notch tip the state of stress is 3D [114-119]. It is evident that strains should not be sampled in those regions as the relationship between the measured strain and NSIF is through the plane stress field equations. Based on the extensive finite element analyses, Li and Guo [119] showed that the extent of the 3D state of stress and a transition from 3D state of stress to 2D state of stress depends only on the thickness and prevails up to a radial distance of 1.25 times the thickness of the notched plate. Thus, the plasticity effects may be kept off by not pasting the gages close to the notch tip, strain gradient errors can be substantially minimized by using gages having small gage lengths [36, 111, 112] and 3D effects can be avoided if the gages are located at locations greater than 1.25 times the thickness of the plate. Clearly, the radial location of the gage should be neither too close to nor too far from the notch tip. Therefore, the valid locations of a strain gage in the proposed approach can now be recommended as

$$r_{\min} \le r \le r_{\max} \tag{4.21}$$

where

$$r_{\min} = 1.25 \times \text{ thickness of the plate [119]} \tag{4.22}$$

Thus, any radial location r along the gage line which satisfies Eq. (4.21) is a valid gage location. Eq. (4.21) assures that the gages can be pasted very close to $r_{\max}$ (but not beyond $r_{\max}$) yet the gage reading can be expected to obey Eq. (4.17). Thus, one can easily decide *a priori* the valid gage locations using Eq. (4.21) once the $r_{\max}$ value of a notched configuration is determined.

In the present investigation, a simple and robust finite element-based approach is suggested for the first time for the accurate determination of $r_{\max}$ value of a given sharp V-notched configuration. The strain ε_a at a large number of finite element nodes (or points) along the entire gage line (i.e., from notch tip to the boundary) is computed using finite element analysis (FEA) of the given sharp V-notched configuration. If the proposed theoretical arguments presented in this section are valid, then a graph between computed values of $\ln(\varepsilon_a)$ versus $\ln(r)$ would show a distinct linear portion and a non-linear portion as shown in Fig. 4.5. Because of the logarithmic plot, a reliable procedure is needed for accurate identification of end point of the straight-line portion. For this purpose, the following procedure is devised for the sharp V-notched bodies

(a) Firstly, a line of slope $(\lambda_1 - 1)$ is superimposed on to the plots of $\ln(\varepsilon_a)$ versus $\ln(r)$ obtained from FEA (see Fig.4.5).

(b) This line is considered as the exact solution and the percent relative error (absolute values) in computed values of $\ln \varepsilon_a$ (obtained from FEA) is then determined at all values of radius (i.e., nodal points) in the plot. The error can be expected to be very large in the non-linear portion and gradually diminishes as one approaches the point till the log-log plot is congruent to the straight line in Eq. (4.20).

(c) Finally, the $r_{\max}$ or the point of deviation on the log-log plot from the superimposed line is one at which the absolute percentage relative error reaches

a value ≤ 0.5% (as one observes from right to left in the graph) as shown in Fig.4.5. The threshold value 0.5% has been chosen based on the extensive numerical experiments.

In this way, r_{max} of a given configuration can be found and this value, in turn, can be employed to assess the valid gage locations *a priori* using Eq. (4.21). For convenience, the whole experimental program using the proposed strain gage-based approach is summarized in a flow chart as shown in Fig. 4.6. On the other hand, r_{min} value is independent of geometry of a V-notched configuration but depends only on the thickness of the specimen. Li and Guo [119] found this value based on extensive finite element analyses. No experimental substantiation of the suggested r_{min} value is available till date. Taking into consideration of this gap, the results of the experimental validation of suggested r_{min} value is presented in Chapter 7 of the present investigation. Once the existence of r_{max} and r_{min} are confirmed, the valid gage locations can be obtained with certainty from Eq. (4.21).

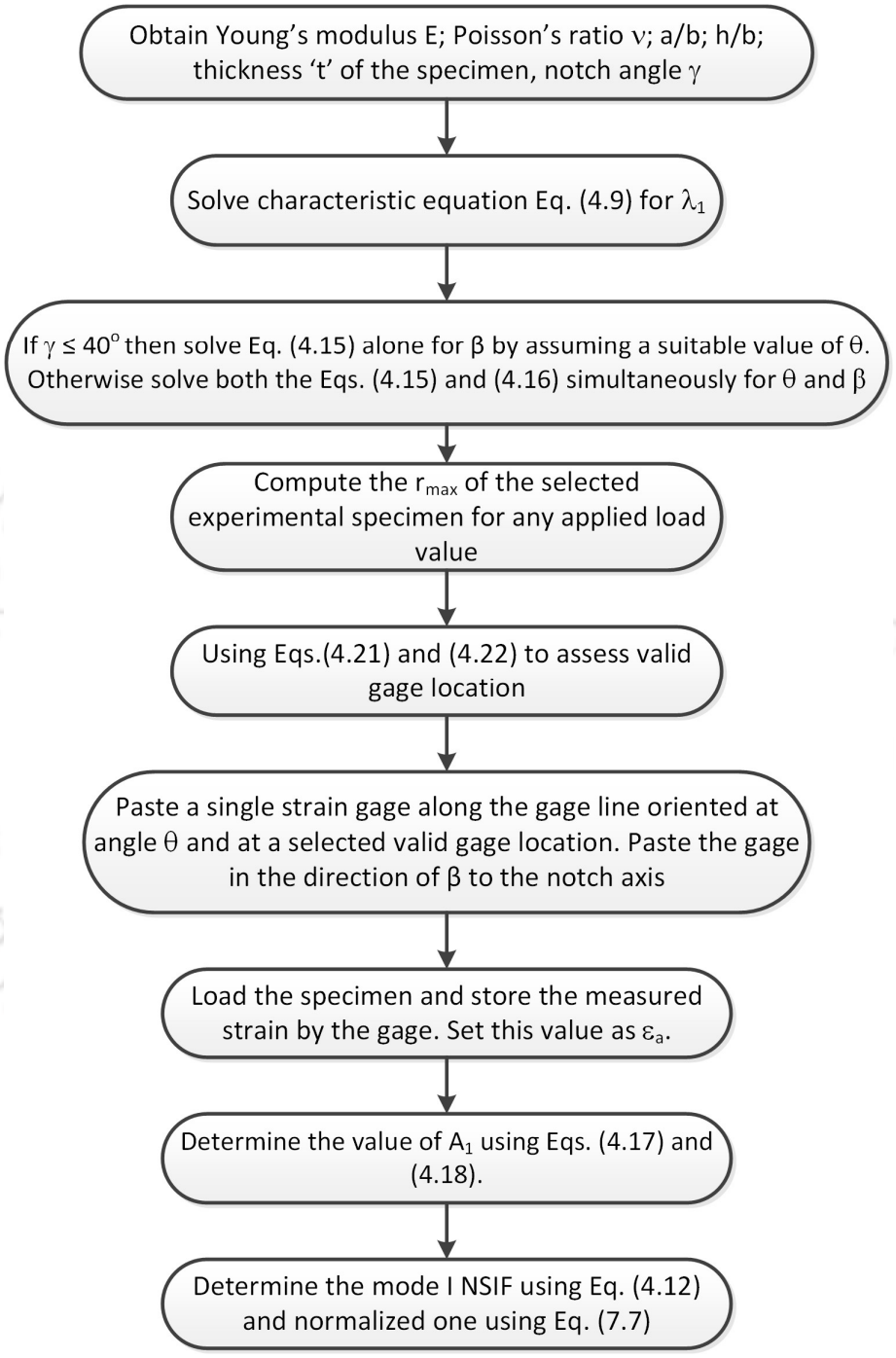

Figure 4.6 Flowchart showing the proposed single strain gage technique with valid gage locations.

4.3 Summary

In this chapter, the proposed single strain gage technique has been discussed thoroughly along with its mathematical formulation. The behaviour of eigenvalues λ_n' and Williams' coefficients A_n' have been explained in detail in this chapter. It has been discussed that the nature of the Williams' coefficients A_n', whether real or complex, is dependent on the nature of the corresponding eigenvalues λ_n'. The nature of λ_n', on the other hand, depends on the magnitude of the notch opening angles γ. It has been shown that the proposed single strain gage technique primarily involves an efficient manipulation of the multiparameter strain formulation to simplify the measurement of the notch stress intensity factor K_I^V. The orientation angle of the gage line θ and the orientation angle of strain gage β are selected in such a way that the multiparameter strain formulation (Eq. (4.14)) gets truncated to only a single term (the first term associated with A_1'). Two distinct cases have been found possible while selecting the values of θ and β viz., $\gamma \le 40°$ and $\gamma > 40°$. Besides, the mathematical strategy to obtain the valid gage locations bounded by $r_{\min}$ and $r_{\max}$, has also been discussed. A flowchart showing the proposed single strain gage technique with valid gage locations has been included at the end of the chapter.

Chapter 5

Determination of r_{max} of various V-notched configurations

This chapter is focused on the estimation of r_{max} value of several mode I benchmark configurations. Finite element analyses (FEA) in all these examples are carried out using ANSYS® software. Eight-nodded isoparametric quadrilateral elements (Q8) are used throughout (Section 3.2). To model the singularity at the notch tip, Q8 elements are collapsed into triangles (six-nodded triangular elements). These six-nodded collapsed Q8 elements are arranged in a typical spider web pattern around the notch tip. Effect of various parameters such as notch length to plate width ratio, notch angle and Poisson's ratio on the estimated values of r_{max} has been investigated in this chapter. The magnitude of r_{max}, as explained earlier in Chapter 4, is the deciding factor of the valid strain gage locations for experimental determination of mode I notch SIF (NSIF) K_I^V using the proposed technique. The procedure described in Section 4.2 is followed here for the estimation of r_{max} using FEA. Different types of sharp V-notched configurations such as single edge notched tensile (SENT) plate, center notched tensile (CNT) plate and double edge notched tensile (DENT) plate have been considered in this chapter. Numerical simulation of the proposed strain gage technique with the valid gage locations have also been carried out in this chapter.

5.1 General procedure for estimation of r_{max}

This section demonstrates the basic procedure for determining r_{max} for any 2D sharp V-notched configuration using the finite element method. For this purpose, a SENT configuration as shown in Fig. 5.1 (a) having a notch angle of $30°$ and $a/b = 0.2$ has been considered. In order to assess the influence of mesh refinement over convergence of the r_{max} values, four different finite element meshes have been considered and are

shown in Fig. 5.2 along with number of nodes (NN), number of elements (NE) and minimum element size in each mesh. Only one of the SENT has been modelled considering into the account of symmetry of the problem and corresponding finite element boundary conditions are shown in Fig. 5.1(b). All parameters of this example have been presented in Table 5.1. The gage line orientation θ is assumed arbitrarily and the corresponding β is obtained from Eq. (4.15). These values are also provided in Table 5.1.

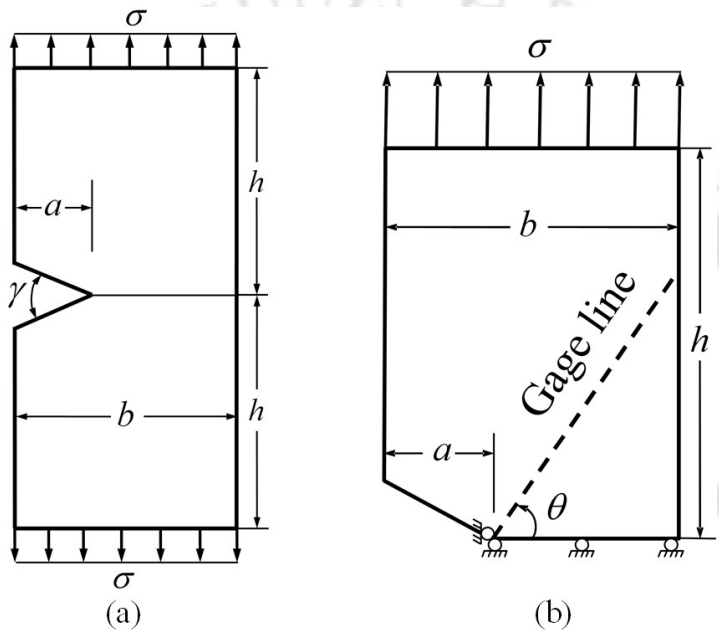

Figure 5.1 (a) SENT specimen under uniform uniaxial tensile load; (b) finite element analysis domain (half symmetry) and boundary conditions.

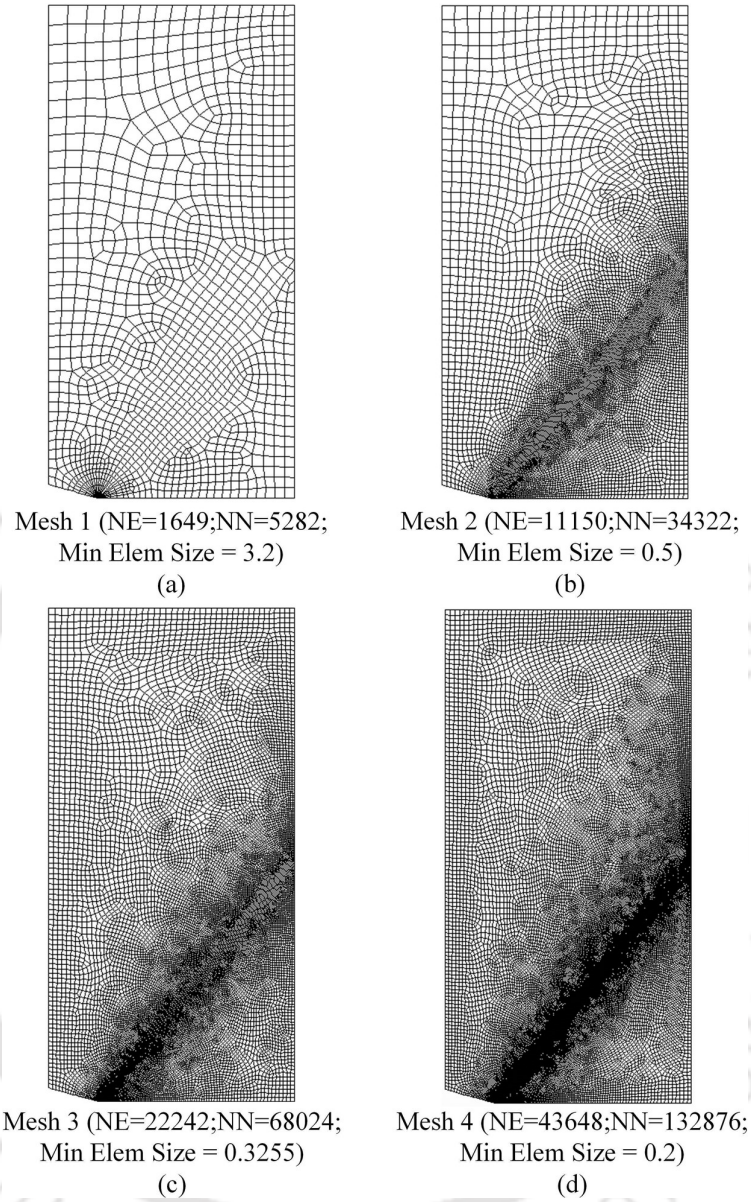

Figure 5.2 Different finite element meshes used for the convergence study along with minimum element size (Min. Elem. Size) of a mesh for SENT plate with notch angle $\gamma = 30°$ and $a / b = 0.2$.

Table 5.1 Geometric, loading and material parameters of the SENT

Notch angle (γ)	First eigen value (λ_1')	b (mm)	a / b	h / b	E (GPa)	ν	σ (MPa)	θ	β
30°	0.5015	150	0.2	2	2.917	0.382	100	50.49°	50.73°

The finite element meshes shown in Fig.5.2 are designed in such a fashion that the nodes of several elements lie along the gage line (Fig.5.1(b)) which makes an angle of θ (Table 5.1) with the notch axis. As depicted in Fig.5.1(b), the gage line originates from the tip of the sharp V-notch and extends to the outer boundaries of the notched plate. According to the present proposed strain gage technique, a single gage is needed to be placed at an appropriate radial location r on this line in the direction of β in order to measure the linear strain ε_a (Fig.4.1). As explained in section 4.1, since the $\gamma < 40°$, the value of θ is arbitrarily set to $50.49°$ and corresponding to this $\beta = 50.73°$ is obtained using Eq. (4.15). Following the procedure described in section 4.1, the computed strains in the global coordinates are transformed to the strain ε_a in the direction defined by β (Fig.4.1(a)). The radial distance (r) of each of the nodes placed on the gage line from the notch tip are then computed.

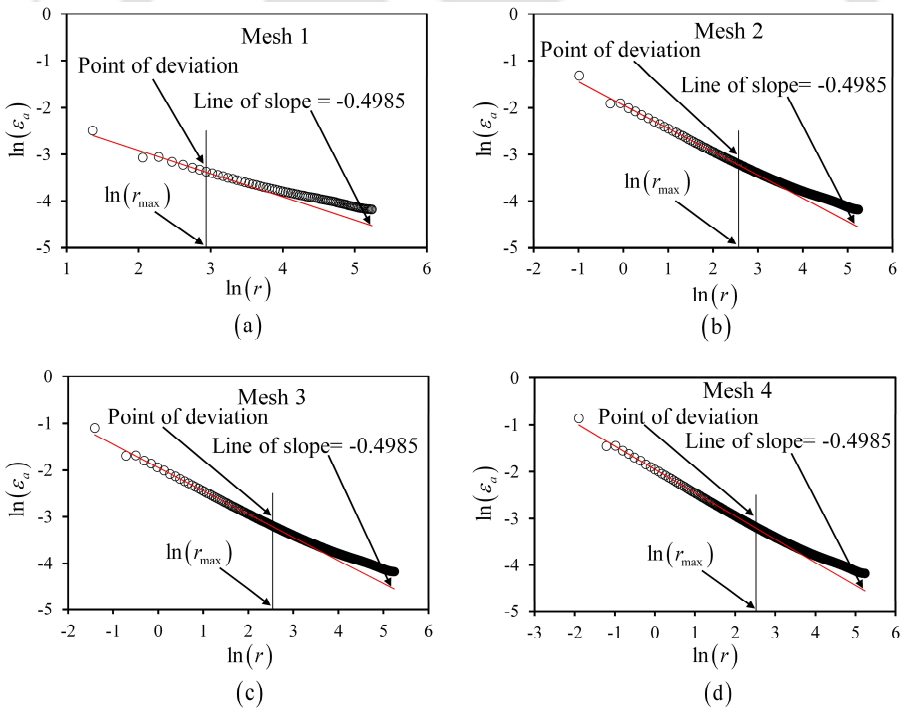

Figure 5.3 Variation of $\ln(\varepsilon_a)$ with $\ln(r)$ along the gage line for sequence of finite element meshes considered for convergence study with $\gamma = 30°$ and $a / b = 0.2$.

Conforming to the Eq. (4.20), plots of $\ln(\varepsilon_a)$ versus $\ln(r)$ along the gage line for each of the four meshes have been made as shown in Fig.5.3. The data corresponding to the notch tip is not shown in the Fig.5.3 as the radial distance of this point from the notch tip is zero. It is important to observe from all the plots of Fig.5.3 that each plot consists of a distinguishable linear portion followed by a non-linear portion (in logarithmic scale) as predicted by the theory presented in section 4.2. Further, as the meshes are refined, the extent of the straight-line portion of the plots is observed to have gradually increased which can be seen more prominently in fine meshes than in the coarse mesh. The initial linear part is due to the dominance of the parameters A_1, A_2 and A_2^* (A_2^* being zero for $\gamma < 40°$) in Eq. (4.14) for the notch angle $\gamma = 30°$ and the non-linear portion can be attributed to the dominance of more number of Williams coefficients other than A_1, A_2 and A_2^*. In case of the notch angle $\gamma > 40°$, the linear portion is due to the dominance of the three coefficients A_1, A_2 and A_2^* ($A_2^* \neq 0$ for $\gamma > 40°$) and the non-linear part is due to the presence of more number of coefficients apart from A_1, A_2 and A_2^*. The terminal point of the linear portion or the beginning point of the non-linear part of the plots in Fig.5.3 is clearly the maximum permissible radial distance $r_{\max}$ for the strain gage according to the proposed technique (Chapter 4). This is true for any value of the notch angle γ. Clearly, the $r_{\max}$ also defines the extent of dominance of the parameters A_1, A_2 and A_2^* for a given γ.

Following the methodology described in section 4.2, first a line having a slope of $(\lambda_1 - 1)$ is superposed onto the plots of $\ln(\varepsilon_a)$ versus $\ln(r)$. In the present example, the slope equals to $0.5015 - 1 = -0.4985$. This line is regarded as the exact solution and the absolute percentage relative error in $\ln(\varepsilon_a)$ at all points of plot in Fig.5.3 is then determined. The $r_{\max}$ or the point of deviation of the plot of $\ln(\varepsilon_a)$ versus $\ln(r)$ from the superposed line is considered as the radius at which the error reaches ≤ 0.5% (as one observes from right to left).

Following the above procedure, Fig.5.3 also shows the superposed line of slope equal to -0.4985 in all the plots. It is worth noting that, both the initial straight-line portion of the plots and superposed lines are congruent to each other up to a certain radial distance. Figure 5.4 shows the percentage relative error between the finite

element solution of $\ln(\varepsilon_a)$ (encircled data points in Fig.5.3) obtained from the Mesh 4 (Fig.5.2) and exact solution (represented by solid line) at different radii on the gage line. It can be seen from Fig.5.4 that the error decreases monotonically from the non-linear to linear portion to the left. The value of the radius at which the percentage relative error reaches less than or equal to 0.5% is marked in all the plots of the Fig.5.3, indicating the $r_{\max}$ of the SENT configuration with $a/b = 0.2$. The corresponding numerical values of the $r_{\max}$ are presented in Table 5.2 with the mesh refinement. It can be noticed from Table 5.2 that as the meshes are refined $r_{\max}$ value converges. No significant improvement is noticed with further refinement of the mesh beyond Mesh 4 in Fig.5.2. Thus, the $r_{\max}$ value of the selected SENT configuration can be taken as 12.45 mm and the valid gage location can be assessed using Eq. (4.21) if the thickness of the plate is available. Similar trends have been noticed in $\ln(\varepsilon_a)$ versus $\ln(r)$ plots corresponding to the SENT configuration with different notch angles γ and some of them have been presented in the next example.

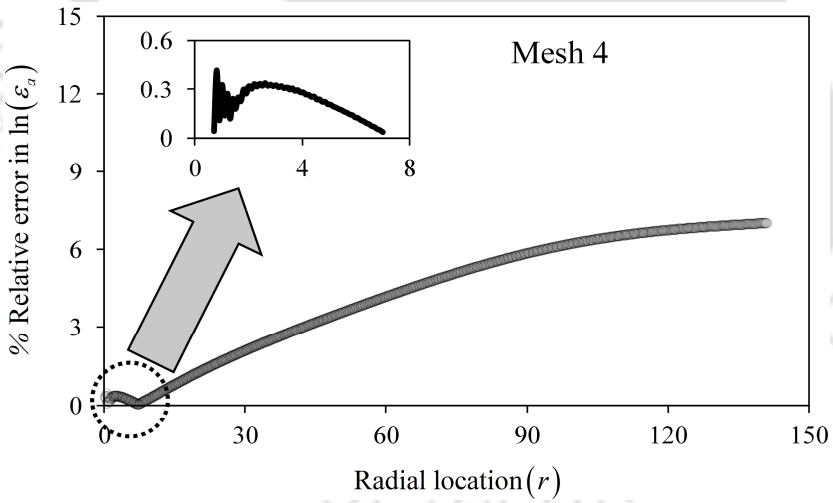

Figure 5.4 Percentage relative error between the finite element solution of $\ln(\varepsilon_a)$ at different radii along the gage line for SENT plate with $\gamma = 30°$ and $a/b = 0.2$.

Table 5.2 Convergence of the r_{max} with mesh refinement for SENT plate with $\gamma = 30°$ and $a / b = 0.2$

Mesh	r_{max} (mm)
Mesh 1	18.86
Mesh 2	13.10
Mesh 3	12.70
Mesh 4	12.45

5.2 Effect of a / b ratio on r_{max}

As r_{max} is a function of singular (A_1) and non-singular coefficients (A_2, A_2^*), therefore the present section studies the effect of geometry on the r_{max} as these coefficients are functions of geometry and boundary conditions. In order to study this issue, the SENT configurations with $a / b =$ 0.2 to 0.8 with an increment of 0.2 has been considered in this section. For each of these a / b values, the notch angle is also varied from $0°$ to $90°$ with an increment of $15°$. Other geometric, loading and material properties are same as in section 5.1 (Table 5.1). The values of θ and β have been obtained as explained in section 4.1. The values of θ and β for notch angles from $0°$ to $90°$ are tabulated in Table 5.3.

Table 5.3 Gage line orientation θ and strain gage orientation β for different geometries of SENT plate

Notch angle γ	a / b	Gage line orientation θ	Strain gage orientation β
0°	0.2	53.13°	58.28°
	0.4	53.13°	58.28°
	0.6	53.13°	58.28°
	0.8	53.13°	58.28°
15°	0.2	52.38°	54.34°
	0.4	52.38°	54.34°
	0.6	52.38°	54.34°
	0.8	52.38°	54.34°
30°	0.2	50.49°	50.73°
	0.4	50.49°	50.73°
	0.6	50.49°	50.73°
	0.8	50.49°	50.73°
45°	0.2	47.81°	47.39°
	0.4	47.81°	47.39°
	0.6	47.81°	47.39°
	0.8	47.81°	47.39°
60°	0.2	44.56°	44.32°
	0.4	44.56°	44.32°
	0.6	44.56°	44.32°
	0.8	44.56°	44.32°
75°	0.2	40.93°	41.54°
	0.4	40.93°	41.54°
	0.6	40.93°	41.54°
	0.8	40.93°	41.54°
90°	0.2	37.06°	39.06°
	0.4	37.06°	39.06°
	0.6	37.06°	39.06°
	0.8	37.06°	39.06°

Refined finite element meshes have been considered for carrying out this study for all a / b ratios. Following the procedure explained in section 5.1, plots of $\ln(\varepsilon_a)$ versus $\ln(r)$ are obtained corresponding to $a / b =$ 0.2 to 0.8 with an increment of 0.2. For

instance, Figure 5.5 shows $\ln(\varepsilon_a)$ versus $\ln(r)$ for various values of a/b corresponding to the notch angle $\gamma = 60°$ ($\theta = 44.56°$ and $\beta = 44.32°$). Figure 5.5 also shows marks on each graph which correspond to the values of the r_{max} computed following the procedure described in the previous section. Once again, the trends (linear and non-linear portions in the graphs) predicted by the proposed theory in section 4.2 can also be seen in Fig.5.5 for all a/b ratios considered here. Although not shown here, similar trends have also been observed for other values of γ (between $0°$ and $90°$) as well.

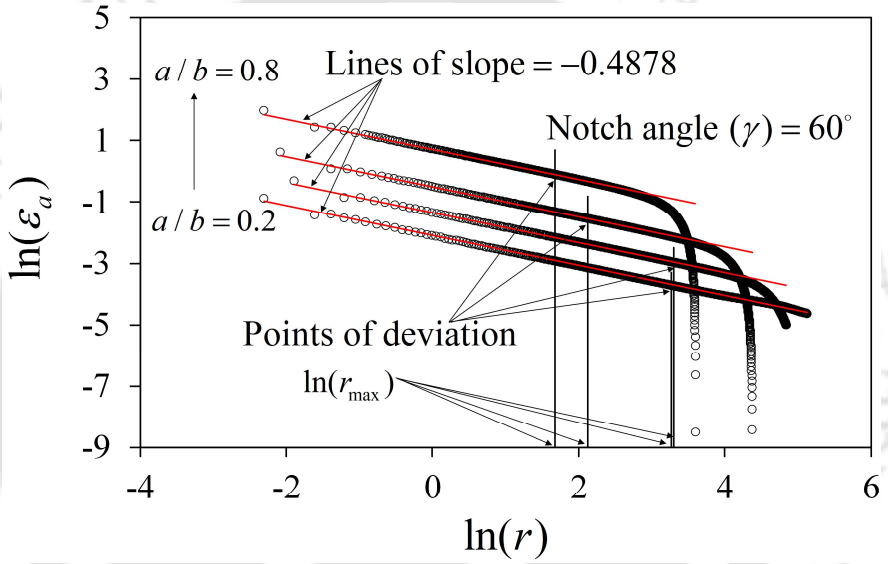

Figure 5.5 Variations of $\ln(\varepsilon_a)$ with $\ln(r)$ along the gage line for different a/b ratios for the SENT configuration with the notch angle $\gamma = 60°$.

Figure 5.6 shows the variation of r_{max}/b with a/b ratio for different notch angles. It can be observed from Fig.5.6 that for a given a/b ratio, the value of r_{max} increases with increasing notch angle. In addition, for a given notch angle i.e., for a given V-notched configuration, r_{max} increases with the increase in a/b initially and beyond a certain value of a/b it decreases with the increase in a/b. This dependence of r_{max} on a/b is true for all notch angles. It can also be noticed that maximum value of r_{max} occurs between $a/b = 0.35$ and 0.45. The striking feature of the results presented in Fig.5.6 is that the trend of dependence of r_{max} with a/b in the present study for the

V-notch problems is similar to that reported for crack problems by Sarangi et al [101]. A deeper explanation for such inverted bell-shaped tendency of $r_{\max}$ with a/b and numerical substantiation to this phenomenon is discussed in detail for crack problems by Sarangi et al in Ref. [101] and is also applicable for the present V-notch problems. Accordingly, the extent of $r_{\max}$ increases with the increase in crack length as long as the boundary effect is insignificant which usually the case at relatively small values of the crack length. On the other hand, for relatively larger values of the crack length the $r_{\max}$ decreases with the increase in crack length due to the domination of the boundary effects. Table 5.4 shows the numerical values of $r_{\max}$ obtained for different a/b (between 0.2 and 0.8) and for different notch angles γ (between $0°$ and $90°$).

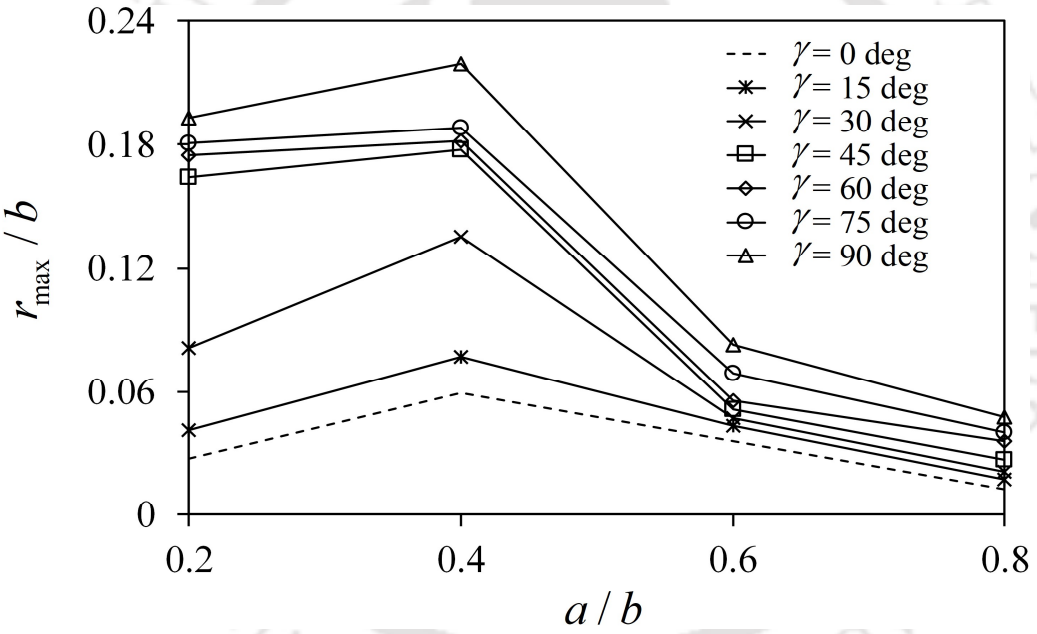

Figure 5.6 Variation of $r_{\max}/b$ with a/b for the SENT configurations for different notch angles.

Table 5.4 Values of r_{max} for different a/b ratios from 0.2 to 0.8 and for notch angles from 0° to 90°

Notch angle (γ)	a/b	r_{max} (mm)	r_{max}/b
0°	0.2	4.13	0.0275
	0.4	8.93	0.0595
	0.6	5.41	0.0360
	0.8	1.88	0.0125
15°	0.2	6.18	0.0412
	0.4	11.57	0.0771
	0.6	6.48	0.0432
	0.8	2.56	0.0170
30°	0.2	12.45	0.0830
	0.4	20.30	0.1353
	0.6	7.07	0.0471
	0.8	3.14	0.0209
45°	0.2	24.67	0.1645
	0.4	26.65	0.1777
	0.6	7.71	0.0514
	0.8	4.04	0.0269
60°	0.2	26.23	0.1749
	0.4	27.26	0.1818
	0.6	8.35	0.0557
	0.8	5.37	0.0358
75°	0.2	27.10	0.1807
	0.4	28.21	0.1880
	0.6	10.33	0.0688
	0.8	6.00	0.0400
90°	0.2	28.99	0.1932
	0.4	32.89	0.2193
	0.6	12.48	0.0832
	0.8	7.13	0.0475

5.3 Numerical simulation of performance of the proposed single strain gage technique with valid gage locations

This section examines the performance of the proposed single strain gage technique using simulated strains obtained through finite element analysis. For this purpose, a benchmark problem of sharp V-notched SENT specimen presented by Ayatollahi and Nejati [65] is considered here. Referring to Fig.5.1(a), the geometrical and loading parameters for this specimen are $b=1$, $a/b=0.4$, $h=1$, $\sigma=1$, $\gamma=30°$ and thickness $t=0.02$. Using an overdeterministic method, Ayatollahi and Nejati [65] estimated the value of the singular coefficient $A_1=0.9334$ and hence the reference value $K_{I-Ref}^{V}=2.4110$. This value of mode I NSIF is used as a reference or exact solution in subsequent calculations. The material properties are assumed as Young's modulus $E=2917$ and Poisson's ratio $\nu=0.382$. Units of this problem are consistent and plane stress condition is assumed. As the material properties are same as in the section 5.1, the strain gage orientation β and the gage line orientation θ for this example are $50.73°$ and $50.49°$ respectively. A mesh similar to that in Fig.5.2(d) is employed and symmetry is also exploited for this problem for the purpose of finite element analysis. Following the procedure explained in section 5.1, a plot of $\ln(\varepsilon_a)$ versus $\ln(r)$ is obtained as shown in Fig.5.7(a) and the $r_{\max}$ value for this configuration is found to be 0.4603 leading to $r_{\max}/b=0.4603$. Figure 5.7(b) shows the % relative error in $\ln(\varepsilon_a)$ with the radial distance r. Once again, it is observed from Fig.5.7(b) that the error is diminishing as one approaches from non-linear zone to linear zone. Therefore, in accordance with Eq. (4.21) of the proposed approach the valid gage location (r) can now be assessed as

$$r_{\min}(=1.25t=0.025)\le r\le r_{\max}(=0.4603) \tag{5.1}$$

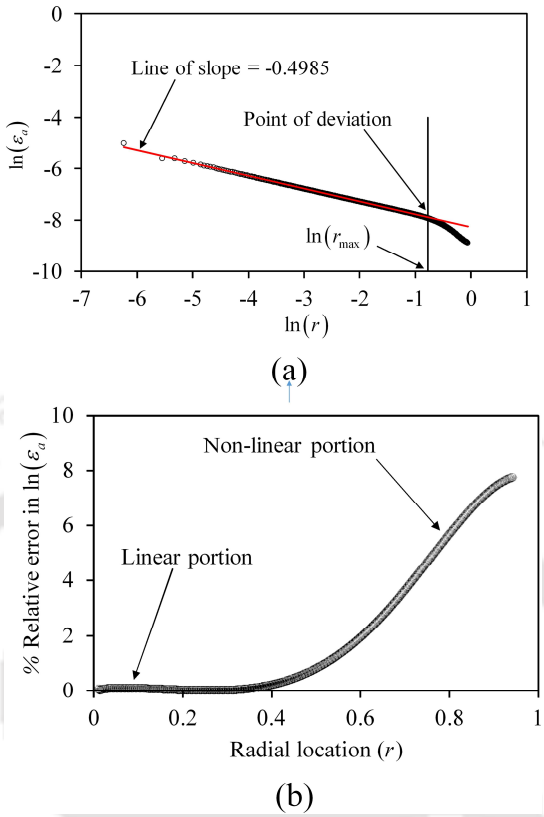

Figure 5.7 (a) Variation of $\ln(\varepsilon_a)$ with $\ln(r)$ along the gage line for a SENT configuration with a notch angle $\gamma = 30°$; (b) variation of percentage relative error in $\ln(\varepsilon_a)$ with radial location r along the strain gage line.

According to the proposed theory, any radial location that satisfies Eq. (5.1) is a valid gage location and the mode I NSIF obtained using the measured strains at these locations are expected to provide very accurate strains and hence very accurate stress intensity factors. Further, gages located beyond r_{max} i.e., invalid gage locations are predicted to result in highly erroneous NSIFs. It is worth mentioning here that the proposed strain gage technique requires only one strain gage for measurement of K_I^V. In order to understand the efficacy of the proposed single strain gage technique and usefulness of the proposed valid gage locations, three sample radial locations for locating the single strain gage have been selected within and outside the r_{max} (as shown in Table 5.5) to simulate the strain measurements at the valid and invalid gage locations respectively.

Table 5.5 Error in simulated measurements of mode I NSIF, K_I^V at valid and invalid locations

Radial location, r	$r / r_{\max}$	Estimated K_I^V	% Relative Error $\left(K_{I-Ref}^V = 2.4110\right)$
0.2 (Valid)	0.4345	2.4245	0.55
0.3 (Valid)	0.6517	2.4266	0.64
0.4 (Valid)	0.8700	2.3886	0.93
0.6 (Invalid)	1.3035	2.0778	13.83
0.8 (Invalid)	1.7380	1.5246	36.77
0.9 (Invalid)	1.9552	1.3261	45.00

Considering that strain at each node along the gage line represents a strain gage reading, nodal strains ε_a at the selected valid and invalid gage locations are obtained from the FEA. Using those strains, A_1 is computed corresponding to each radial location using Eq. (4.17) and subsequently the value of K_I^V is computed at each radial location by putting the computed value of A_1 in Eq. (4.12). Table 5.5 also shows comparison of these estimated NSIFs K_I^V with the reference solution $K_{I-Ref}^V = 2.4110$ reported by Ayatollahi and Nejati [65] and the percentage relative error between them considering the reference solution as an exact solution. Simulated results in Table 5.5 clearly show that the percentage relative error in measured K_I^V is less than 1% when the strain gage is placed within the range of valid radial location. At all the valid locations the measured K_I^V is nearly same as expected. On the other hand, percentage relative error in estimated K_I^V is greater than 10% even if the strain gage is placed just outside the valid location. In fact, the percentage relative error in estimated K_I^V is as high as 45% when the strain gage is placed at an invalid location further away from $r_{\max}$. Two important inferences could be drawn from these simulated results. First, based on the proposed theory it is possible to accurately determine the K_I^V using a single strain gage. Second, there exist

valid radial locations corresponding to a particular specimen configuration and the strain gage should be placed in the valid location to ensure accurate determination of K_I^V. Thus, it is extremely important to know the valid radial location of the strain gage *a priori* to ensure that the K_I^V could be accurately determined from the proposed single strain gage experiment. Table 5.5 also shows that the present method of determination of $r_{\max}$ is robust and ensures accurate measurement of K_I^V from single strain gage experiment.

5.4 Effect of the gage line orientation θ on r_{max}

This example illustrates additional advantage in selection of certain easily locatable gage lines available with the configurations $\gamma \leq 40°$. As explained in section 4.1, for these configurations one can choose any arbitrary value of gage line orientation θ. In the previous examples, an arbitrary value of $\theta = 50.49°$ has been selected. However, particular orientations of gage lines are more convenient in locating them and facilitate easy installation of strain gages (Fig.5.8) and thus minimize the errors associated while pasting the gages. For instance, the gage line 1 (i.e., the line joining the notch tip to the boundary in the direction $\theta = 0°$) and the gage line 4 (i.e., the line joining the notch tip to the top corner of the configuration in the direction $\theta = \theta_C$) which has more length than the former gage line. These two gage lines can be easily located on a specimen.

Apart from the above advantages of the gage lines 1 and 4, it is also important to know the value of $r_{\max}$ on these gage lines for convenient pasting of the gages. Thus, it is imperative to study the variation of $r_{\max}$ as θ is varied from 0° to θ_C. Such a study also provides information about the impact of length of the gage line on $r_{\max}$ for a given configuration. The present example studies these aspects and for this purpose the configuration employed in section 5.1 (notch angle of 30°) is considered here. The ratio $a/b =$ 0.2 to 0.8 with an increment of 0.2 has been considered. As shown in Fig.5.8, four gage lines with varying θ are considered. The first gage line has $\theta = 0°$, the second line has $\theta = \theta_C / 2$, the third gage line has an arbitrarily selected value $\theta = 50.49°$ and the fourth gage line connects the notch tip to the top corner of the

configuration i.e. $\theta = \theta_C$. Following the procedure adopted in the previous examples, r_{max} value corresponding to each of the above four gage lines has been determined and listed in Table 5.6. It is clear from the results in Table 5.6 that as θ is varied from 0° to θ_C, the length of the gage line increases and so is the r_{max} value.

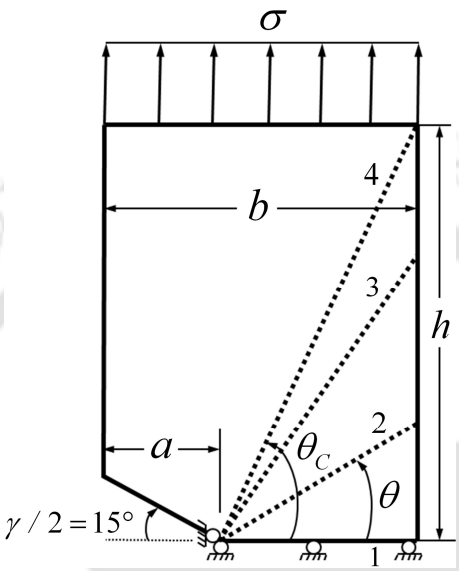

Figure 5.8 Different gage lines that can be selected in case of notch angle $\gamma \leq 40°$.

Thus, for the configurations having $\gamma \leq 40°$, selecting gage lines such as the gage line 4 is preferably a better choice for reducing the errors during pasting of the gage as this line is easier to draw on the specimen and provides maximum r_{max} and hence provides more space for laying the gage. Though, the results in Table 5.6 indicate a direct proportionality between the length of the gage line and the r_{max}, however this is true only for a given a/b configuration. For example, the length of the gage line 4 for the configuration $a/b = 0.2$ is more than the length of the gage line 4 for $a/b = 0.4$, but the value of r_{max} (18.10 mm) in the former case is less than the value of r_{max} (23.93 mm) in the latter case.

Table 5.6 Different choices of combination of θ and β for a specific a/b ratio and the corresponding r_{max} values

a/b	θ_C	θ	Length of the gage line (mm)	β	r_{max} (mm)
0.2	68.20°	0°	120	61.55°	0.80
		34.10°	144.92	53.50°	7.40
		50.49°	188.62	50.73°	12.45
		68.20°	323.13	48.98°	18.10
0.4	73.30°	0°	90	61.55°	1.71
		36.65°	112.18	52.99°	13.10
		50.49°	141.46	50.73°	20.30
		73.30°	313.20	48.68°	23.93
0.6	78.69°	0°	60	61.55°	0.64
		39.35°	77.59	52.49°	5.93
		50.49°	94.30	50.73°	7.07
		78.69°	305.94	48.45°	7.85
0.8	84.29°	0°	30	61.55°	0.48
		42.15°	40.46	51.99°	1.27
		50.49°	47.15	50.73°	3.14
		84.29°	301.53	48.27°	6.43

5.5 Determination of r_{max} for the sharp center V-notched (CNT) plates

Another configuration, a sharp center V-notched (CNT) plate under mode I loading with a plane state of stress is considered here as shown in Fig.5.9. Geometry, material properties and loading parameters are listed in Table 5.7. Exploiting the symmetry of the specimen, only a quarter of the plate has been modelled in the FEA shown as a shaded region in Fig.5.9 along with the boundary conditions. To understand the influence of notch angle on the NSIF, four different notch angles viz., $\gamma = 0°$, $30°$, $45°$ and $60°$ have been considered. In addition, four different a/b ratios viz., 0.2,

0.4, 0.6 and 0.8 have been considered to understand the influence of a/b ratio. In all analyses, a refined mesh (NE=88500, NN=266441) has been used which was obtained after the mesh convergence study.

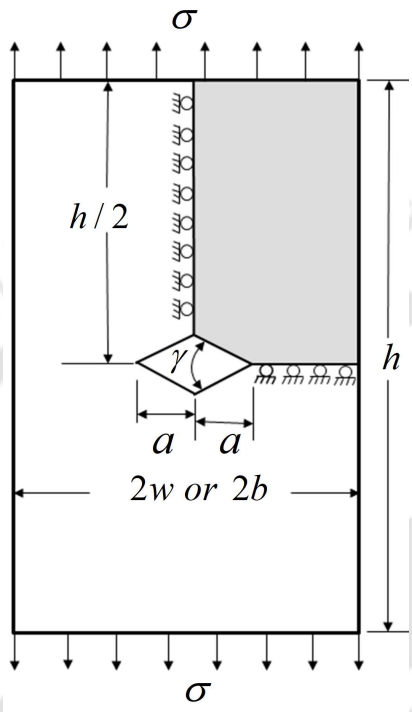

Figure 5.9 Sharp center V-notched configurations under uniaxial tension and the FEA domain (shaded region).

Table 5.7 Geometric, material and loading parameters of sharp center V-notched (CNT) configurations

b (mm)	Notch angle γ	a/b	$h/2b$	ν	E (GPa)	σ (MPa)
75	0°, 30°, 45°, 60°	0.2, 0.4, 0.6, 0.8	2	1/3	200	100

5.5.1 Influence of a/b on r_{max}

Log-log graphs have been plotted showing the variation of $\ln(\varepsilon_a)$ with $\ln(r)$ for different a/b ratios (a/b ranging from $a/b=0.2$ to 0.8 with an increment of 0.2) of a particular notch angle γ. The log-log graphs, which are direct representations of

the determination of r_{max}, have been plotted for different notch angles (notch angle γ = 30°, 45° and 60°) as shown in Figs.5.10-5.12. To understand the influence of a/b ratio on r_{max}, the ratio of r_{max}/b is plotted against a/b for different notch angles as shown in Fig.5.13. Figure 5.13 exhibits the characteristic bell-shaped curve showing that the parameter r_{max}/b increases in the beginning while shifting from $a/b = 0.2$ to $a/b = 0.4$ and subsequently it decreases while shifting from $a/b = 0.4$ to $a/b = 0.8$ which is due to the edge effect observed in the case of cracks by Sarangi et al. [101] and for the SENT configurations (Fig.5.6 of Section 5.2). From Fig.5.13, it can also be observed that the r_{max} value increases with the notch angle γ at a constant a/b ratio but this trend prevails within $a/b = 0.6$.

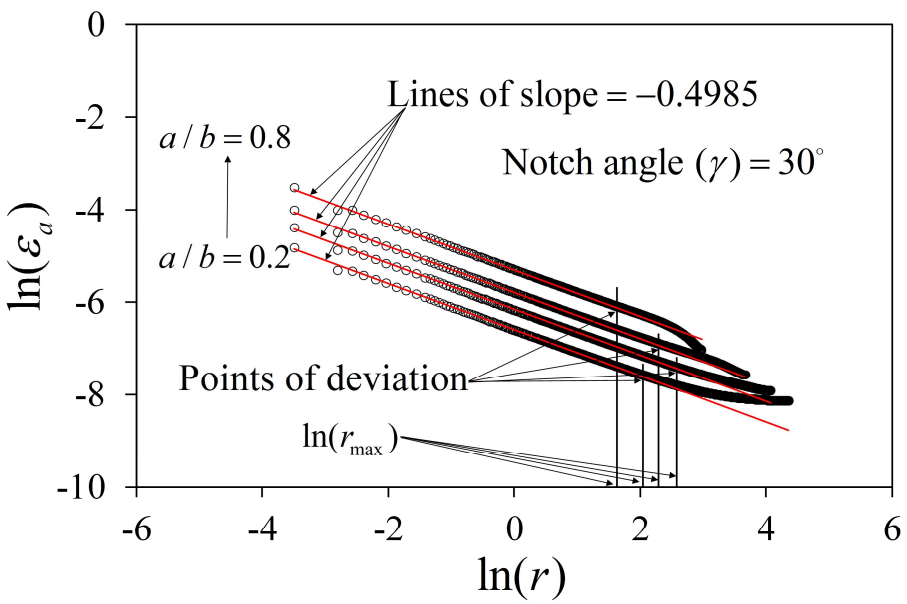

Figure 5.10 Variation of $\ln(\varepsilon_a)$ with $\ln(r)$ along the gage line for sharp center V-notched (CNT) plate with notch angle γ = 30° with a/b varying from 0.2 to 0.8.

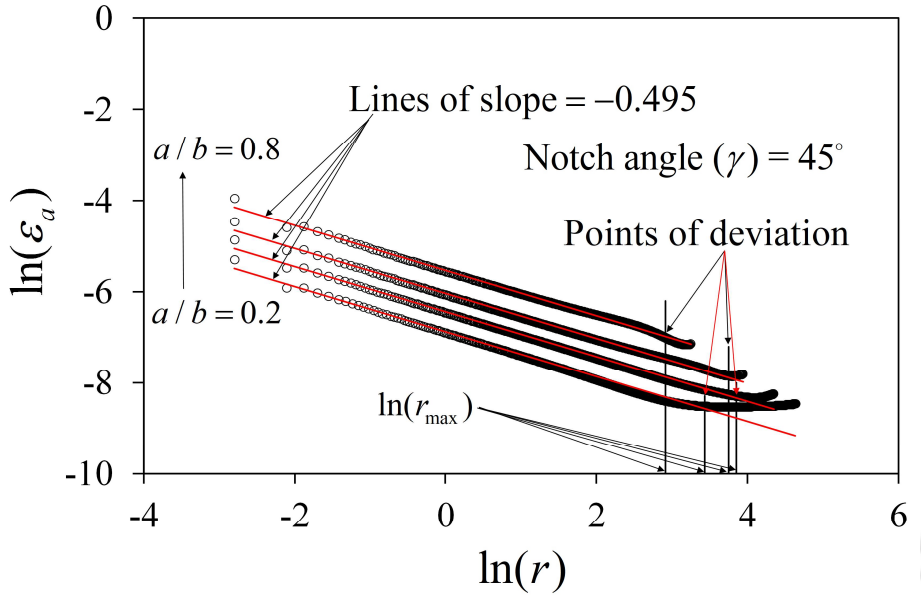

Figure 5.11 Variation of $\ln(\varepsilon_a)$ with $\ln(r)$ along the gage line for sharp center V-notched (CNT) plate with notch angle $\gamma = 45°$ with a/b varying from 0.2 to 0.8.

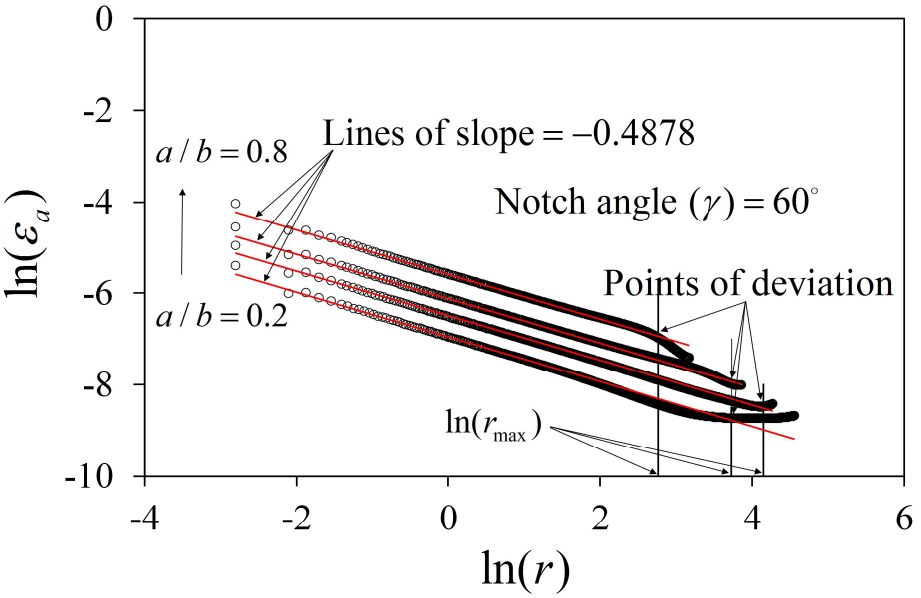

Figure 5.12 Variation of $\ln(\varepsilon_a)$ with $\ln(r)$ along the gage line for a sharp center V-notched (CNT) plate with notch angle $\gamma = 60°$ with a/b varying from 0.2 to 0.8.

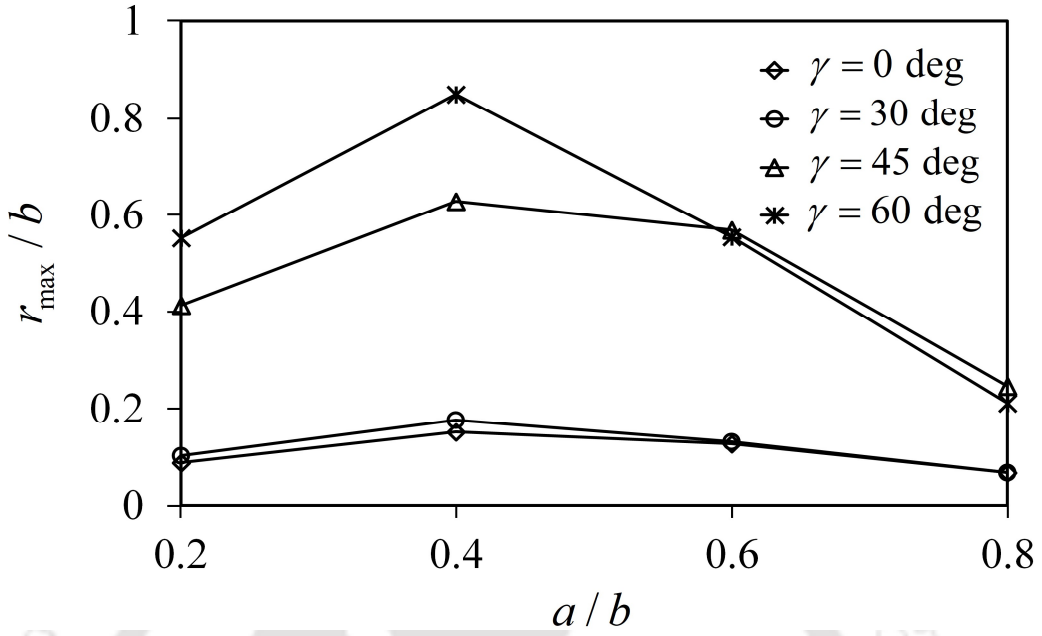

Figure 5.13 r_{max} / b variation with a / b for sharp center V-notched tensile (CNT) configuration for different notch angles γ under mode I loading condition.

5.5.2 Numerical simulation of measurement of the NSIFs for CNT configurations

This section again further examines the efficacy of the proposed single strain gage technique using simulated strains obtained through finite element analysis of the CNT configuration. For this purpose, a benchmark problem of CNT specimen presented by Treifi et al. [123] is considered here. Referring to Figure 5.9, the geometrical and loading parameters for this specimen are presented in Table 5.8. Plane stress conditions have been assumed. Using fractal finite element method, Treifi et al. [123] found the normalized mode I NSIF of 1.053 for this configuration. This value of mode I NSIF is used as a reference or exact solution in subsequent calculations. Following the procedure as explained in section 4.2, the value of r_{max} for this configuration is found equal to 7.70 mm. Strain measurements are taken at selected valid and invalid radial gage locations using FEA simulations, and NSIFs are calculated based on those FE simulated strain values and are listed in Table 5.9. Table 5.9 clearly shows that the

notch SIF values show excellent agreement with the reference solution at radial locations $r < r_{max}$, the percentage relative error increases at radial locations $r > r_{max}$, and the error is as high as 30% at r which is far beyond the r_{max}.

Table 5.8 Geometric, material and loading parameters of the sharp center V-notched (CNT) configuration

b (mm)	Notch angle γ	a / b	$h / 2b$	ν	E (GPa)	σ (MPa)
75	30°	0.2	2	1/3	200	100

Table 5.9 Error in mode I normalized NSIF, K_I^V at different strain gage locations for the CNT with $\gamma = 30°$, $a / b = 0.2$ (r_{max} = 7.7 mm, r_{min} = 1.25 mm)

Radial location r (mm)	Estimated Normalized K_I^V	% Relative Error $\left(\text{Normalized } K_{I-\text{Ref}}^V = 1.053 \text{ [123]}\right)$
3.0 (valid)	1.080	2.6
4.0 (valid)	1.087	3.2
5.0 (valid)	1.093	3.8
6.0 (valid)	1.101	4.6
7.0 (valid)	1.108	5.2
8.0 (Invalid)	1.115	5.9
9.0 (Invalid)	1.124	6.7
11.0 (Invalid)	1.140	8.3
15.0 (Invalid)	1.179	12.0
20.0 (Invalid)	1.238	17.6
25.0 (Invalid)	1.303	23.7
30.0 (Invalid)	1.374	30.5

5.6 Determination of r_{max} for the double edge notched tensile (DENT) configurations

A double edge notched tensile plate as shown in Fig.5.14(a) with $a / b = 0.2$ to 0.8 in increments of 0.2, $b = 75$ mm and $h / b = 4$ is considered. Applied stress $\sigma = 100$ MPa and material properties with the Young's modulus $E = 200$ GPa and Poisson's ratio $\nu = 1/3$ are considered for the analysis. Plane stress conditions are assumed throughout the analysis. Only one-quarter portion of the full domain is utilized for finite element analysis due to the symmetry as shown in Fig.5.14(b).

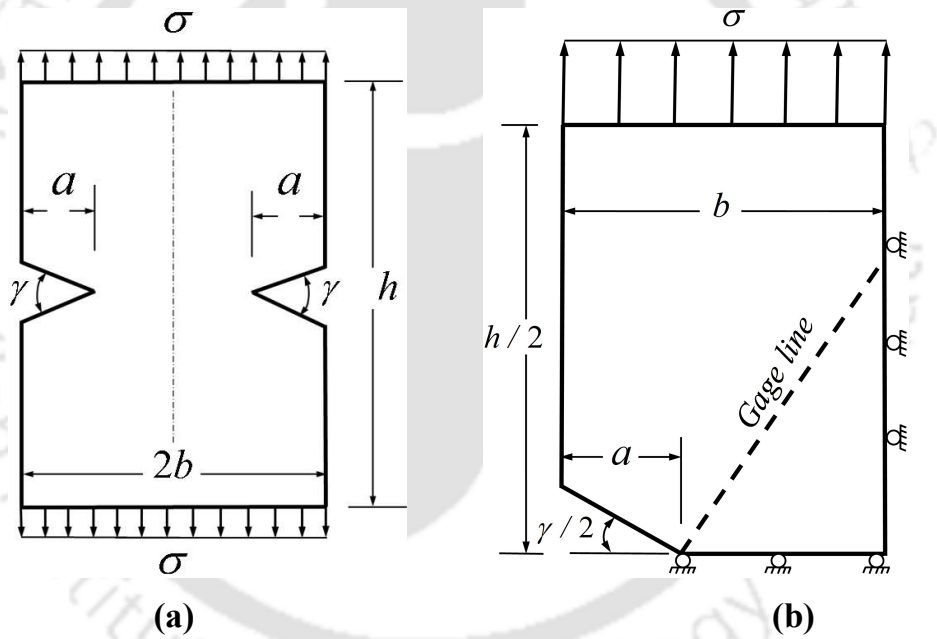

Figure 5.14 (a) Double edge notched plate; (b) Exaggerated view of the FE solution domain (one-quarter portion) for the double edge notched plate.

Figure 5.15(a) shows a typical finite element mesh in the finite element analysis for all a / b ratios and Fig.5.15(b) shows an exaggerated view of the notch tip. Following the procedure described in the section 4.1, ε_a values of double edge notched plate $a / b = 0.2$ to 0.8 have been evaluated. Figure 5.16 shows the variation of $\ln(\varepsilon_a)$ versus $\ln(r)$ for different a / b ratios and for the different notch angles. It can be seen

from Fig.5.16 that in each case, there is a definite linear portion followed by a non-linear portion as per theoretical prediction.

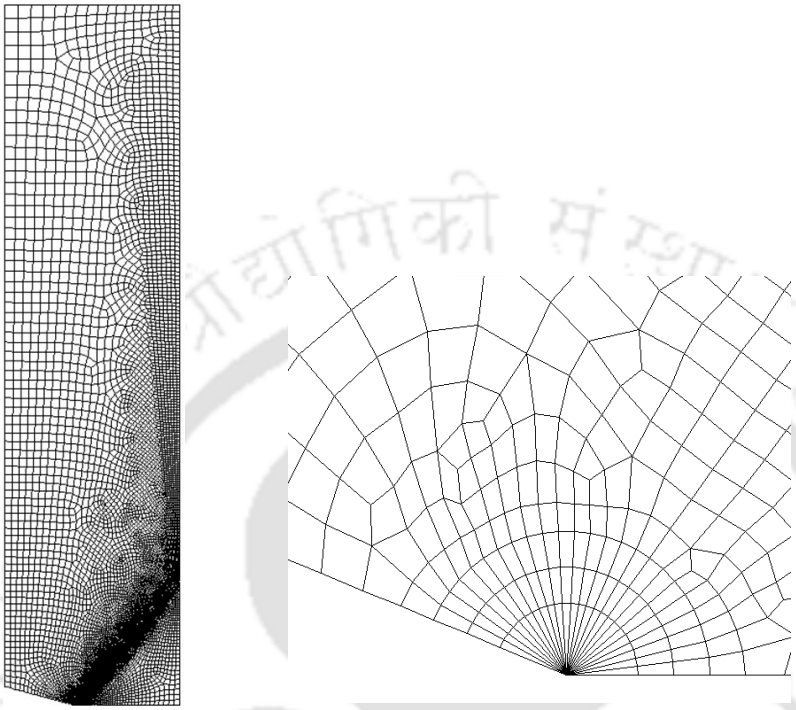

Figure 5.15 (a) Typical FE mesh used for double edge notched plate; (b) exaggerated view of notch tip corresponding to the FE mesh.

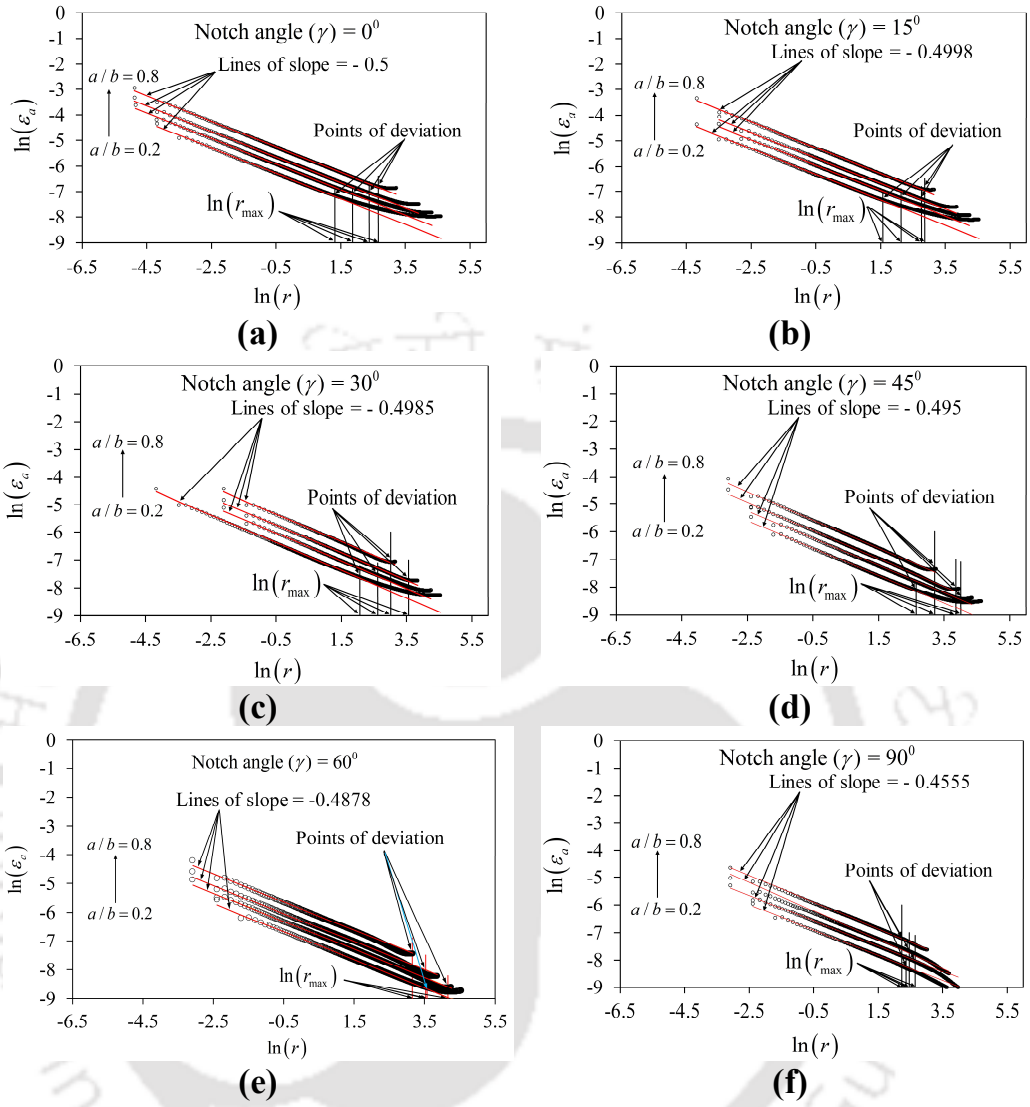

Figure 5.16 Variation of $\ln(\varepsilon_a)$ with $\ln(r)$ along the gage line for the double edge notched tensile configurations with $a/b = 0.2$ to 0.8 for different notch angles ($\gamma = 0°, 15°, 30°, 45°, 60°$ and $90°$).

Using the procedure as illustrated in section 4.2, the $r_{\max}$ values have been extracted and tabulated in Table 5.10. It is interesting to observe from the results of Table 5.10 that the $r_{\max}$ value increases with the increase in a/b for smaller notch angles $(0° \le \gamma \le 15°)$. In fact, this could be anticipated because, the crack tips are far away from their respective boundaries. Therefore, the crack length is the controlling parameter for changes in the $r_{\max}$ values. As a consequence, the $r_{\max}$ values increased with the increase in a/b ratio [101]. Similar observations have also been noticed for the crack problems by Sarangi et al. [101]. Having said that, an inverted-bell shaped trend could be noticed for $r_{\max}$ values versus a/b for the remaining notch angles as is observed in the SENT configurations. The change in the trend of the $r_{\max}$ values for the notch angles greater than 15° requires further investigation. Figure 5.17, therefore, shows the graphical variation of $r_{\max}/b$ values with a/b for different notch angles in support of the numerical results tabulated in Table 5.10.

Table 5.10 Variation of r_{max} with a / b

Notch angle γ	a / b	r_{max} (mm)
0°	0.2	3.76
	0.4	6.47
	0.6	10.88
	0.8	14.32
15°	0.2	4.80
	0.4	8.49
	0.6	15.79
	0.8	17.64
30°	0.2	7.86
	0.4	13.63
	0.6	35.26
	0.8	20.35
45°	0.2	14.06
	0.4	53.72
	0.6	47.79
	0.8	24.65
60°	0.2	35.70
	0.4	63.92
	0.6	34.32
	0.8	23.25
90°	0.2	10.64
	0.4	14.21
	0.6	11.74
	0.8	9.39

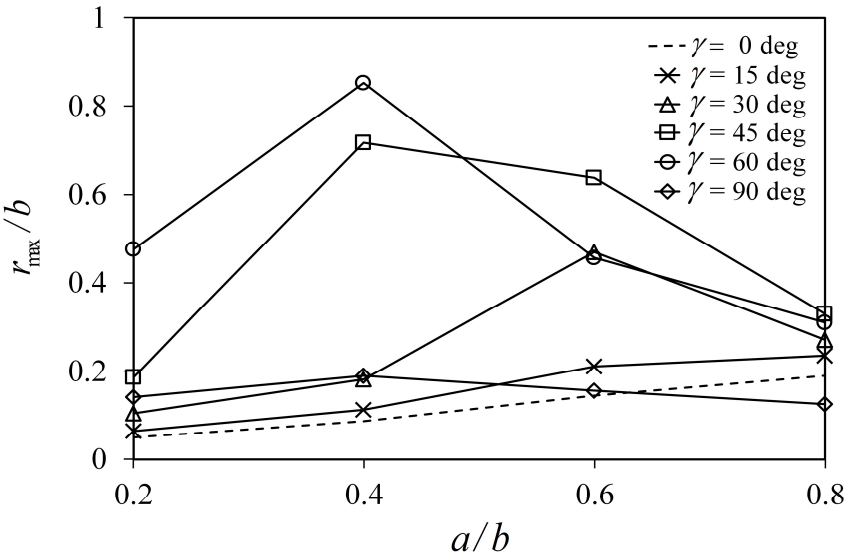

Figure 5.17 r_{max}/b variation with a/b for sharp double edge notched tensile (DENT) configurations for different notch angles γ under mode I loading condition.

5.7 Summary

In this chapter, several benchmark numerical problems are considered involving various sharp V-notched configurations viz., SENT, CNT and DENT subjected to mode I loading under plane stress conditions. This chapter clearly shows the implementation of the proposed procedure for estimation of the upper bound of the valid gage locations i.e., r_{max} for all the aforesaid notched configurations using finite element analysis. Numerical simulations are presented to show the performance of the proposed single strain gage technique at valid and invalid gage locations for a few notched cases and to substantiate the importance of appropriate selection of gage locations for the accurate determination of K_I^V in sharp V-notches. Further, the effect of a/b ratio on r_{max}, and the orientation angle of the gage line θ on r_{max} are also discussed in depth. Results clearly substantiate that the proposed single strain gage technique provides very accurate NSIFs at the valid gage locations (with a maximum error of nearly 5%). At invalid gage locations, the results have been found hugely erroneous as expected.

Chapter 6

Experimental procedures and setup

This chapter systematically discusses the experimental procedures, including details of the various test specimens employed, experimental setups, and other associated topics. Additionally, the evaluation of material properties and detailing of strain gage are also shown.

6.1 Description of the test specimens

All the experimental specimens of the present investigation have been made using commercially available PMMA (Polymethylmethacrylate) material. It is well known that PMMA is a homogeneous, isotropic and brittle material at room temperature [120]. PMMA is a great model material in experimental fracture mechanics because it is cheap and simple to create complex cracked and notched shapes [120]. Further, it has excellent linear elastic properties at room temperature. This material has long been used in studies of many aspects of LEFM [121, 122] and is still a highly preferred linear elastic isotropic material at room temperature [73, 76]. The chief advantage of this material is that it is easy to introduce sharp cracks and notches with the help of razor blades, jewellery saws etc. A historical account of PMMA in experimental fracture mechanics is reported in [120].

Two benchmark specimen geometries have been considered in the present investigation viz., a single edge notched tensile (SENT) specimen and a semi-circular bend (SCB) specimen. The schematic of the SENT specimen for experimental analyses is shown in Fig.6.1(a). Figure 6.1(b) shows the photograph of a typical specimen made of PMMA material with strain gages pasted along the gage line. Similarly, Fig.6.1 (c) shows the geometry of the SCB specimen and Fig.6.1(d) shows actual PMMA SCB specimen with strain gages. The SENT specimen has been employed more frequently in the present investigation. Plate thickness t of these two specimens in all experiments is 6 mm. Throughout the investigation, the plate width b of the all the SENT specimens is 100 mm, and height of the plate ($2h$) is 300 mm. Dimensions and loading conditions

in all the test specimens have been chosen to ensure that plane stress conditions prevail during the experiments.

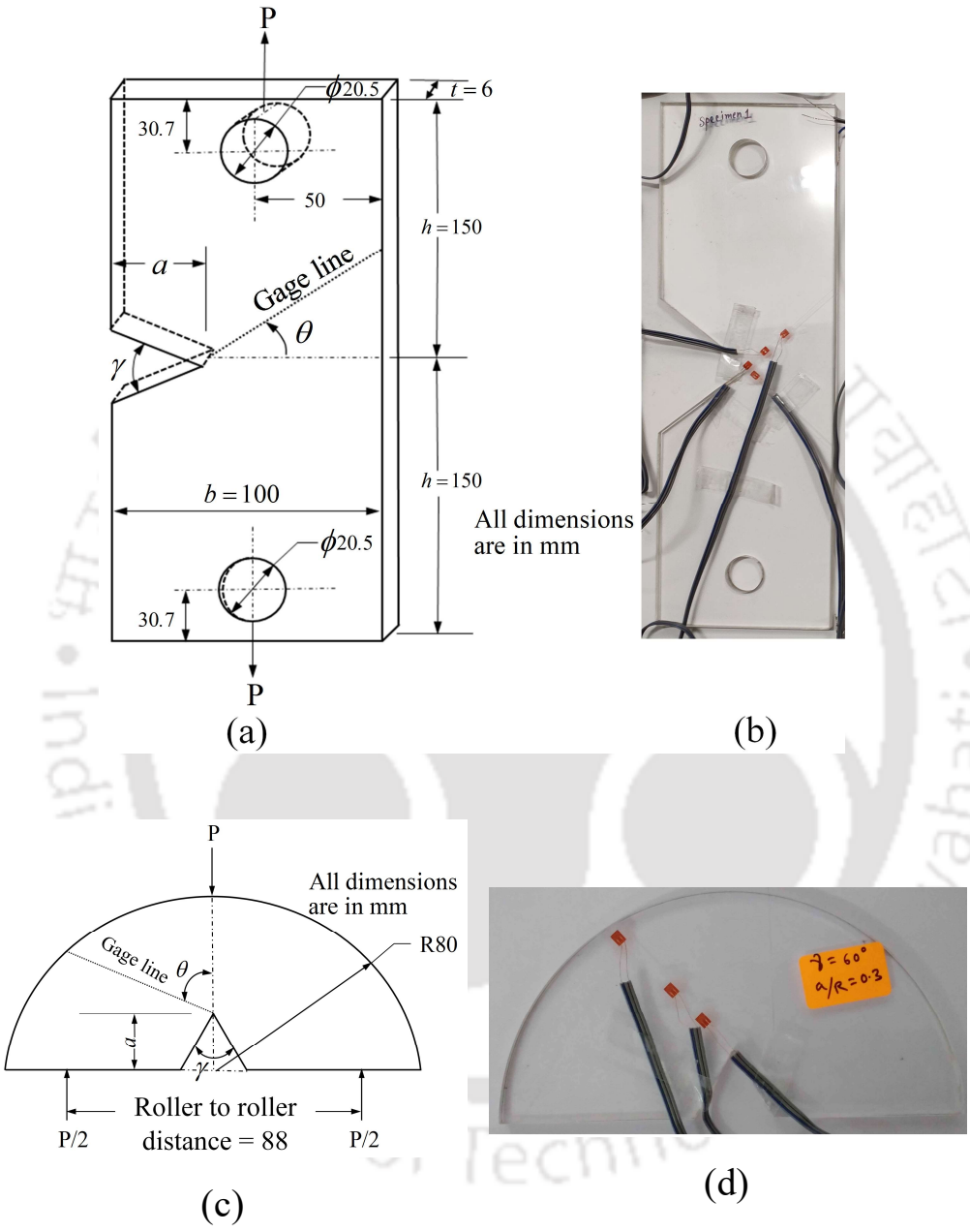

Figure 6.1 Details of experimental specimens (a) 3D geometry of the SENT specimen; (b) Typical SENT specimen made of PMMA; (c) Schematic diagram of SCB specimen; (d) Typical SCB specimen made of PMMA.

The loading holes in the SENT specimen at the ends are intended to load the specimen under tensile loading using clevis grips and pins. The location of these loading holes relative to the free ends are decided by the clearances available in the clevis grips. It is to be noted here that all the experimental specimens have been loaded three times to ensure the repeatability of the results. Furthermore, two identical specimens for a particular sharp V-notched configuration have been considered to ensure further the reproducibility of the experimental results.

In the present investigation it was intended to carry out tests for different values of $a/b = 0.3, 0.4$ and 0.6 .After fabrication using laser machine and manual sharpening of a V-notch using a razor blade, a slight change in the intended a/b ratios have been noticed using optical profile projector. For example, for $a/b = 0.3$, the final finished values are found between 0.29 to 0.32, for $a/b = 0.4$, the resulting values are in the range 0.37 to 0.43. Similarly, for $a/b = 0.6$, the final dimensions obtained are in the range 0.55 to 0.64. As these deviations from the intended values are minimal, therefore intended values of a/b have been used in the numerical simulations and while reporting the results for different a/b ratio.

6.2 Preparation of the test specimens

All experimental specimens of the present investigation have been cut with the help of a 2.5 kW CO_2 laser machine (make: LVD) including the V-notches. To include a sharp V-notch in the specimen, firstly the specimen of desired dimensions is prepared with a notch length of a mm and notch angle γ. Due to the finite radius of the laser beam, the resulting notch is not sharp but slightly rounded. A sharp razor blade is then used to sharpen the notch tip by sliding the razor blade along the surfaces of the notch edges as shown in Fig.6.2. In this way, a sharp V-notch of root radius 0.155 mm approximately has been achieved. Fig.6.3 shows the photograph of a notched specimen (before and after sharpening) obtained using the optical profile projector which helps examine the sharpness of the notch tip of a typical V-notched specimen.

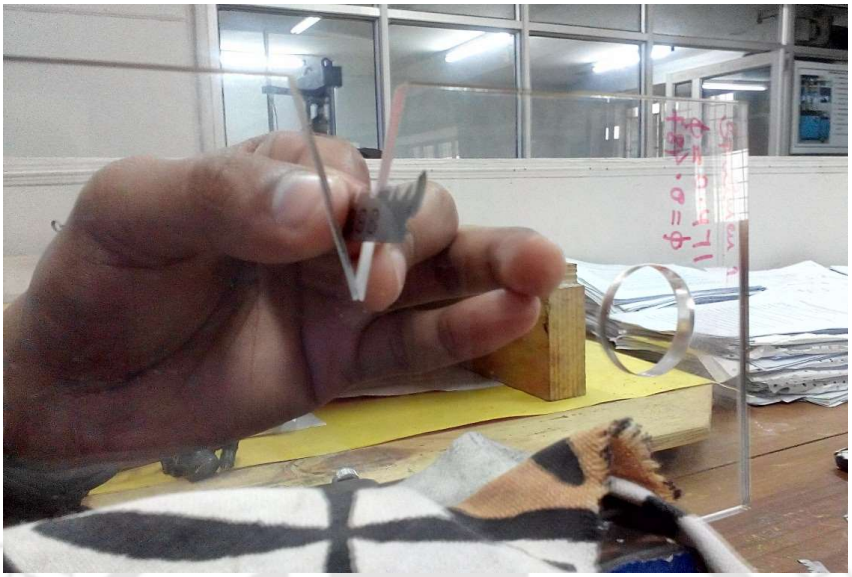

Figure 6.2 Notch tip sharpening using a razor blade.

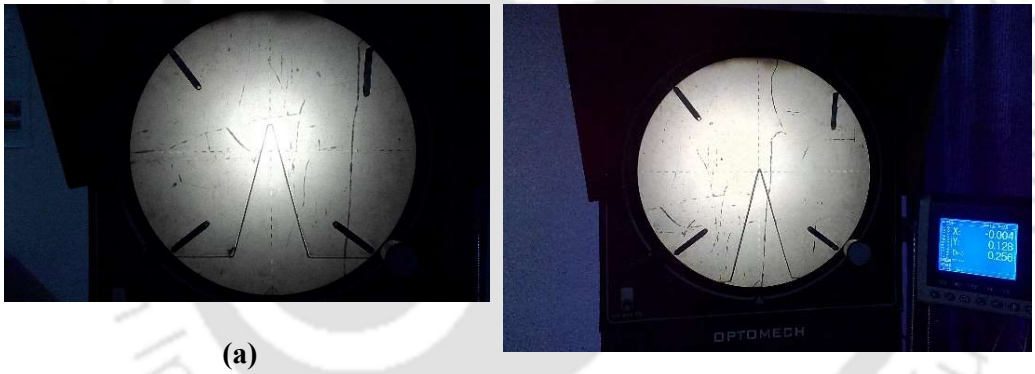

(a) **(b)**

Figure 6.3 V-notch (a) before sharpening; (b) after sharpening.

6.3 Elastic properties of selected PMMA material

While conducting experiments for the determination of accurate NSIFs using strain gages, accurate values of Young's modulus E and Poisson's ratio ν are necessary which can be justified by referring to Eqs. (4.12), (4.17) and (4.18). To determine the elastic material properties of selected PMMA, typical tensile test coupons (Table 6.1) have been made cut from the same parent sheet from which V-notched specimens are

cut. Two geometrically identical rectangular PMMA specimens have been tested for checking the reproducibility and each specimen has been tested thrice for the same purpose. Therefore, six tests in total have been conducted to obtain the Young's modulus E, and Poisson's ratio ν of the selected commercially available PMMA material. During these tensile tests, two strain gages with a gage length of 3 mm and 120 Ω resistance have been pasted on each specimen to measure the strain data in the longitudinal lateral direction. All tensile tests have been conducted as per the ASTM D638 standard.

In each tensile test, the specimen has been monotonically loaded in a closed loop servo-hydraulic INSTRON 8801 universal testing machine (100 kN capacity) under displacement control with an actuator speed of 0.25 mm/min. Fig.6.4 shows the typical rectangular flat specimen of PMMA with strain gages.

Table 6.1 Details of the tensile test specimen for determination of E and ν of PMMA

Strain measurement	Test	Specimen type	Specimen geometry (All dimensions are in mm)	Number of specimens tested
Strain gage	Tensile	Rectangular specimen	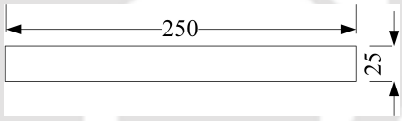	2

Figure 6.4 Typical rectangular flat PMMA specimen pasted with biaxial strain gages for determination of material properties.

In the aforesaid tests, the measured strains have been stored, digitized and processed with the help of the data acquisition system (cDAQ-9178) of National Instruments (NI) supported by the LabVIEW software. Figures 6.5-6.7 show the raw data obtained from the tensile tests and the best-fitted lines to these raw data corresponding to each case. Figures 6.5(a), 6.6(a) and 6.7(a) show the engineering stress-strain diagrams for determination of the Young's modulus E .The slope of the best-fit line in each of these figures is the Young's modulus E. Figures 6.5(b), 6.6(b) and 6.7(b) show the axial transverse strains versus load for the measurement of Poisson's ratio ν. According to ASTM E132-04 test procedure, Poisson's ratio ν is defined as the ratio of the slope of best-fit line of transverse strain to the slope of best-fit line of axial strain.

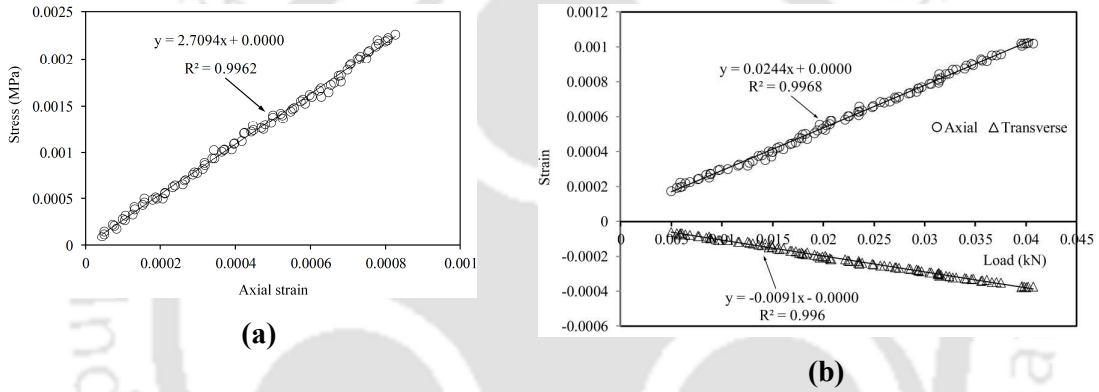

(a) **(b)**

Figure 6.5 Trial 1 (tensile testing of specimen 1).

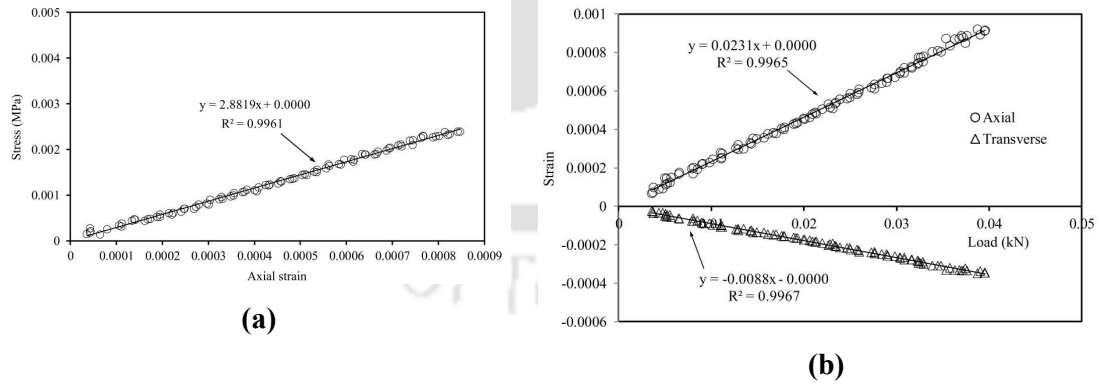

(a) **(b)**

Figure 6.6 Trial 2 (tensile testing of specimen 1).

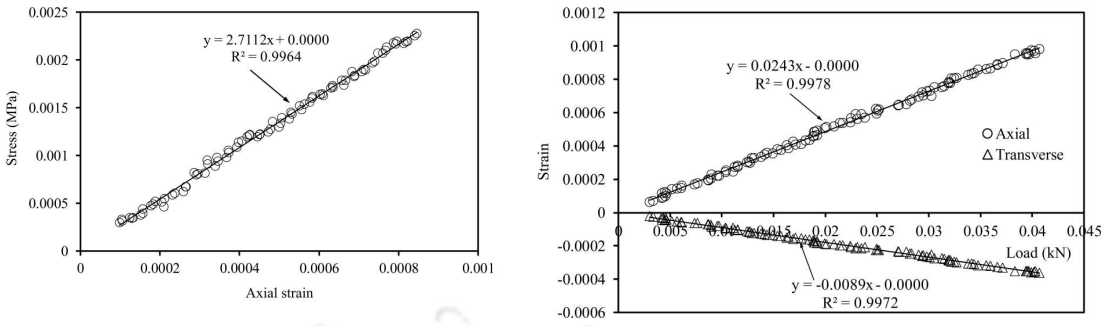

(a) **(b)**

Figure 6.7 Trial 3 (tensile testing of specimen 1).

It should be noted that all the experimental specimens of the present investigation have been fabricated from two different PMMA sheets. This was necessary as one single parent sheet was unable to accommodate all the test specimens of the present work. Tensile tests as described above have been conducted on the coupons from both the parent material sheets. The results in Figs.6.5-6.7 and Table 6.2 presents the results of the tensile tests corresponding to one parent material sheet. Table 6.2 also shows the mean and standard deviation of the experimental results of material properties. The mean value $E = 2.7758$ GPa and the mean value $\nu = 0.3696$ are then considered as the material properties of one of the two PMMA sheets. The above material properties have been used for the specimens in Chapter 7. The elastic properties of another sheet have been found to be equal to $E = 3.207$ GPa and $\nu = 0.381$. These values have been employed for the specimens of the Chapter 8.

Table 6.2 Experimental results for determination of material properties E and ν of PMMA

Case	Specimen dimensions	E (GPa)	ν
Specimen 1	Length =250 mm, width =25 mm, thickness =6 mm	2.7094	0.3730
		2.8819	0.3809
		2.7112	0.3663
Specimen 2	Length =250 mm, width =25 mm, thickness =6 mm	2.7208	0.3725
		2.8101	0.3660
		2.8214	0.3590
	Mean	**2.7758**	**0.3696**
	Std. Dev	**0.0723**	**0.0075**

6.4 Details of experimental procedure and setup

Following subsections deal with the further information on experimental procedures adopted in the presented investigation on the sharp V-notched SENT and SCB specimens.

6.4.1 Details of strain gages used

Strain measurements on all the loaded specimens have been carried out using the electrical resistance strain gages of type FLA-1-350-11-3LT, Make: TML Japan. These gages have the gage length 1 mm and 350 Ω resistance. Details of the specification of strain gages used are given in Table 6.3. Fig.6.8 shows the photograph of a typical strain gage. Utmost care has been taken while pasting the strain gages on the test specimens to ensure perfect and defect-free bonding following the standard procedures for strain gage pasting.

Table 6.3 Details of TML strain gage

Parameter	Specifications
Type	FLA-1-350-11-3LT
Gauge length	1 mm
Gauge factor	2.10 ± 1 %
Gauge resistance	350 ± 1.5 Ω
Transverse sensitivity	0.6 %
Lead wires	10 / 0.12 3W 3m
Test condition	23°C 50% RH

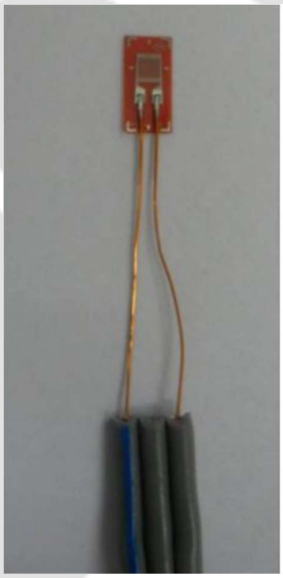

Figure 6.8 A typical 1 mm gage length, pre-wired TML strain gage.

All strain gages have been pasted very carefully at selected locations along the gage lines (at gage line orientation θ and strain gage orientation β). The radial positions and orientation of strain gages have been cross-checked using a profile projector. Figure 6.9 shows the photograph of an optical profile projector showing clearly the orientation of a typical strain gage pasted on the specimen.

Figure 6.9 Optical profile projector for verification of orientation and location of a strain gage.

6.4.2 Details of data acquisition system for strain measurements

Data acquisition is the process of sampling signals that measure real world physical conditions and converting the resulting samples into digital numeric values that can be manipulated by a computer. The measured strains have been acquired, digitized and processed using NI Data Acquisition System comprising of cDAQ9178 chassis. NI 9219 a universal analog input module having 4 channels and 24 bit has been used for the measurement of force from the INSTRON machine load cell in terms of voltage signals. This has been reached by connecting a BNC cable between the load cell of the INSTRON machine and the NI 9219 module. In this manner, the load has been measured simultaneously along with the strains. NI 9237 module (4 channels 24 Bit, analog input module) has been employed for strain measurements.

In all the experiments, the quarter bridge Wheatstone bridge circuit has been employed for the measurement of strains. For this purpose, NI 9944 (Quarter bridge completion accessories) has been added to the NI 9237 strain gage module. The

sampling rate (also known as sampling frequency) for data in all of these modules has been set to 2000 Hz.

LabVIEW is a graphical user interface (GUI) software widely used for data acquisition. LabVIEW 9 has been used in the present investigation to interface the DAQ system with a computer and this software is also used for processing and storing of experimental data. In all the experiments, offset-nulling and shunt calibration of strain gages have been done using the LabVIEW. An excitation voltage of 2.5V is set in all the experiments. Fig.6.10 shows the screenshot of a typical virtual instrumentation using DAQ assistant of the LabVIEW used in one of the experiments.

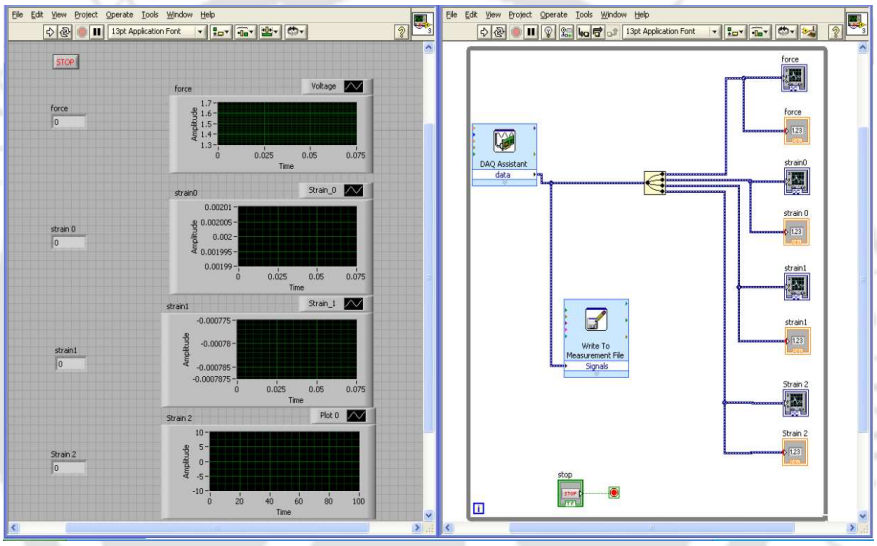

Figure 6.10 Typical LabVIEW programming for force and strain measurement.

6.4.3 Testing arrangement

All the V-notched specimens of the present work have been monotonically loaded in a closed loop servo-hydraulic INSTRON 8801 universal testing machine (100 kN capacity) under displacement control with an actuator speed of 0.25 mm/min. The specimen with strain gages is connected to the INSTRON machine using clevis grips and pins. Spacer blocks have been used in both the top and bottom clevis arrangements, as illustrated in Fig.6.11, to prevent the specimen from bending during tensile loading (i.e., pure mode I) and to guarantee that the specimen is subjected to solely axial tensile loads. The dimensions of the spacer blocks are machined to ensure perfect alignment

of the specimen. The alignment of the specimen is also checked using a plumb bob before loading as shown in Fig.6.12. Figure 6.13 shows the complete experimental setup highlighting all the components of the setup as described above (along with the data acquisition system).

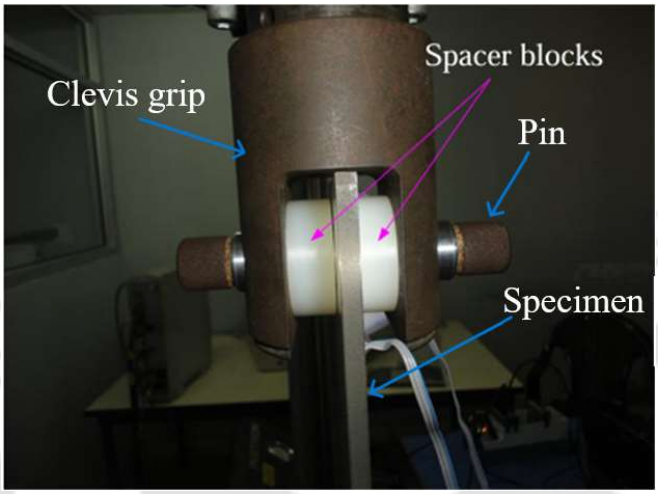

Figure 6.11 Specimen with the spacer blocks in clevis grips.

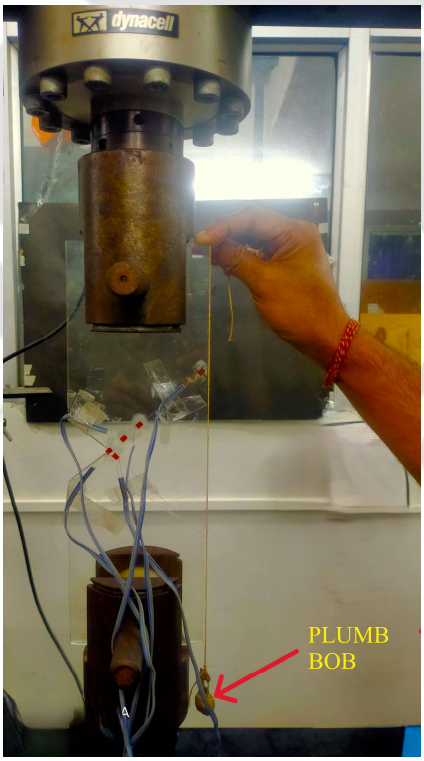

Figure 6.12 Checking of alignment of a specimen using a plumb bob.

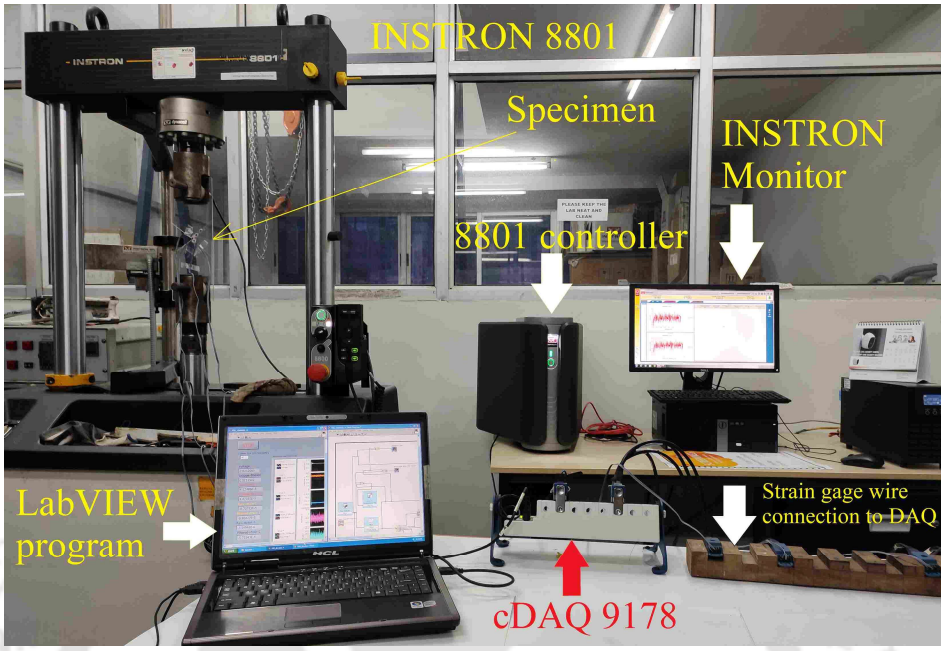

Figure 6.13 Complete experimental setup.

6.5 Summary

This chapter provides complete details of the proposed experiments and experimental setup, description of the geometry of the test specimens, preparation of the test specimens, evaluation of material properties of the experimental specimens, description of strain gage used and all other details needed to conduct the experiments. The type of notched configurations selected for the experiments viz., SENT and SCB made of PMMA material, have been described in detail in this chapter. The number of test specimens and number of repeated tests on each specimen have also been stated in this chapter to ensure the reproducibility of results.

This page is left blank intentionally

Chapter 7

Experimental validation of r_{min}

A sharp V-notched plate under plane stress loading conditions is always accompanied by a strong three-dimensional (3D) stress-strain region close to the notch tip, followed by a 3D to 2D transition state and a region dominated by the 2D stress-strain field. Li and Guo [119] were the first to find the extent of these zones for a sharp V-notch using extensive 3D finite element studies. However, till date no experimental verification of these results have been made. Clearly, it is important to know the extent of the above fields for accurate measurement of field variables. In the present chapter, numerical and experimental verification of the extent of the 3D stress-strain field, 3D-2D transition zone and plane stress zone ahead of the tip of a sharp V-notch given by Li and Guo [119] has been carried out to suggest a minimum radius required for the identification of the plane stress dominant zone. As stated earlier in section 4.2, this value has been termed in this work as r_{min} which provides minimum radial distance allowed for locating a strain gage. Indeed, knowing this value *a priori* is vital for accurate sampling of the 2D field variables in any experimental study on the sharp V-notched configurations.

7.1 Out-of-plane constraint factor T_z

A 3D stress field dominates near a V-notch tip when the out-of-the-plane stress σ_z influences the state of stress. To describe this more conveniently, a special parameter known as the out-of-plane constraint factor, T_z defined as

$$T_z = \frac{\sigma_z}{\sigma_x + \sigma_y} \tag{7.1}$$

is introduced to quantify the conditions of plane stress, plane strain and 3D state of stress in the vicinity of a sharp V-notch [119]. Thus, in the plane stress conditions,

$$T_z = 0 \tag{7.2}$$

It is known that in the plane strain conditions,

$$\sigma_z = \nu(\sigma_x + \sigma_y) \tag{7.3}$$

Thus, in the plane strain conditions

$$T_z = \nu \tag{7.4}$$

Eq. (7.2) and Eq. (7.4) altogether imply that the parameter T_z generally varies from 0 to ν to represent different states of stress. For cases where neither plane stress nor plane strain prevails (i.e., in the case of 3D stress-strain state), T_z assumes the values as

$$0 < T_z < \nu \tag{7.5}$$

In the present study, T_z is normalized by T_{z0} which is the value of $T_z(z=0)$ at the notch tip. Thus, different states of stress can be ascertained using the following relations

$$\left.\begin{array}{rl} T_z / T_{z0} = 0 & \text{Plane stress} \\ T_z / T_{z0} = 1 & \text{Plane strain} \\ 0 < T_z / T_{z0} < 1 & \text{3D state of stress} \end{array}\right\} \tag{7.6}$$

The value of the above normalized constraint factor can be computed using numerical methods such as the FE method. According to Li and Guo [119], the 3D stress-strain state prevails till a radial distance of $0.5t$ and 3D-2D stress-strain transition zone continues until $1.25t$, where t is the thickness of the sharp V-notched plate.

7.2 Numerical results and discussion

The purpose of this section is to verify the r_{min} value recommended by Li and Guo [119], for the thin plates under plane stress conditions using 3D FE analyses. For this purpose, a double-edge V-notched tensile specimen (DENT) considered by Li and Guo [119] has been considered here with different notch angles and plate thicknesses. DENT is assumed to be under the plane stress conditions. All FE analyses in this numerical work have been carried out using ANSYS®. Twenty nodded isoparametric quadrilateral elements (Q20) having three degrees of freedom (DOF) per node (section 3.3) have been used for the FE modelling of the notched configurations. These conventional Q20 elements have been collapsed to generate the grid around the notch tip in a spider-web pattern.

A DENT specimen subjected to uniform tensile loading is shown in Fig.7.1(a). Considering the symmetry in terms of both loading and geometry, only one-eighth of the DENT plate has been analysed (the shaded portion in Fig.7.1(b)). Boundary conditions and loading of the selected domain are also shown in Fig.7.1(b). Table 7.1 shows the geometric and material properties of the DENT. The out-of-plane constraint factor T_z has been observed along three lines, viz., a line along the mid-plane ($z = 0.01$, $y = 0$; mid-plane line), free surface ($z = t/2$, $y = 0$; surface plane line), and a line along a quarter plane ($z = t/4$, $y = 0$; mid-way line) as shown in Fig.7.1(b). A typical mesh (after the convergence study) of the selected analysis domain is shown in Fig.7.2(a) and the mesh near the notch tip is shown in Fig.7.2(b).

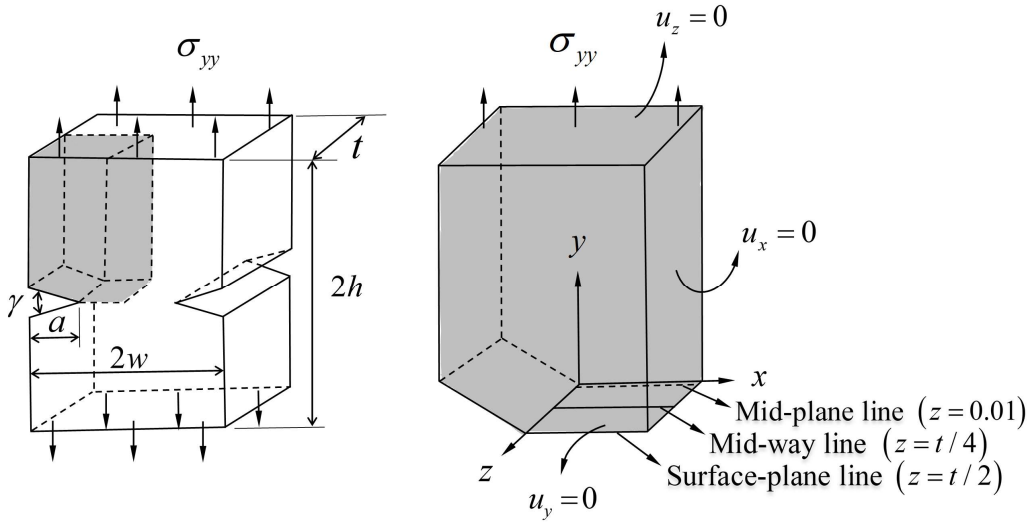

Figure 7.1 (a) DENT subjected to uniform tensile loading; (b) One-eighth of the DENT plate.

Table 7.1 Geometrical data and material properties of the DENT configuration

Description	Value
Notch angle, γ	$0°, 75°, 90°, 135°, 150°$
Plate thickness, t	0.1, 1.0, 2.0 and 4.0 mm
a/w ratio	0.35
Young's modulus, E	200 GPa
Poisson ratio, ν	0.33
Height, $2h$	20 mm
Width, $2w$	12 mm
Notch length, a	2.1 mm

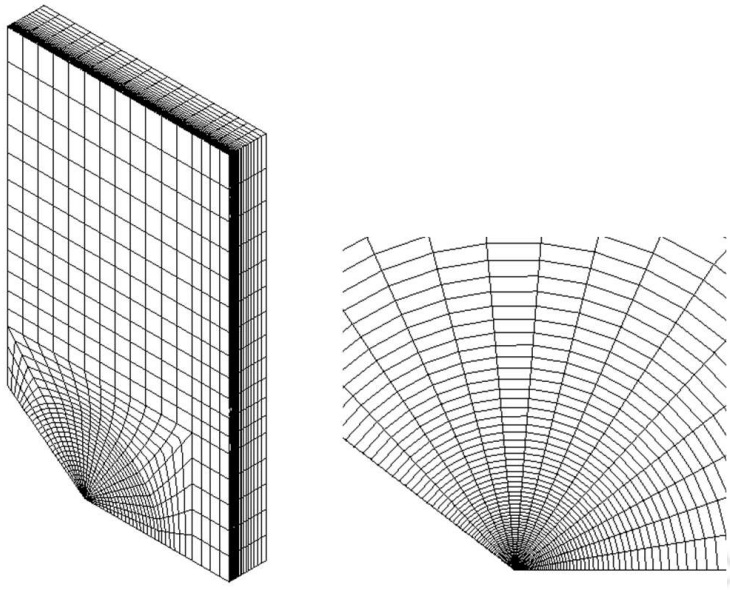

Figure 7.2 (a) FE meshing of the one-eighth portion of the DENT plate; (b) Spider web mesh pattern at the notch-tip.

As discussed previously, the parameter T_z (out-of-plane constraint factor) has been computed along the aforementioned three lines to figure out different zones of stress-strain fields around the notch tip across the thickness of the plate. The distance from the notch tip, x (Fig.7.1(b)) is normalized as x/t in all the plots of the present section. Firstly, mesh convergence has been studied with three different mesh densities in increasing order of number of elements (NE) and number of nodes (NN) for $t = 2$ mm and $\gamma = 75°$. For this purpose, the values of T_z / T_{z0} have been computed along the mid-plane line (Fig.7.1(b)) and compared with the results of Li and Guo [119]. Figure 7.3 shows the results of the mesh convergence study. The results presented in Fig.7.3 clearly show the convergence of the results with the reference solutions [119] as mesh density is increased. Therefore, the finest mesh (Mesh 3) as shown in Fig.7.2 with the highest NE and NN has been used in all FE analyses of this section.

Figure 7.3 also shows that a strong 3D field within the radius of half the plate thickness (marked by a vertical dotted line) and 3D-2D transition state persist approximately up to a radial distance of 1.25 times the plate thickness (i.e., $x / t = 1.25$) from the notch tip. Further away from this radius, the plane stress

conditions ($T_z / T_{z0} = 0$) dominate. A slight dip in T_z / T_{z0} after $x/t = 0.5$ has also been observed by Li and Guo [119]. As can be noticed from the results in Fig.7.3 that $r_{\min}$ for the sharp V-notch problems can be assigned a value of $1.25t$ as suggested by Li and Guo [119] or $1.5t$ as suggested by Nakamura and Parks [114], the latter being a more conservative and definitive limit.

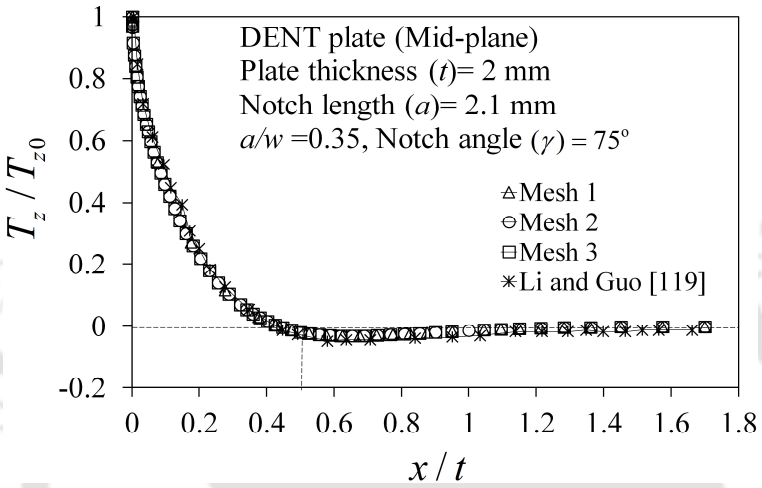

Figure 7.3 Results of the 3D FE mesh convergence study.

Fig.7.4(a) shows the influence of the notch angle γ on the out-of-plane constraint factor T_z in the mid-plane. It can be seen from Fig.7.4(a) that all three zones, viz., 3D, 3D-2D transition and 2D zones are distinctly visible for all the notch angles. At the notch-tip ($x/t = 0$), the ratio $T_z / T_{z0} = 1$ which represents the plane strain condition. Subsequently, a strong 3D state of stress prevails up to a radial distance of $x/t = 0.5$ where $0 < T_z / T_{z0} < 1.0$. When x/t further increases, the ratio T_z / T_{z0} shifts towards zero and eventually reaches the state of plane stress condition ($T_z / T_{z0} = 0$) at about $x/t = 1.25$. From these results also, it can be noticed that $r_{\min}$ for the sharp V-notch problems can be recommended as $1.25t$ as suggested by Li and Guo [119] or $1.5t$ as suggested by Nakamura and Parks [114].

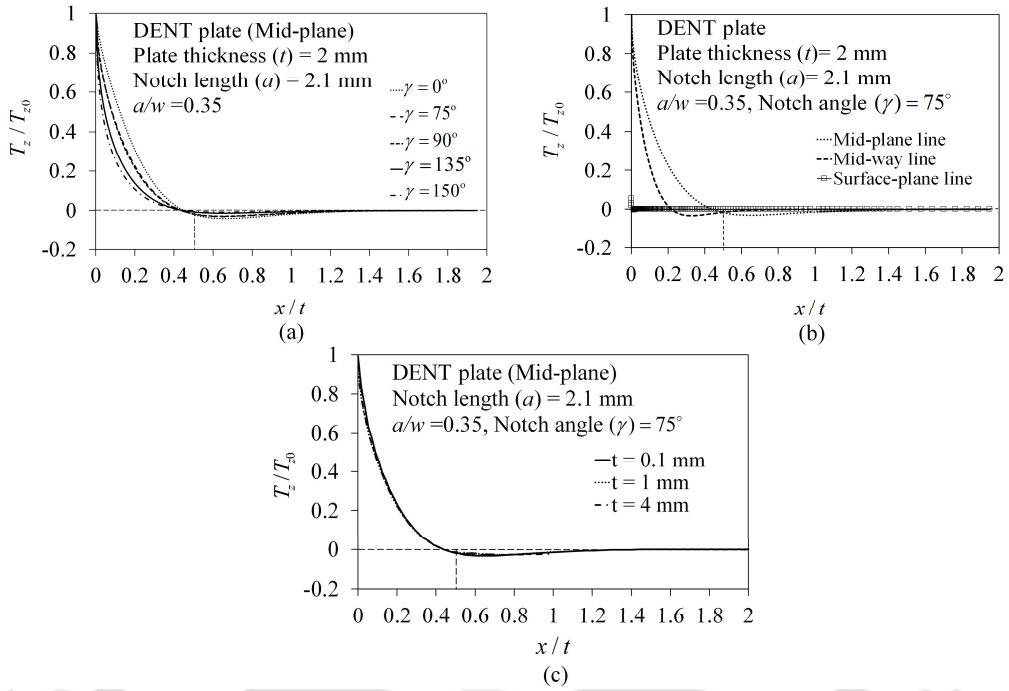

Figure 7.4 Distribution of T_z ahead of notch tip in the DENT configuration (a) Influence of the notch angle γ ; (b) Influence of the location; (c) Influence of the plate thickness t.

Figure 7.4(b) shows the distribution of T_z ahead of the notch tip along the three different lines chosen on the plane $y = 0$, viz., mid-plane line, quarter-plane line (or mid-way line) and free surface line (or surface-plane line) as discussed previously (Fig.7.1(b)) for the notch angle $\gamma = 75°$. Figure 7.4(b) depicts that similar to the previous observations, at the mid-plane the 3D state and 3D-2D stress transition state exist up to a radial distance of $0.5t$ and $1.25t$, respectively and the state of plane stress finally dominates beyond $x / t = 1.25$. On the other hand, at the free surface, 3D and 3D-2D transition states vanish immediately after the notch tip. Thus, one can clearly notice from Fig.7.4(b), that the extent of effect of 3D field decreases from the mid-plane to the outer surface. This observation agrees well with the results of Li and Guo [119]. As it will be discussed later, the results based on measuring the surface strains on the free surface of the specimen using the strain gages better corroborate the results of the mid-plane.

The influence of the plate thickness t on the distribution of T_z ahead of the notch tip has been studied along the mid-plane line for $\gamma = 75°$ and results have been presented in Fig.7.4(c). All the values of t considered in Fig.7.4(c) ensure plane stress conditions. Results in Fig. 7.4(c), show that as long as the specimen is under plane stress conditions, the influence of plate thickness t on the distribution of T_z ahead of the notch tip is negligible for a given notch angle γ as expected. Results of Fig.7.4(c) once again confirm that the r_{min} can be considered equal to either $1.25t$ or $1.5t$. Further, all results in Fig.7.4 clearly demonstrate that $r_{min} = 1.5t$ is the most dependable value for the safe estimation of the plane stress field variables.

7.3 Experimental results and discussion

Experimental verification of r_{min} value found by the 3D FE analysis in the previous section has been carried out using several mode I experiments. This value is verified in terms of accuracy of the mode I NSIFs of the single edge notched tensile (SENT) specimen. For this purpose, the proposed strain gage technique has been employed. The schematic of the SENT specimen for this experimental investigation is shown in Fig.6.1(a).

Table 7.2 shows the geometrical data and the material properties of the SENT specimens employed in the experiments aiming for validation of r_{min} which is discussed in this chapter. As mentioned in section 6.1, the plate width b of the test specimens is 100 mm, the height of the plate ($2h$) is 300 mm and the plate thickness t is 6 mm.

Table 7.2 Material and geometrical data of the SENT specimens

Description	Value
Width, b	100 mm
Height, $2h$	300 mm
Plate thickness, t	6 mm
Notch angle, γ	$30°$, $75°$
Notch length to width ratio, a/b	0.3
Young's modulus, E	2.7758 GPa
Poisson's ratio, ν	0.3696

For the said experimental investigation, two different notch angles $\gamma = 30°$ and $\gamma = 75°$ of the SENT specimen have been tested with a notch length to plate width ratio, $a/b = 0.3$ for each of the above two notch angles. Two identical specimens have been tested for each of the above two notch angles to ensure the reproducibility of the experimental results (section 6.4). Moreover, all four specimens have been loaded thrice to further ensure the repeatability of the results. This has resulted in a total of 12 experiments for the verification of r_{min} value in this chapter. As stated in Chapter 6, a closed-loop servo hydraulic INSTRON 8801 machine with a capacity of 100 kN has been used to load all the specimens under displacement control mode with an actuator speed of 0.25 mm/min. A 25 kN load cell has been employed in the INSTRON 100 kN machine in all experiments to measure the applied load. Strain gages (Type: FLA-1-11-3LT and Make: TML Japan) with 1 mm gage length and 350 Ω resistance have been pasted on the specimens.

After following the fabrication procedures explained in Chapter 6, the a/b values of the specimens were found to be in the range of 0.29 to 0.32 instead of 0.3 as intended. As these deviations from the intended value of 0.3 are practically small, so this value ($a/b = 0.3$) has been mentioned throughout in the results of the present investigation.

Using the measured strains at different locations along the gage line (Fig.6.1(b)), the mode I NSIFs corresponding to each of the measured strains have been determined using Eq. (4.12) and Eq. (4.17). The NSIFs are then normalized as

$$F_I = \frac{K_I}{\sigma\sqrt{\pi}\,a^{1-\lambda_1}} \tag{7.7}$$

and the % relative error in F_I is calculated as

$$\%\ \text{Rel.error} = \left| \frac{F_I^{reference\ solution} - F_I^{experimental}}{F_I^{reference\ solution}} \right| \times 100 \tag{7.8}$$

where $F_I^{reference\ solution}$ and $F_I^{experimental}$ are the reference and present experimental solutions of the mode I NSIFs of the selected SENT specimens.

$F_I^{reference\ solution}$ of the selected experimental specimens have been obtained using a recently proposed finite element based the point substitution displacement technique by Hussain and Murthy [54]. Figure 7.5 shows a typical finite element mesh considered after the convergence study to determine the reference normalized NSIFs. Due to the symmetry of the SENT configuration, only one-half of the specimen has been analysed with symmetric boundary conditions (Fig.7.5). Collapsed Q8 elements have been arranged in a typical spider web pattern around the notch tip. Eight-nodded isoparametric quadrilateral elements (Q8) have been used everywhere, including the notch-tip, in both the SENT configurations (Table 7.2). Table 7.3 shows the computed reference normalized NSIFs of the selected SENT specimens for substantiation of r_{min} value.

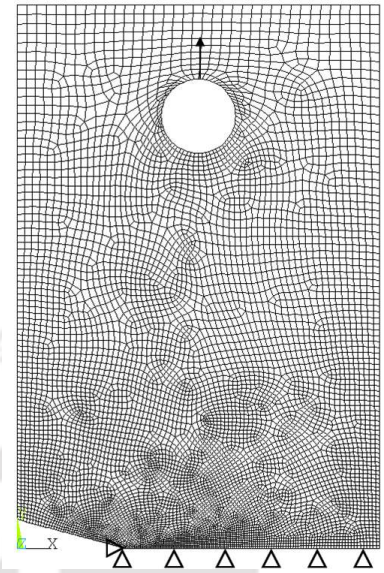

Figure 7.5 Typical finite element mesh used for $\gamma = 30°$ (NE=7758, NN=23735).

Table 7.3 Reference values of the normalized NSIFs of the SENT specimens

γ	a / b	F_I
30°	0.3	1.6645
75°	0.3	1.8254

Figure 7.6 shows the images of the selected SENT specimens (as per the dimensions given in Table 7.2) made of PMMA with strain gages. For the SENT specimen with $\gamma = 30°$, the gage line orientation (Fig.4.1(a)) is arbitrarily chosen at $\theta = 60°$ and the corresponding gage orientation $\beta = 50°$ can be obtained using Eq. (4.15). As $\gamma > 40°$ for the second SENT specimen (where $\gamma = 75°$), $\theta = 42°$ and $\beta = 42°$ have been obtained after solving simultaneously Eqs. (4.15) and (4.16).

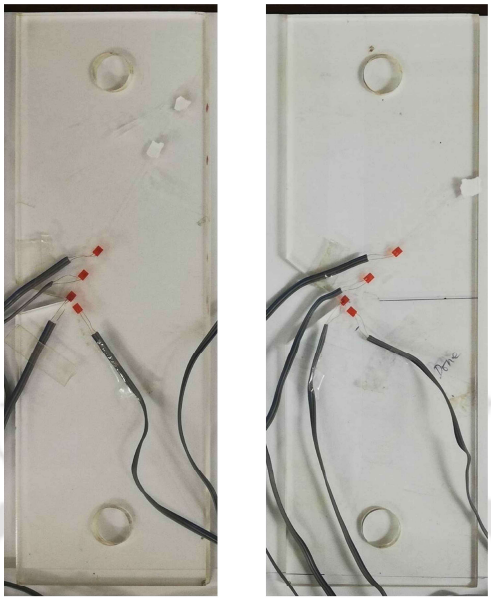

(a) (b)

Figure 7.6 SENT specimens employed in the experiments (a) SENT specimen with $\gamma = 30°$; (b) SENT specimen with $\gamma = 75°$.

It can be noticed from Fig.7.6 that each specimen has been tested with more than one strain gage located at different radial distances from the notch tip to assess r_{min} by studying the effect of different stress-strain states on the measured mode I NSIFs. Table 7.4 shows the selected radial locations of the strain gages in the two specimen configurations. Table 7.4 also provides the extents of the 3D stress-strain zone and 3D to 2D transition zone as given by Li and Guo [119]. As the plate thickness $t = 6$ mm is small compared to other dimensions of the specimens, it is assumed that the specimens are under plane stress conditions except in the vicinity of the notch tip [114, 119].

Table 7.4 Selected radial strain gage locations (thickness $t = 6$ mm ; $0.5t = 3$ mm ; $1.25t = 7.5$ mm)

γ	a / b	r_1(mm)	r_2(mm)	r_3(mm)	r_4(mm)
30°	0.3	2	5	15	30
75°	0.3	2	5	15	30

As depicted in Fig.7.6, the radial gage location $r_2 = 5$ mm (Table 7.4) has been chosen on the negative gage line (i.e., at gage line orientation $-\theta$) whereas the other three radial gage locations viz., $r = 2$ mm, 15 mm and 30 mm have been chosen on the positive gage line (i.e., at gage line orientation $+\theta$), so that gages get space and can be pasted easily. It is to be noted here that reversing the gage line orientation, i.e., from $+\theta$ to $-\theta$ causes no effect on the strain gage readings (Section 4.1).

As the thickness of the specimen is 6 mm, the first gage location $r_1 = 2$ mm has been intentionally selected to be in a 3D stress-strain zone, i.e., less than $0.5t$. The second radial location $r_2 = 5$ mm is selected to be under the 3D-2D transition zone, i.e., $0.5t < r < 1.25t$ (or $1.5t$). Both the radial locations $r_3 = 15$ mm and $r_4 = 30$ mm have been selected such that they are well within the valid plane stress region, i.e., $r > 1.25t$ (or $1.5t$) whilst r_4 being significantly far away from the notch tip. At such large radial distances, it can be anticipated that Eq. (4.14) or Eq. (4.17) may not hold appropriate due to the dominance of other higher-order non-singular Williams' coefficients than those selected in the above equation. This location is deliberately selected to observe whether or not the above coefficients dominate or not for the selected SENT configuration.

Figure 7.7 represents the foot-corrected graphs of measured strain ε_a (encircled data points) at $r_1 = 2$ mm versus the applied load for the SENT specimen with $\gamma = 30°$ and $a/b = 0.3$. These plots correspond to the three repeated tests of the first specimen. While Fig.7.8 shows plots of ε_a at $r_4 = 30$ mm versus the applied load for the two identical SENT specimens of $\gamma = 75°$ and $a/b = 0.3$ in the first test. Figures 7.7 and 7.8 also show the best-fit straight lines (solid lines) with the associated slopes and the statistical coefficient R^2 of the fit. In all these repeated tests (Figs.7.7 and 7.8), the values of R^2 are close to unity and indicate that the measured strains are linearly proportional to the applied load. In addition, the slopes of the best-fit straight lines in all three graphs of Fig.7.7 are approximately the same. A similar trend can also be noticed in Fig.7.8 between two specimens in the first test. These observations clearly indicate the good calibration of the entire experimental procedure and the repeatability of the results. Similar trends have been observed in the remaining experiments.

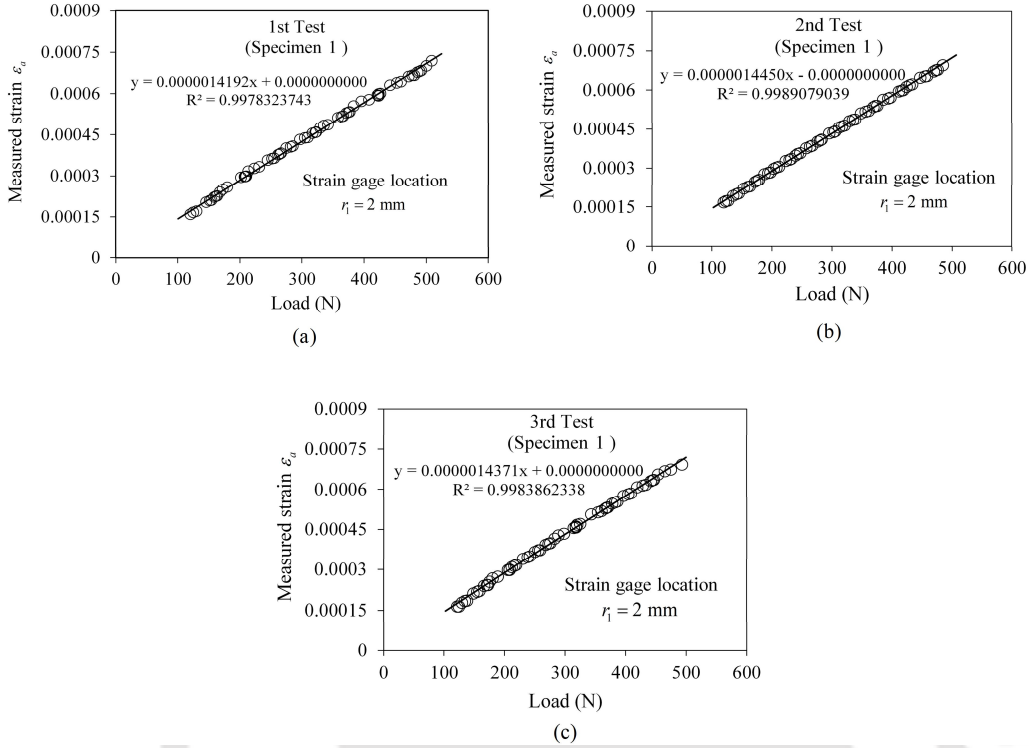

Figure 7.7 Measured strain ε_a at $r_1 = 2$ mm for the specimen 1 of the notch angle $\gamma = 30°$, $a/b = 0.3$ in all three repeated tests.

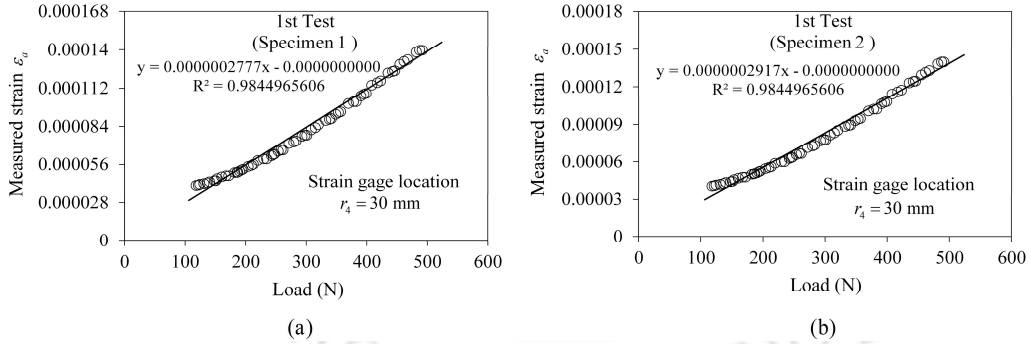

Figure 7.8 Measured strain ε_a at $r_4 = 30$ mm in the first test of the two identical specimens of the notch angle $(\gamma) = 75°$, $a/b = 0.3$.

Table 7.5 shows the measured strains ε_a for the strain gage located at $r_1 = 2$ mm obtained from the best-fit equations of a typical test (1st test of specimen 1 in Fig.7.7(a)) for different values of applied loads for $\gamma = 30°$ and $a/b = 0.3$. The mode I NSIF K_I^V has been computed corresponding to different load values using the measured strain

values (Table 7.5) and average material properties (E and ν shown in Table 6.2 and again in Table 7.2) in Eq. (4.12) and Eq. (4.17). Subsequently, the mode I normalized NSIF F_I is computed using the experimental values of K_I^V by using Eq. (7.7). Table 7.5 also shows these experimental values of K_I^V and F_I for different loads. It could be observed from the Table 7.5 that while K_I^V is increasing with the increase in applied load, F_I remains constant irrespective of the applied load. All these trends are as expected. Similar trends have also been obtained with the strain data of other repeated tests as the slopes of the straight lines in Fig. 7.7 are almost equal.

Table 7.5 Variation of experimental values of K_I^V and F_I at $r_1 = 2$ mm with the applied load in the 1st test of specimen 1 for $\gamma = 30°$ and $a/b = 0.3$

Load (N)	Measured strain ε_a	K_I^V (MPa (mm)$^{1-\lambda_1}$)	F_I
50	0.00007	1.7776	2.2085
100	0.00014	3.5552	2.2085
150	0.00021	5.3327	2.2085
200	0.00028	7.1103	2.2085
250	0.00035	8.8879	2.2085
300	0.00043	10.6655	2.2085
350	0.00050	12.4431	2.2085
400	0.00057	14.2206	2.2085
450	0.00064	15.9982	2.2085
500	0.00071	17.7758	2.2085

Table 7.6 shows the experimental values of F_I for the two identical SENT specimens of the notch angle $\gamma = 30°$, $a/b = 0.3$ at all four selected radial strain gage locations (Table 7.4). Averaged values of F_I of three repeated experiments of each of the two specimens is also presented in Table 7.6 at each gage location. It is interesting to notice from Table 7.6 that the averaged F_I values of the two identical specimens are almost the same at each radial strain gage location, which further substantiates the good reproducibility of the present experimental results. At each radial location (Table 7.6),

F_I values of two identical specimens have been further averaged, and it has been used to find the percentage relative error using the reference solutions presented in Table 7.3.

Table 7.6 Experimental values of F_I for the notch angle $\gamma = 30°$ and $a/b = 0.3$

Location	F_I				% Relative error (Eq.(7.8))
	Specimen-1	Specimen-2	Average ($F_I^{experimental}$)	Reference solution (Table 7.3)	
$r_1 = 2$ mm $(< 0.5t)$	2.1993	2.1895	2.1944		31.84
$r_2 = 5$ mm $(< 1.25t)$	2.0617	2.0704	2.0661		24.12
$r_3 = 15$ mm $(> 1.25t)$	1.6440	1.6394	1.6417	1.6645	1.37
$r_4 = 30$ mm $(> 1.25t)$	1.5695	1.5676	1.5686		5.76

According to Li and Guo [119], and Nakamura and Parks [114], the strain gages located at r_1 and r_2 are in the 3D and 3D-2D transition stress zones, respectively. Therefore, the substitution of the measured strain values at these locations in the expression of Eq. (4.17) (which is based on the plane stress conditions) can be expected to produce large errors in the NSIFs. It is very interesting to notice from the results presented in Table 7.6 that errors in the assessed NSIFs at these locations (r_1 and r_2) are relatively large and non-acceptable. On the other hand, the strain gages at r_3 and r_4 have been located well within the plane stress region according to Li and Guo [119], and Nakamura and Parks [114] and as expected, the percent relative error in the NSIF at these locations is small and acceptable. Indeed, the error at r_3 is much smaller than at r_4.

The results at r_3 and r_4 are acceptable mainly because measured strains and Eq. (4.17) correspond to plane stress conditions. These results clearly corroborate the findings of Li and Guo [119] for the sharp V-notch problems on the location of the plane stress region and also demonstrate the extension of findings of Nakamura and Parks [114] for the sharp V-notch problems. However, it is worth mentioning here that, the error at the location r_4 is larger than that at the location r_3 (Table 7.6). Although r_3

and r_4 are located well within the dominance of plane stress, but r_4 is located at a substantially larger distance from the notch tip than r_3. It is well-known that the dominance of a certain number of Williams' coefficients in the measured strain depends on the location of its measurement. As a result, the measured strains at large distances from the notch tip such as at r_4 would have the dominance of higher-order coefficients than those considered in Eq. (4.14) and as a result higher error in the NSIF as compared with the results at r_3. In contrast, the measured strain at the radial location r_3 is compatible with the Williams' coefficients in Eq. (4.14) and thus provides the NSIF with a small error.

Thus, the above discussion clearly indicates that mere measurement of strains in the plane stress region is not enough; measurements at valid or appropriate locations within the plane stress zone (such as r_3) also influence the error in the measured NSIF. Conversely, $r_{\min}$ is a necessary parameter for conducting valid experiments but not sufficient.

Table 7.7 shows the measured strains ε_a for the strain gage located at $r_4 = 30$ mm obtained from the best-fit equations of another typical test (1st test of specimen 1 in Fig.7.8(a)) for different values of applied loads for $\gamma = 75°$ and $a/b = 0.3$. The mode I NSIF K_I^V and the mode I normalized NSIF F_I have been computed using the same procedure as followed for the previous notched case ($\gamma = 30°$ and $a/b = 0.3$). It could be observed from the Table 7.7 that K_I^V is increasing with the increase in applied load but F_I remains constant irrespective of the applied load. Similar trends have also been obtained with the strain data of other repeated tests as the slopes of the straight lines are almost equal (Fig.7.8).

Table 7.7 Variation of experimental values of K_I^V and F_I at $r_4 = 30$ mm with the applied load in the 1st test of specimen 1 for $\gamma = 75°$ and $a/b = 0.3$

Load (N)	Measured strain ε_a	K_I^V (MPa $(mm)^{1-\lambda_1}$)	F_I
50	0.00001	1.3267	1.7837
100	0.00003	2.6533	1.7837
150	0.00004	3.9800	1.7837
200	0.00006	5.3067	1.7837
250	0.00007	6.6334	1.7837
300	0.00008	7.9601	1.7837
350	0.00010	9.2868	1.7837
400	0.00011	10.6134	1.7837
450	0.00012	11.9401	1.7837
500	0.00014	13.2668	1.7837

Table 7.8 presents the experimental results of the SENT specimen with $\gamma = 75°$ and $a/b = 0.3$. Here again, averaged values of F_I of three repeated experiments of each of the two specimens are presented in Table 7.8 at each gage location. As can be noticed from the table (Table 7.8), F_I values of two identical specimens of this configuration are almost the same at each radial gage location, which again validates the good reproducibility of the present experimental results. Like in the previous notched case, averaged values of F_I have been employed in the calculation of the percent relative error as shown in Table 7.8. Here again, one can notice large errors in the NSIFs have been obtained at the radial locations r_1 and r_2 as they are located in the 3D and 3D-2D transition regions, respectively. This indicates that the measured strains at r_1 and r_2 are in the 3D and 3D-2D transition regions and hence not compatible with the state of stress employed in Eq. (4.17). As expected, the error at r_1 is higher in comparison with the error at r_2 due to its location in the 3D stress-strain state.

Table 7.8 Experimental values of F_I for the notch angle $\gamma = 75°$ and $a/b = 0.3$

Location	F_I				% Relative error
	Specimen-1	Specimen-2	Average	Reference solution (Table 7.3)	
$r_1 = 2$ mm $(< 0.5t)$	2.5631	2.5793	2.5712	1.8254	40.86
$r_2 = 5$ mm $(< 1.25t)$	2.2859	2.2812	2.2836		25.10
$r_3 = 15$ mm $(> 1.25t)$	1.8013	1.8026	1.8020		1.28
$r_4 = 30$ mm $(> 1.25t)$	1.7895	1.7899	1.7897		1.96

Similar to the previous notched configuration ($\gamma = 30°$ and $a/b = 0.3$), it can be noticed from Table 7.8 that the percentage relative error at r_3 and r_4 are very small as compared with the locations at r_1 and r_2. This is mainly because both the r_3 and r_4 are located in the plane stress region and Eq. (4.17) is derived using the plane stress conditions. Clearly, these results once again strongly substantiate the findings of Li and Guo [119], and Nakamura and Parks [114]. It is interesting to notice from the results of Table 7.8 that the errors at the locations r_3 and r_4 are less than 2% and hence are acceptable errors. Furthermore, the error at r_4 in this configuration is much smaller than that in the configuration with $\gamma = 30°$ and $a/b = 0.3$. This is mainly because (a) both the r_3 and r_4 radial positions of the notch angle $\gamma = 75°$ and $a/b = 0.3$ are located in the plane stress region and (b) the measured strains at these locations are primarily dominated by the Williams' coefficients A_1, A_2 and A_2^* as in Eq. (4.17). Similar to the case of $\gamma = 30°$ and $a/b = 0.3$, the error is minimal at the location r_3 for this configuration as well (Table 7.8).

The results presented in Tables 7.6 and 7.8 strongly validate the findings of Li and Guo [119] for the sharp V-notch problems and also demonstrate the extension of the use of the findings of Nakamura and Parks [114] for the sharp V-notch problems. Furthermore, the present results also clearly recommend considering $r_{min} = 1.5t$ [114] as the more sound, highly dependable and definitive value as compared with the

$r_{min} = 1.25t$ [119] without loss of generality for identification of plane stress zone ahead of a sharp V-notch tip.

Results at the radial location r_4 in Tables 7.6 and 7.8, demonstrate that not only the r_{min} parameter is important for the accurate assessment of the field variables (and NSIFs) of the sharp V-notch problems but also the maximum permissible radial distance (r_{max}) within the plane stress zone. This needs to be decided based on the number of non-singular Williams' coefficients employed in the strain expression. Thus, the present results demonstrate the importance of the maximum permissible radial distance of a strain gage r_{max}. Next chapter investigates the accuracy of the measured NSIFs by considering both the r_{min} and r_{max} values (and hence the valid gage locations).

7.4 Summary

This chapter substantiates the value of r_{min} i.e., the minimum radial distance for locating the strain gage. It includes the numerical and experimental verification of the extent of the 3D stress-strain field, 3D-2D transition zone and plane stress zone ahead of the tip of a sharp V-notch given by Li and Guo [119]. This chapter shows that a strain gage needs to be placed at a minimum radial distance of r_{min} from the notch tip for accurate sampling of the 2D field variables. It has been shown that the NSIFs can be highly erroneous (as high as 40%) if a gage is located below r_{min} value. The study summarizes that valid radial locations play a vital role in the determination of accurate NSIFs. Based on the presented experimental results, it has been recommended to consider $r_{min} = 1.5t$ [114] formulated by Nakamura and Parks as a more reliable value than the $r_{min} = 1.25t$ [119] without loss of generality for identification of plane stress zone ahead of a sharp V-notch tip.

Chapter 8

Experimental validation of the proposed technique with the valid gage locations

This chapter is focused on the experimental investigation on the efficacy of the proposed single strain gage technique which comes along with the valid gage locations presented in Chapter 4 for the accurate determination of the mode I NSIFs. Experiments have been conducted on several mode I sharp V-notched configurations as explained in Chapter 6. It has been shown that these valid locations are governed by two parameters r_{min} and r_{max} of a sharp V-notched configuration. The previous chapter validated the minimum allowable strain gage radial location r_{min}.

8.1 Description of the test procedure

In the present work, numerous mode I experiments have been conducted on a single-edge notch tensile (SENT) specimen and a semi-circular bend (SCB) specimen, as shown schematically in Figs.8.1 and 8.2, respectively. These figures have been reproduced here for the convenience. Different notch angles and a / b ratios have been considered for testing in the present investigation.

Table 8.1 and Table 8.2 show the geometrical data and the material properties of the SENT and SCB specimens, respectively. The elastic properties of the selected material (PMMA) have been found as Young's modulus $E = 3.207$ GPa and Poisson's ratio $\nu = 0.381$ (section 6.3). As the plate thickness $t = 6$ mm is small compared to other dimensions of both specimens, it is assumed that the specimens are under plane stress conditions except in the vicinity of the notch tip [114, 119].

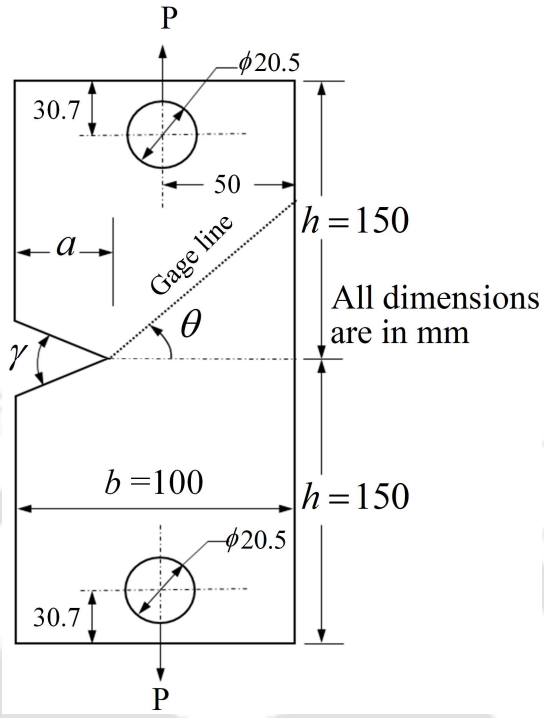

Figure 8.1 Schematic diagram of the SENT experimental specimen subjected to mode I loading.

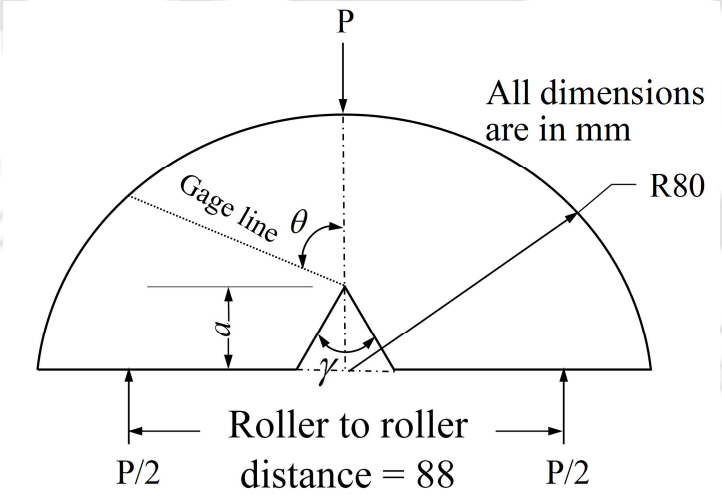

Figure 8.2 Schematic diagram of the three-point sharp V-notched SCB experimental specimen subjected to mode I loading.

Table 8.1 Material properties and geometrical data of the SENT specimens

Description	Value
Width, b	100 mm
Height, $2h$	300 mm
Plate thickness, t	6 mm
Notch angle, γ	$20°, 30°$
Notch length to width ratio, a/b	0.4, 0.6
Young's modulus, E	3.207 GPa
Poisson's ratio, ν	0.381

Table 8.2 Material properties and geometrical data of the SCB specimens

Description	Value
Radius, R	80 mm
Roller diameter, ϕ	25 mm
Centre-to-roller distance	44 mm
Plate thickness, t	6 mm
Notch angle, γ	$35°, 60°$
Notch length to radius ratio, a/R	0.3
Young's modulus, E	3.207 GPa
Poisson's ratio, ν	0.381

The SENT specimens with the notch angles $\gamma = 20°$ and $\gamma = 30°$ have been considered for the experiments, and for each notch angle, two notch length to plate width ratios $a/b = 0.4$ and $a/b = 0.6$ have been tested. On the other hand, the SCB specimens with two notch angles $\gamma = 35°$ and $\gamma = 60°$ have been tested for notch length to plate radius ratio $a/R = 0.3$. Two identical SENT specimens for $\gamma = 20°$, $a/b = 0.4$ and $\gamma = 30°$, $a/b = 0.4$ have also been tested to ascertain the reproducibility of the experimental results. Also, two identical SCB ($\gamma = 35°, a/R = 0.3$) specimens have been tested. Further, all the specimens (both the SENT and SCB) have been tested three times to

observe the repeatability of the results. Thus, a total of 18 and 9 experiments have been conducted on the SENT and SCB configurations respectively. All the specimens have been cut using the same 2.5 kW CO_2 laser cutting machine as discussed in section 6.2, and the V-notches have been further sharpened (Fig.6.2) using a razor blade to make sharp tips. As stated earlier, after the fabrication of the SENT specimens, a/b ratios were found to vary in the range of 0.37 to 0.43 instead of 0.4 and in the range of 0.55 to 0.64 instead of 0.6. As these variations are practically trivial compared to the intended values of 0.4 and 0.6, results have been reported with a/b ratios 0.4 and 0.6 in the presented investigation.

A closed-loop servo hydraulic INSTRON 8801 machine with a capacity of 100 kN has been used to load all the specimens under displacement control mode with an actuator speed of 0.25 mm/min. A 25 kN load cell has been employed in the INSTRON 100 kN machine in all experiments of the present work to measure the applied load. Strain gages (Type: FLA-1-11-3LT and Make: TML Japan) with 1 mm gage length and 350 Ω resistance have been pasted on the specimens. As shown by Dally and Sanford [36], the effect of strain gradients on the strain measurements can be minimized by employing strain gages with small gage lengths. Strain gages have been positioned at different radii (along the gage line) from the notch tip including both the valid and invalid radial locations to demonstrate the efficacy of the proposed strain gage technique. A LabVIEW-supported experimental setup comprising NI data acquisition system as described in Chapter 6 has been employed. The complete experimental setup of the presented investigation is shown in Fig.6.13.

After determining the mode I NSIF K_I^V using the measured strains and Eq. (4.12) and Eq. (4.17), the normalized mode I NSIF F_I is obtained using Eq. (7.7) in section 7.3.1. Then, the % relative error in measured F_I is computed using Eq. (7.8) as shown in section 7.3.1. In this experimental investigation, the reference solutions in Eq. (7.8) for the SENT and SCB specimens as per the geometric dimensions given in Table 8.1 and Table 8.2 have been computed using the point substitution technique developed by Hussain and Murthy [54]. Finite element computation of the reference solutions of NSIFs for SENT and SCB specimens have been presented in the next section (section 8.2).

8.2 Numerical evaluation of the reference NSIFs and r_{max} of the experimental specimens

Here, 2D finite element analysis using commercial software ANSYS® is employed to estimate r_{max} values and the reference solutions of mode I NSIFs for the selected SENT and SCB specimens. Following the theoretical procedure discussed in section 4.2, r_{max} values of the experimental specimens have been computed for different notch parameters. As the procedure for the computation of r_{max} for any V-notched configuration is discussed and demonstrated in detail in Chapters 4 and 5, therefore no in-depth details are presented here for the computation of the same for the experimental specimens of this chapter.

Figures 8.3 (a) and (b) show a typical finite element mesh with a number of elements (NE) and a number of nodes (NN) considered for the SENT and SCB configurations for the computation of the reference NSIFs and r_{max} values. Due to the symmetry of the experimental specimens, only one-half of the specimen in each case has been analysed with the symmetric boundary conditions as shown in Fig.8.3. The region around the notch tip has been meshed with the collapsed eight-nodded isoparametric quadrilateral elements (Q8) in a typical spider web pattern, and the conventional quadrilateral elements (Q8) have been introduced everywhere. In the mesh convergence study for the SENT specimens, three meshes of different densities have been considered viz., mesh 1(NN=3397, NE=1076), mesh 2(NN=10561, NE=3418) and mesh 3 (NN=23356, NE=7631). Similarly, three meshes of different densities have been considered for the SCB specimens viz., mesh 1(NN=5197, NE=1669), mesh 2(NN=11586, NE=3768) and mesh 3 (NN=28819, NE=9459).

In each of the above two specimens, mesh 3 represents the finest mesh. The r_{max} value corresponding to mesh 3 is employed for determination of the valid strain gage locations during experiments, while the reference NSIF corresponding to mesh 3 is employed for % relative error estimation of the experimental NSIFs. Tables 8.3 and 8.4 show the convergence of the computed reference normalized NSIFs of the SENT and SCB specimens, respectively. A very good convergence of the NSIFs can be noticed in

the above tables. Tables 8.3 and 8.4 also show final converged values of the corresponding r_{max} values of each specimen obtained using mesh 3.

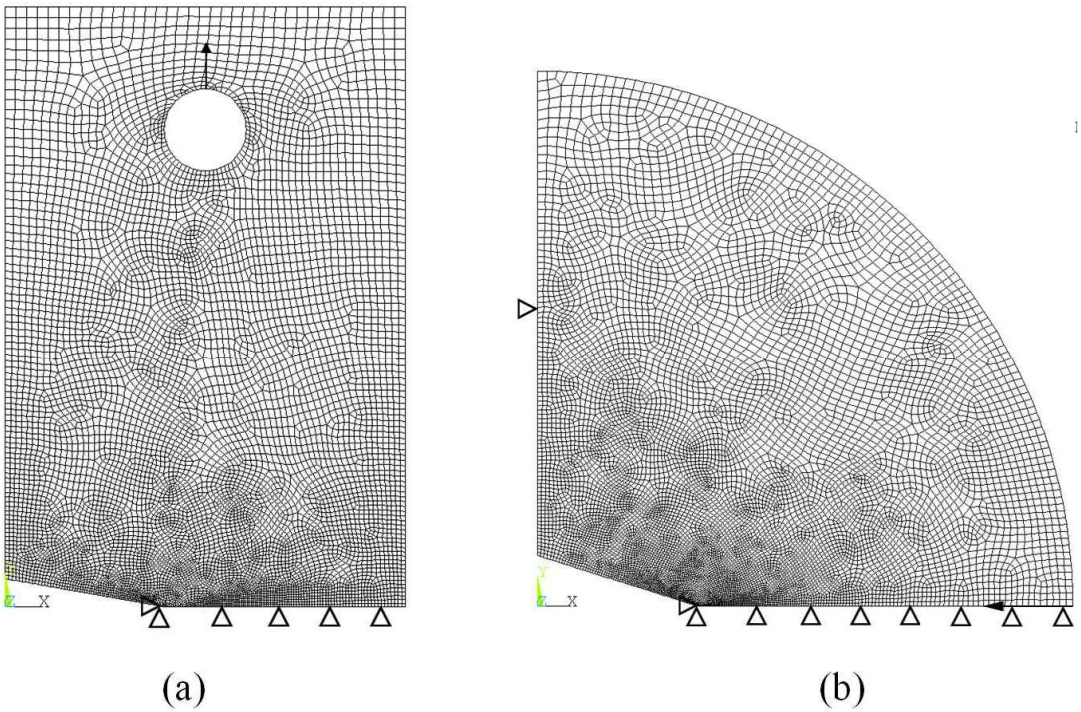

Figure 8.3 (a) Typical finite element mesh used for the SENT configuration with $\gamma = 20°, a/b = 0.4$ (NE=7631, NN=23356); (b) Typical finite element mesh used for three-point sharp V-notched SCB configuration with $\gamma = 35°, a/R = 0.3$ (NE=9459, NN=28819).

Table 8.3 Convergence of reference values of the NSIFs of the SENT specimens

γ	a/b	Mesh1	Mesh2	Mesh3	r_{max}
		F_I	F_I	F_I*	(mm)
20°	0.4	2.0927	2.0923	2.0921	25.26
	0.6	4.0044	3.9925	3.9824	20.25
30°	0.4	2.1101	2.1097	2.1084	69.97
	0.6	4.0344	4.0174	4.0088	38.21

* NSIF employed for error estimation of experimental NSIFs

Table 8.4 Convergence of reference values of the NSIFs of the SCB specimens

γ	a/R	Mesh1	Mesh2	Mesh3	r_{max}
		F_I	F_I	F_I *	(mm)
35°	0.3	1.4976	1.5197	1.5243	55.62
60°	0.3	2.0891	2.1189	2.1273	53.38

* NSIF employed for error estimation of experimental NSIFs

8.3 Experimental results and discussion

This section presents the experimentally obtained NSIFs using different strain gages located at different radial locations for the selected SENT and SCB specimens. As stated earlier, strain gages are located at valid (Eq. (4.21)) and invalid locations intentionally to understand the significance of r_{min} and r_{max}. According to Eq. (4.21), a valid gage location (r) is one which satisfies the equation $r_{min} \le r \le r_{max}$. Unacceptable results of the NSIFs (due to 3D and 3D-2D transition effects) obtained from strain gages placed below the value of r_{min} was discussed in detail in Chapter 7 and hence gages have not been placed below the r_{min} value in this chapter. Conversely, all strain gages of the present chapter have been pasted beyond r_{min} of the specimens and hence located in the plane stress dominated regions. The efficacy of the proposed strain gage technique with the valid gage locations has been studied using the percentage relative error in the measured NSIFs.

8.3.1 Experimental results for the SENT specimens

Figure 8.4 shows the selected SENT specimens made using PMMA material as per the dimensions mentioned in Table 8.1 with strain gages pasted along the respective gage lines. Table 8.5 shows selected radial gage locations which consists of both the valid and invalid locations (Eq. (4.21)). As explained earlier, gage locations above r_{max} are invalid and locations that obey Eq. (4.21) are valid locations. Table 8.5 also shows the computed values of r_{max}, θ and β (Eq. (4.15)) for each of the selected specimens following the procedure described in Chapter 4. It is to be noted here that the value of

β is dependent only on the Poisson's ratio and the notch angle γ. As mentioned earlier, each of the SENT specimens has been tested three times to examine the repeatability of the results. Also, two identical specimens of the SENT geometry with $\gamma = 20°$, $a/b = 0.4$ and $\gamma = 30°$, $a/b = 0.4$ have been tested to substantiate the reproducibility of the results.

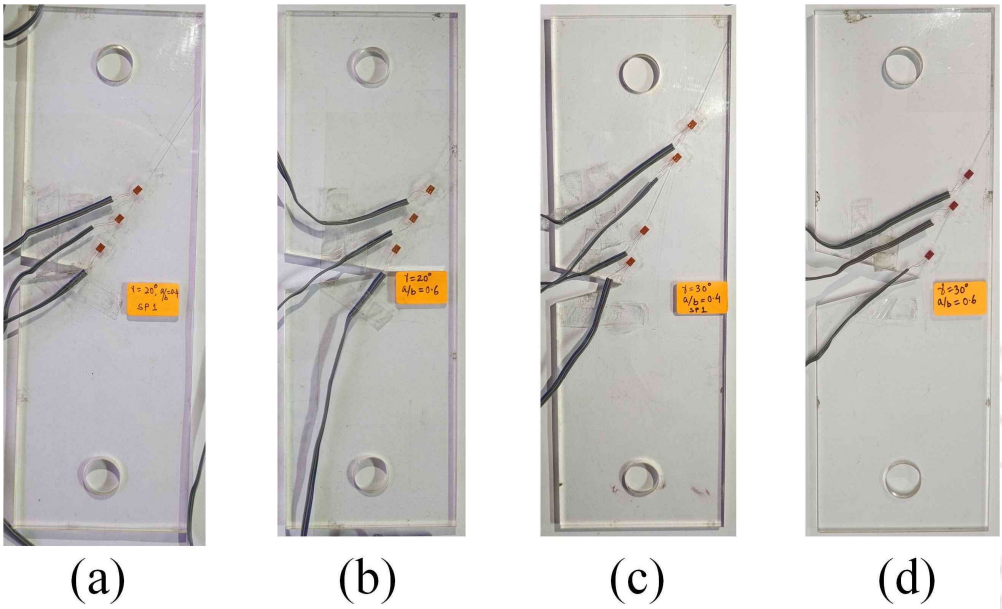

Figure 8.4 SENT specimens employed in the experiments (a) $\gamma = 20°, a/b = 0.4$; (b) $\gamma = 20°, a/b = 0.6$; (c) $\gamma = 30°, a/b = 0.4$; (d) $\gamma = 30°, a/b = 0.6$.

Table 8.5 Selected strain gage radial locations for the SENT configurations ($t = 6$ mm, $r_{min} = 1.5t = 9$ mm)

γ	a/b	r_1(mm)	r_2(mm)	r_3(mm)	r_4(mm)	r_{max}(mm)	$\theta°$	$\beta°$
20°	0.4	15	35	55	-	25.26	60	52.58
	0.6	15	35	55	-	20.25	60	52.58
30°	0.4	15	35	80	100	68.97	65	49.24
	0.6	15	45	65	-	38.21	65	49.24

As can be seen from Table 8.5 for $\gamma = 20°$, the radial location r_1 is valid whereas the radial locations r_2 and r_3 are invalid as they are beyond the values of the corresponding

r_{max}. Similarly, for $\gamma = 30°$ and $a/b = 0.4$, both the r_1 and r_2 locations are valid locations, whereas r_3 and r_4 are invalid strain gage locations. However, for $\gamma = 30°$ and $a/b = 0.6$, again r_1 is a valid location, r_2 and r_3 are invalid locations. These radii are arbitrarily selected to demonstrate the validity of proposed Eq. (4.21). Further, it can also be noticed from Table 8.5 that the smallest valid radial distance $r_1 = 15$ mm is at a considerable distance from the sharp V-notch tip. As can be noticed from Table 8.5 that all strain gages have been pasted in the plane stress region as all their radial distances are greater than 1.5 times the thickness of the plate (see section 7.3).

According to the proposed technique, it can be anticipated that the percentage relative errors in the experimentally measured normalized NSIF, F_I would be within the acceptable limit at valid radial locations as they satisfy Eq. (4.21). On the other hand, unacceptable or highly erroneous measured F_I values can be expected at the invalid radial locations. This is because, at such large distances, Eq. (4.21) may not hold appropriately due to the dominance of additional Williams' coefficients of higher order than those selected in Eq. (4.14), although the gages are well within the plane stress dominated zone.

Here, the results corresponding to $\gamma = 20°$ have been presented first, followed by $\gamma = 30°$. Figure 8.5 represents the foot-corrected plots of measured raw strain ε_a data (encircled data points) versus the applied load at $r_1 = 15$ mm corresponding to the first test of the two identical SENT specimens of $\gamma = 20°$ and $a/b = 0.4$. Figure 8.6, on the other hand, shows the plots of measured raw strain ε_a at $r_3 = 55$ mm versus the applied load for three repeated tests of the SENT specimen with $\gamma = 20°$ and $a/b = 0.6$. Figures 8.5 and 8.6 also show the best-fit straight lines (solid lines) with the associated slopes and the statistical coefficient R^2 of the fit. In all the plots in Figs.8.5 and 8.6, the value of R^2 is very close to unity, thus indicating a very good linear relationship between the measured strains and the applied loads. In addition, as expected, the slopes of the best-fit lines in Fig.8.5 are almost the same indicating the goodness of the calibration and repeatability of the presented experiments. A similar trend can also be observed in Fig.8.6.

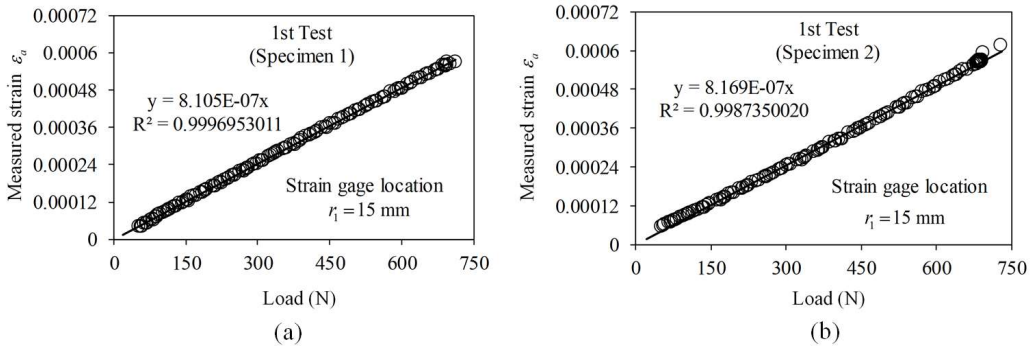

Figure 8.5 Measured strain ε_a at $r_1 = 15$ mm in the first test of the two identical SENT specimens with $\gamma = 20°$, $a/b = 0.4$.

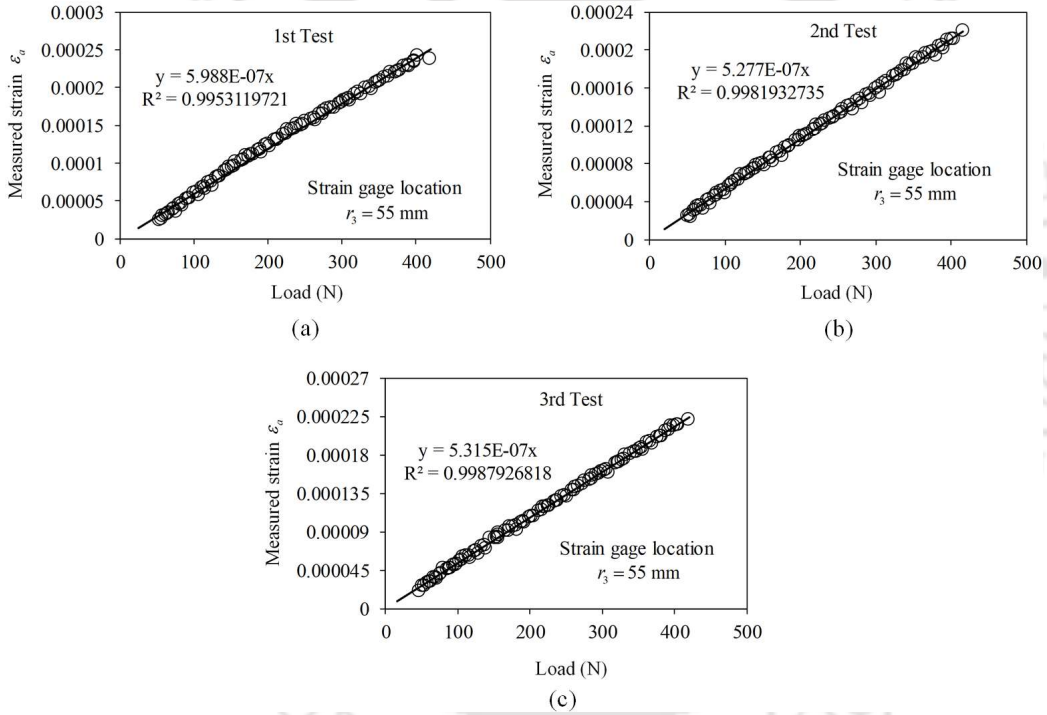

Figure 8.6 Measured strain ε_a at $r_3 = 55$ mm in three repeated tests of the SENT specimen with $\gamma = 20°$, $a/b = 0.6$.

Similarly, Fig.8.7 shows the plots of the measured raw strain ε_a versus the applied loads at $r_1 = 15$ mm in the first test of the two identical specimens of $\gamma = 30°$, $a/b = 0.4$, whereas Fig.8.8 presents plots of ε_a versus the applied loads at $r_3 = 65$ mm for three repeated tests of the SENT specimen with $\gamma = 30°$, $a/b = 0.6$. The graphical trends of

Fig.8.7 and Fig.8.8 are similar to those of Fig.8.5 and Fig.8.6 indicating once again the goodness of the calibration and repeatability of the present experiments. Similar trends have also been observed at all other strain gage locations.

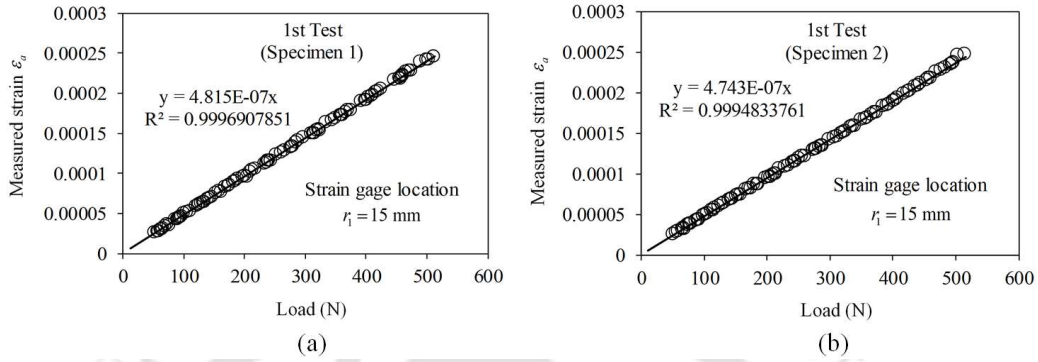

Figure 8.7 Measured strain ε_a at $r_1 = 15$ mm in the first test of the two identical SENT specimens with $\gamma = 30°$, $a/b = 0.4$.

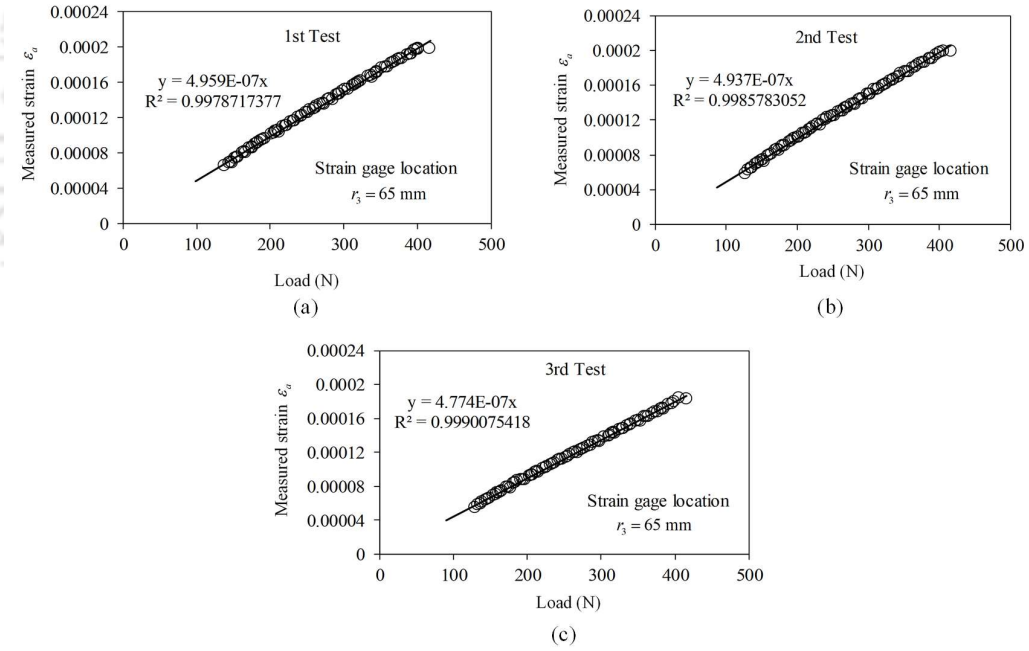

Figure 8.8 Measured strain ε_a at $r_3 = 65$ mm in three repeated tests of the SENT specimen with $\gamma = 30°$, $a/b = 0.6$.

Table 8.6 shows the measured strains ε_a for the strain gage located at $r_1 = 15$ mm obtained from the best-fit equations in Fig.8.5(a) ($\gamma = 20°$ and $a/b = 0.4$) for different

values of applied loads. The mode I NSIF K_I^V and the mode I normalized NSIF F_I have been computed using the same procedure as followed in Chapter 7 (Eqs. (4.12) and (4.17)). It could be observed from Table 8.6 that K_I^V is increasing with the increase in applied load but F_I remains constant irrespective of the applied load as expected. Similar trends have been obtained with the strain data of other repeated tests as well.

Table 8.6 Variation of experimental values of K_I^V and F_I at $r_1 = 15$ mm with the applied load in the 1st test of 1st specimen for $\gamma = 20°$ and $a/b = 0.4$

Load (N)	Measured strain ε_a	K_I^V (MPa $(mm)^{1-\lambda_1}$)	F_I
50	0.0000405	1.9956	2.1396
100	0.0000811	3.9912	2.1396
150	0.0001216	5.9868	2.1396
200	0.0001621	7.9824	2.1396
250	0.0002026	9.9779	2.1396
300	0.0002432	11.9735	2.1396
350	0.0002837	13.9691	2.1396
400	0.0003242	15.9647	2.1396
450	0.0003647	17.9603	2.1396
500	0.0004053	19.9559	2.1396

Table 8.7 shows the experimental values of F_I corresponding to two identical SENT specimens with the notch angle $\gamma = 20°$, $a/b = 0.4$ at all three selected radial strain gage locations (Table 8.5). In Table 8.7, the value of F_I at each radial gage location is the average value from three repeated experiments of each of the two identical specimens. It can be seen from Table 8.7 that the measured F_I values of two identical specimens are almost the same at each strain gage location, which clearly substantiates the good reproducibility of the present experimental results. F_I values of these two identical specimens (Table 8.7) have been further averaged at each radial location and subsequently, the percentage relative error in measured F_I (Eq. (7.8)) has been

obtained at each radial location using the reference solutions based on finite element analyses (Table 8.3). Table 8.7 also shows these errors.

Table 8.7 Experimental values of F_I at valid and invalid locations for the two identical SENT specimens with $\gamma = 20°$, $a/b = 0.4$ and $r_{max} = 25.26$ mm

Location	F_I				% Relative Error
	1st specimen	2nd specimen	Average	Reference solution (Table 8.3)	
Valid $(r_1 = 15\text{ mm} < r_{max})$	2.0769	2.0145	2.0457	2.0921	2.21
Invalid $(r_2 = 35\text{ mm} > r_{max})$	1.7931	1.7125	1.7528		16.22
Invalid $(r_3 = 55\text{ mm} > r_{max})$	1.4741	1.4458	1.4599		30.22

It is interesting to observe from the results in Table 8.7 that very accurate F_I values with a relative error of 2.21% is measured by the strain gage located at the valid location r_1 although it is not located near the notch tip. On the other hand, highly unacceptable F_I values (error > 5%) have been measured by the strain gages located at both the invalid locations (r_2 and r_3) to such an extent that the percentage relative error attains as high as 30%. As mentioned earlier, this large error at invalid locations i.e., radial locations greater than r_{max} is mainly due to the dominance of higher-order Williams' coefficients other than those considered in Eq. (4.14) in the measured strain. The results in Table 8.7 clearly substantiate excellent capability for the accurate determination of mode I NSIFs of a sharp V-notched configuration by the proposed single strain gage technique with the valid gage locations. Further results also show the importance of valid gage locations and knowing r_{min} and r_{max} values of a sharp V-notched configuration *a priori*.

Table 8.8 shows the measured strains ε_a for the strain gage located at $r_3 = 55$ mm obtained from the best-fit equations of another typical test (1st test of the experimental specimen in Fig.8.6(a)) for different values of applied loads for $\gamma = 20°$

and $a/b=0.6$. It could be observed from Table 8.8 that K_I^V is increasing with the increase in applied load but F_I remains constant irrespective of the applied load as expected. Similar trends have been obtained with the strain data of other repeated tests as well.

Table 8.8 Variation of experimental values of K_I^V and F_I at $r_3=55$ mm with the applied load in the 1st test of the experimental specimen for $\gamma=20°$ and $a/b=0.6$

Load (N)	Measured strain ε_a	K_I^V (MPa (mm)$^{1-\lambda_1}$)	F_I
50	0.0000299	2.7037	2.8988
100	0.0000599	5.4075	2.8988
150	0.0000898	8.1112	2.8988
200	0.0001198	10.8149	2.8988
250	0.0001497	13.5186	2.8988
300	0.0001796	16.2224	2.8988
350	0.0002096	18.9261	2.8988
400	0.0002395	21.6298	2.8988
450	0.0002695	24.3336	2.8988
500	0.0002994	27.0373	2.8988

Table 8.9 shows the measured strains ε_a at $r_1=15$ mm obtained from the best-fit equations corresponding to Fig.8.7(a) for different values of applied loads for $\gamma=30°$ and $a/b=0.4$. Moreover, Table 8.10 shows the measured strains ε_a at $r_3=65$ mm obtained from the best-fit equations corresponding to test in Fig.8.8(a) for different values of applied loads for $\gamma=30°$ and $a/b=0.6$. In each of the above cases, the mode I NSIF K_I^V and the mode I normalized NSIF F_I have been computed according to Eq. (4.12) and Eq. (7.7) as discussed in Chapter 7. From both the Tables 8.9 and 8.10, the increasing trend of K_I^V with the increase in applied load could be observed again similar to previous cases but F_I remains constant irrespective of the applied load. Similar trends have been obtained with the strain data of other repeated tests as well.

Table 8.9 Variation of experimental values of K_I^V and F_I at $r_1 = 15$ mm with the applied load in the 1st test of the 1st specimen for $\gamma = 30°$ and $a/b = 0.4$

Load (N)	Measured strain ε_a	K_I^V (MPa $(mm)^{1-\lambda_1}$)	F_I
50	0.0000241	2.0141	2.1676
100	0.0000482	4.0281	2.1676
150	0.0000722	6.0422	2.1676
200	0.0000963	8.0562	2.1676
250	0.0001204	10.0703	2.1676
300	0.0001445	12.0844	2.1676
350	0.0001685	14.0984	2.1676
400	0.0001926	16.1125	2.1676
450	0.0002167	18.1265	2.1676
500	0.0002408	20.1406	2.1676

Table 8.10 Variation of experimental values of K_I^V and F_I at $r_3 = 65$ mm with the applied load in the 1st test of the experimental specimen for $\gamma = 30°$ and $a/b = 0.6$

Load (N)	Measured strain ε_a	K_I^V (MPa $(mm)^{1-\lambda_1}$)	F_I
50	0.0000248	3.0687	2.6981
100	0.0000496	6.1373	2.6981
150	0.0000744	9.2060	2.6981
200	0.0000992	12.2746	2.6981
250	0.0001240	15.3433	2.6981
300	0.0001488	18.4119	2.6981
350	0.0001736	21.4806	2.6981
400	0.0001984	24.5492	2.6981
450	0.0002232	27.6179	2.6981
500	0.0002480	30.6865	2.6981

Table 8.11 presents the results of $\gamma = 20°$ and $a/b = 0.6$, while Table 8.12 presents the results of the two identical SENT specimens of $\gamma = 30°$ and $a/b = 0.4$, and Table 8.13 shows the results of $\gamma = 30°$ and $a/b = 0.6$. It is worth recalling here that only for $a/b = 0.4$ two identical specimens have been tested and only one specimen has been tested for $a/b = 0.6$ for each γ. The results presented in Tables 8.11-8.13 show interesting and strikingly similar trends to those presented in Table 8.7. Again, very accurate mode I NSIFs have been obtained from the strain gage readings located at valid location i.e., at r_1 irrespective of the notch angle and a/b ratio. At all these valid locations, F_I is obtained with relative error less than 5% and the lowest error being 1.93%. It can be seen from Table 8.12 that the measured F_I values of two identical specimens are again almost the same at each strain gage location indicating very good reproducibility of the experiments.

Even more interestingly, referring to Table 8.12, although the second valid radial location $r_2 = 35$ mm is substantially away from the notch tip, nevertheless the error in F_I is less than 5%. An intriguing result is that in Tables 8.7 and 8.11, $r_2 = 35$ mm is an invalid location, and hence the error in F_I is very large, while in Table 8.12 the same radial distance being a valid location, the error is very small as expected. This observation once again indicates the importance of the concept of the r_{max} proposed in this thesis work. As predicted, F_I is measured with a large and unacceptable error by all the gages located at the invalid radial locations in Tables 8.11-8.13. Again, the reason for such a larger error at these locations can be attributed to the presence of the additional higher-order Williams' coefficients than in Eq. (4.14). It is worth mentioning here that the amount of error at invalid locations strongly depends on the given configuration. The aforementioned results clearly indicate r_{min} and r_{max} are the key parameters for achieving the accurate values of mode I NSIFs. Further, the above results also clearly demonstrate the excellent performance of the single strain gage technique proposed in this thesis.

Table 8.11 Experimental values of F_I at valid and invalid locations for the SENT specimens with $\gamma = 20°$, $a/b = 0.6$ and $r_{max} = 20.25$ mm

Location	F_I		% Relative Error
	Reference solution (Table 8.3)	Experimental value	
Valid $(r_1 = 15\text{ mm} < r_{max})$	3.9824	4.0591	1.93 %
Invalid $(r_2 = 35\text{ mm} > r_{max})$		3.2719	17.84%
Invalid $(r_3 = 55\text{ mm} > r_{max})$		2.8027	29.62%

Table 8.12 Experimental values of F_I at valid and invalid locations for the SENT specimens with $\gamma = 30°$, $a/b = 0.4$ and $r_{max} = 68.97$ mm

Location	F_I				% Relative Error
	1st specimen	2nd specimen	Average	Reference solution (Table 8.3)	
Valid $(r_1 = 15\text{ mm} < r_{max})$	2.1704	2.1566	2.1635	2.1084	2.61
Valid $(r_2 = 35\text{ mm} < r_{max})$	2.0151	2.0150	2.0150		4.43
Invalid $(r_3 = 80\text{ mm} > r_{max})$	1.8080	1.8187	1.8134		13.99
Invalid $(r_4 = 100\text{ mm} > r_{max})$	1.6371	1.6019	1.6195		23.19

Table 8.13 Experimental values of F_I at valid and invalid locations for the SENT specimens with $\gamma = 30°$, $a/b = 0.6$ and $r_{max} = 38.21$ mm

Location	F_I		% Relative Error
	Reference solution (Table 8.3)	Experimental value	
Valid $(r_1 = 15\text{ mm} < r_{max})$	4.0088	4.1730	4.10
Invalid $(r_2 = 45\text{ mm} > r_{max})$		3.3376	16.74
Invalid $(r_3 = 65\text{ mm} > r_{max})$		2.7914	30.37

8.3.2 Experimental results for the SCB configurations

Another geometry considered in this investigation is the three-point semi-circular bend (SCB) specimen with a sharp V-notch. Fig.8.9 displays the images of the selected specimens made of PMMA material, as detailed in Table 8.2. Again, two identical specimens of the SCB with $\gamma = 35°$, $a/R = 0.3$ have also been tested to substantiate the reproducibility of the results. Further, each specimen has been tested three times. Thus, a total of nine experiments have been conducted on the SCB specimen. Fig.8.10 shows a sharp V-notched SCB specimen mounting on a three-point bend setup. As stated earlier, all the specimens have been loaded under displacement control with an actuator speed of 0.25 mm/min.

(a) (b)

Figure 8.9 Three-point sharp V-notched SCB specimens employed in the experiments (a) $\gamma = 35°, a/R = 0.3$; (b) $\gamma = 60°, a/R = 0.3$.

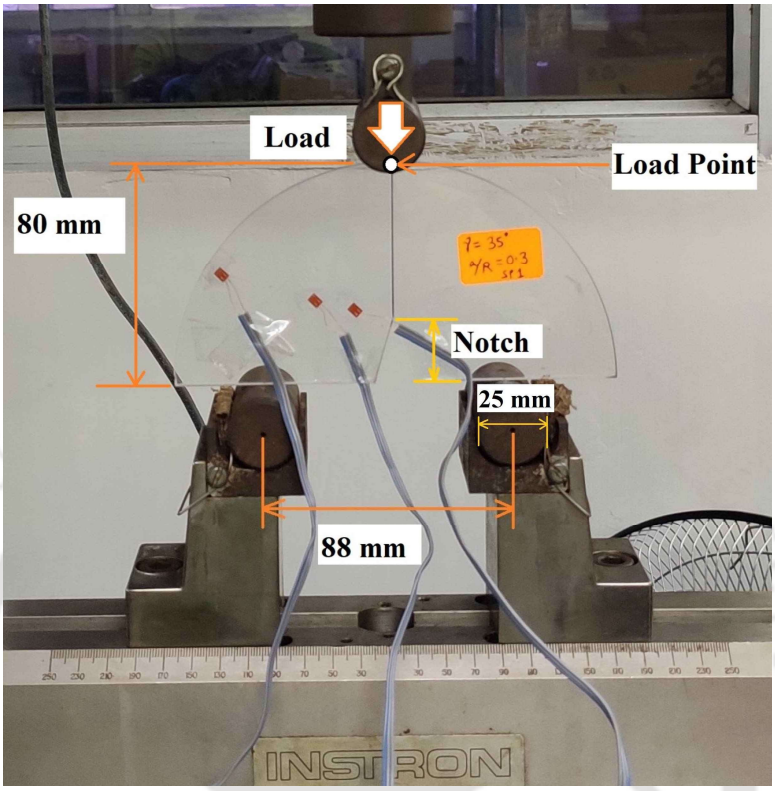

Figure 8.10 The SCB specimen mounted on the three-point bend setup.

Each SCB specimen (Fig.8.9) has been tested with multiple strain gages placed at different radial locations away from the notch tip. Table 8.14 shows the selected radial gage locations, which consist of both the valid and invalid locations, as in the case of the SENT specimen. Table 8.14 also shows the computed values of r_{max}, θ and β for each of the selected specimens following the procedure described in Chapter 4. It should be noted that here also the values of θ and β are dependent only on the Poisson's ratio ν and the notch angle γ.

Table 8.14 Selected strain gage radial locations for the SCB configurations ($t = 6$ mm, $r_{min} = 1.5t = 9$ mm)

γ	a / R	r_1(mm)	r_2(mm)	r_3(mm)	r_{max}(mm)	$\theta°$	$\beta°$
35°	0.3	15	30	65	55.62	75	46.83
60°	0.3	15	30	60	53.38	44.67	44.32

As can be noticed from Table 8.14, all strain gages have been pasted in the plane stress region as all their radial distances are greater than 1.5 times the thickness of the plate. For both the notch angles $\gamma = 35°$ and $60°$, both the radial locations r_1 and r_2 are the valid locations whereas the radial location r_3 is intentionally selected to be an invalid location as it is beyond the values of r_{max}. Further, it can also be noticed from Table 8.14 that the smallest valid radial distance $r_1 = 15$ mm is at a considerable distance from the sharp V-notch tip, as in the case of the SENT specimen (section 8.3.1).

Fig.8.11 represents the foot-corrected plots of measured raw strain ε_a versus the applied load at $r_2 = 30$ mm corresponding to the first test of two identical sharp V-notched SCB specimens of $\gamma = 35°$, $a / R = 0.3$ for substantiation of the reproducibility of results. Fig.8.12, on the other hand, shows the plots of measured raw strain ε_a data versus the applied load at $r_3 = 60$ mm for three repeated tests of the SCB specimen of $\gamma = 60°, a / R = 0.3$. Figs.8.11 and 8.12 also show the best-fit straight lines with the associated slopes and the statistical coefficient R^2. The magnitude of R^2 is close to unity in all the graphs of Figs.8.11 and 8.12 which clearly indicates the anticipated linear variation of the measured strains with applied loads. In addition, both the plots in Fig.8.11 exhibit approximately equal slopes of best-fit straight lines. Furthermore, all plots of Fig.8.11 exhibit nearly identical slopes of the best-fit lines. A similar feature can also be noticed in Fig.8.12. All these observations clearly reflect good calibration of the entire experimental setup and the achievement of satisfactory repeatability. Similar trends have been observed in all remaining tests.

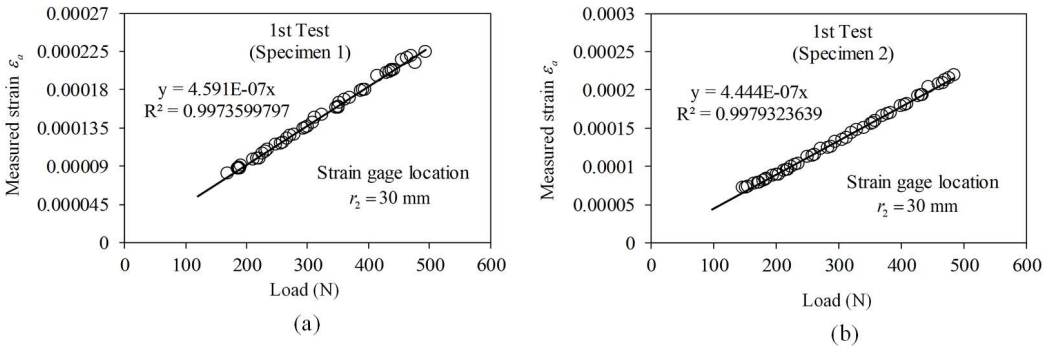

Figure 8.11 Measured strain ε_a at $r_2 = 30$ mm in the first test of the two identical SCB specimens with $\gamma = 35°$, $a / R = 0.3$.

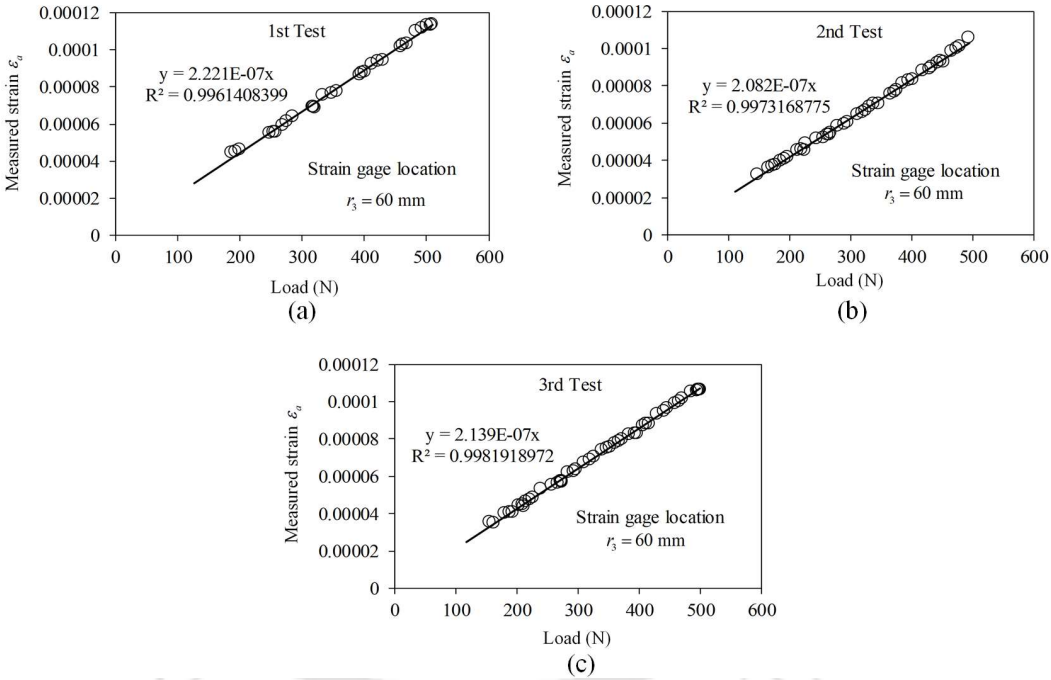

Figure 8.12 Measured strain ε_a at $r_3 = 60$ mm in three repeated tests of the SCB specimen with $\gamma = 60°$, $a / R = 0.3$.

Table 8.15 shows the measured strains ε_a at $r_2 = 30$ mm obtained from the best-fit equations corresponding to results in Fig.8.11(a) for different values of applied loads for $\gamma = 35°$ and $a / R = 0.3$. Similarly, Table 8.16 shows the measured strains ε_a at $r_3 = 60$ mm obtained from the best-fit equations corresponding to the 1st test of the experimental specimen in Fig.8.12(a) for different values of applied loads for $\gamma = 60°$

and $a/R = 0.3$. From both the Tables 8.15 and 8.16, the increasing trend of K_I^V with the increase in applied load could be observed (similar to the SENT cases) but F_I remains constant irrespective of the applied load as expected. Similar trends have been obtained with the strain data of other repeated tests as well.

Table 8.15 Variation of experimental values of K_I^V and F_I at $r_2 = 30$ mm with the applied load in the 1st test of 1st specimen (SCB) for $\gamma = 35°$ and $a/R = 0.3$

Load (N)	Measured strain ε_a	K_I^V (MPa $(mm)^{1-\lambda_1}$)	F_I
50	0.0000230	0.7086	1.5784
100	0.0000459	1.4172	1.5784
150	0.0000689	2.1258	1.5784
200	0.0000918	2.8344	1.5784
250	0.0001148	3.5430	1.5784
300	0.0001377	4.2516	1.5784
350	0.0001607	4.9602	1.5784
400	0.0001836	5.6688	1.5784
450	0.0002066	6.3774	1.5784
500	0.0002296	7.0860	1.5784

Table 8.16 Variation of experimental values of K_I^V and F_I at $r_3 = 60$ mm with the applied load in the 1st test of the experimental specimen (SCB) for $\gamma = 60°$ and $a / R = 0.3$

Load (N)	Measured strain ε_a	K_I^V (MPa $(\text{mm})^{1-\lambda_1}$)	F_I
50	0.0000111	0.7271	1.6715
100	0.0000222	1.4543	1.6715
150	0.0000333	2.1814	1.6715
200	0.0000444	2.9086	1.6715
250	0.0000555	3.6357	1.6715
300	0.0000666	4.3628	1.6715
350	0.0000777	5.0900	1.6715
400	0.0000888	5.8171	1.6715
450	0.0001000	6.5443	1.6715
500	0.0001111	7.2714	1.6715

Table 8.17 shows the experimentally measured values of F_I for two identical SCB specimens of notch angle $\gamma = 35°, a / R = 0.3$ at all the selected radial locations. F_I corresponding to the 1st and 2nd specimens are the averaged values of three repeated tests. Table 8.18 shows the experimental values of F_I for $\gamma = 60°, a / R = 0.3$ at all the selected radial strain gage locations (Table 8.14). In Table 8.18 also, averaged F_I values from all three repeated tests have been reported.

Table 8.17 Experimental values of F_I at valid and invalid locations for the SCB specimens with $\gamma = 35°, a/R = 0.3$ and $r_{max} = 55.62$ mm

Location	F_I				% Relative Error
	1st specimen	2nd specimen	Average	Reference solution (Table 8.4)	
Valid $(r_1 = 15\text{ mm} < r_{max})$	1.4906	1.4979	1.4943	1.5243	1.97
Valid $(r_2 = 30\text{ mm} < r_{max})$	1.5734	1.5832	1.5783		3.54
Invalid $(r_3 = 65\text{ mm} > r_{max})$	1.1719	1.1755	1.1737		23.00

Table 8.18 Experimental values of F_I at valid and invalid locations for the SCB specimens with $\gamma = 60°, a/R = 0.3$ and $r_{max} = 53.38$ mm

Location	F_I		% Relative Error
	Reference solution (Table 8.4)	Experimental value	
Valid $(r_1 = 15\text{ mm} < r_{max})$	2.1273	2.1430	0.74
Valid $(r_2 = 30\text{ mm} < r_{max})$		2.1995	3.39
Invalid $(r_3 = 60\text{ mm} > r_{max})$		1.6991	20.13

It can be seen from Table 8.17 that the measured F_I values of two identical SCB specimens are almost the same at each strain gage location, which clearly further substantiates the good reproducibility of the present experimental results. F_I values of these two identical specimens (Table 8.17) have been further averaged at each radial location and subsequently, the percentage relative error in measured F_I (Eq. (7.8)) has been obtained using the reference solutions obtained using finite element analyses (Table 8.4). These percentage relative errors have also been presented in Table 8.17 for

comparison. Even though the geometries of the SENT and SCB specimens are distinctly different (the former has straight boundaries and the latter has curved boundaries), yet again outstandingly very accurate mode I NSIFs have been extracted from the strain gage readings at both the valid gage locations r_1 and r_2. Again, it is very interesting to notice that although these radial locations ($r_1 = 15$ mm and $r_2 = 30$ mm) are significantly away from the notch tip, yet very accurate NSIFs have been determined by the single strain gage technique proposed in the present thesis. It is worth mentioning here that a similar observation has also been noticed in the case of the SENT specimen. As expected, large and unacceptable errors in F_I can be noticed at invalid locations due to the dominance of a greater number of higher-order Williams' coefficients at the sampling location.

As can be noticed from the results presented in Table 8.18, again strikingly similar trends in the percentage relative error to those observed in the results of Table 8.17 can be noticed. As expected, very accurate NSIFs have been noticed at valid locations, and highly erroneous F_I values have been obtained at the invalid locations. Comparing the results in Table 8.12 and Tables 8.17 and 8.18 (where two valid gage locations are available), the error in F_I obtained at a valid location that is closer to the sharp V-notch tip (i.e., r_1) is relatively small as compared with that at a valid gage location that is comparatively away from the notch tip (i.e., r_2). Nevertheless, at all valid gage locations the error in F_I is very small as compared with that at the invalid locations irrespective of the geometry of the sharp V-notched configuration.

Finally, the results of the present investigation clearly demonstrate the commendable performance of the single strain gage technique with the proposed valid gage locations. The results also clearly demonstrate the role of existence and usefulness of the valid gage locations in obtaining the very accurate mode I NSIFs and the shortcomings of pasting the strain gages based on the guesswork or speculations, as they may lead to the invalid locations. Further, the present results also clearly demonstrate the importance of knowing *a priori* the maximum bound r_{max} as envisaged in the thesis work and the importance of r_{min} as reported in Ref. [114, 119] and Chapter 7 of the present thesis. Thus, if a strain gage is located below the r_{min}, the erroneous NSIFs are mainly due to the 3D effects or strain gradient effects or plasticity

effects or a combination of these issues. On the other hand, if a gage is located beyond the r_{max}, large errors in the measured NSIFs is mainly due to the domination of the higher order Williams' coefficients that are not considered in the formulation. Finally, the results undoubtedly substantiate that the proposed single strain gage technique is simple, efficient and rugged for the accurate measurement of the mode I NSIFs.

8.4 Summary

This chapter verifies experimentally the proposed single strain gage technique which comes along with the strategy of considering valid gage locations for the accurate determination of the mode I NSIFs. Experimental determination of the NSIFs have been carried out on multiple mode I sharp V-notched configurations (SENT and SCB geometries with varied notch angles and a / b ratio). It has been shown that the valid radial gage locations are governed by two parameters r_{min} and r_{max} of a sharp V-notched configuration. It has also been shown experimentally that accurate NSIFs can be obtained only within the range bounded by r_{min} and r_{max}. On the other hand, highly erroneous NSIFs (as high as 30%) are obtained beyond the r_{max}. These experimental findings are consistent with the discussion in Chapter 4. It, therefore, substantiates the importance of the proposed single strain gage technique with valid gage locations.

Chapter 9

Conclusions and scope of the future work

In the present work, a new strain gage technique which comes along with the prediction of the valid gage locations has been proposed for the first time for the accurate measurement of mode I notch stress intensity factors (NSIFs) of the sharp V-notched configurations made of linear elastic and isotropic materials. The proposed technique is based on the popular Dally and Sanford [36] strain gage technique for the crack problems. The proposed strain gage technique requires only one gage and can be pasted at distant locations from the notch tip for the measurement of NSIFs. Two parameters have been defined in the present work to assess the valid gage locations *a priori* viz., the minimum allowable radial gage distance $(r_{\min})$ and the maximum allowable strain gage location $(r_{\max})$. The proposed theory has been supported by the strong theoretical foundations of fracture mechanics. Extensive numerical and experimental verification studies of the proposed theory and methodologies have also been carried out in the present investigation. Conclusions drawn from the present work have been categorized as general conclusions and specific conclusions and are presented in the subsequent sections.

9.1 General conclusions

1. The results of the present investigation clearly demonstrate that the proposed strain gage technique is found to be very simple, efficient, practical and rugged for the determination of the mode I NSIFs of sharp V-notched configurations.
2. The proposed technique requires only one strain gage and can be placed at recommended distant locations from the notch tip for the accurate determination of mode I NSIFs.
3. Numerical and experimental results clearly substantiate the extent of 3D stress-strain zone, 3D to 2D transition zone and plane stress dominance zone a head of a sharp V-notch found by Li and Guo [119].

4. The minimum allowable radial distance (r_{min}) for a strain gage can be taken as $1.25t$ or $1.5t$ for the case of sharp V-notched bodies. It depends only on the thickness of the specimen.
5. The maximum permissible radial distance (r_{max}) for a strain gage also exists and depends only on the geometry of a sharp V-notched configuration. This can be estimated before using the proposed strain gage technique.
6. The results of the present investigation undoubtedly establish that valid strain gage radial locations are those locations that lie between r_{min} and r_{max}.
7. Very accurate mode I NSIFs can be obtained by using the proposed strain gage technique if a strain gage is located at a valid location. Highly erroneous NSIFs can result if a gage is pasted or located at an invalid location.

9.2 Specific conclusions

9.2.1 Conclusions based on finite element analyses for r_{max} of sharp V-notched configurations

1. The results of the present numerical investigation clearly show that the determination of the upper bound of strain gage locations r_{max} is the solution to the determination of the valid radial locations for strain gages in the experimental determination of mode I NSIF.
2. Strains (in the direction of β) along the gage line exhibit $r^{-(1-\lambda_1)}$ singularity only up to the extent of validity of three parameter zone from the notch tip i.e., up to the value of r_{max} for all mode I sharp V-notched configurations studied.
3. A perfect linear trend with a slope equals to $-(1-\lambda_1)$ has been observed on all log-log plots of ε_a versus radial distance along the gage line until a radial distance of r_{max} and thereafter nonlinear trend has been noticed due to the dominance of more number of Williams' coefficients as predicted by the theory. This has been noticed in all the sharp V-notched geometries considered under present work.

4. The computed r_{max} value of all the sharp V-notched configurations considered under the present study converges as the finite element meshes are refined.
5. The proposed methodology for the determination of the r_{max} value of a given configuration is strongly supported by the theory and very accurately can be estimated using proposed approach.
6. The r_{max} is found to be dependent on the ratio of notch length (a) to the plate width (b) and the notch angle γ of a sharp V-notched plate. In majority of the cases, an inverted bell-shaped trend has been observed which is in line with the reported observations made for cracked geometries by other researchers.
7. Simulation results show that the accurate value of K_I^V could be measured using a single strain gage placed at a valid gage location i.e., below the r_{max} value of a configuration.
8. Finite element simulation results also show that placing the gage beyond r_{max}, leads to highly erroneous measurements of K_I^V.
9. The numerical results also demonstrate that it is vital to know the value of r_{max} *a priori*.

9.2.2 Conclusions based on experimental verification of r_{min} for mode I sharp V-notched configurations

1. The results of the experimental investigation corroborate the previous findings of Li and Guo [119], and Nakamura and Parks [114] on various zones and confirm that the minimum radius, r_{min} required for full dominance of the plane stress region dominates is 1.25 times the thickness of the plate as suggested [119].
2. Further, the results also strongly suggest considering the minimum radius r_{min} for the case of sharp V-notches to be equal to 1.5 times the plate thickness which is suggested for crack problems by Nakamura and Parks [114]. This value is found more conservative and highly dependable.

3. The experimental results clearly demonstrate that gage placed below the r_{min} will yield highly erroneous and unacceptable mode I NSIFs. This has been shown mainly due to the dominance of 3D state of stress or 3D-2D transition state of stress.
4. The results of this experimental investigation also indicate that not only the sampling in the plane stress region is important but also the location of the measurement points within the plane stress region plays a vital role in achieving the desired accuracy. Conversely, r_{max} is also an important parameter in deciding the accuracy of the measured mode I NSIFs.

9.2.3 Conclusions based on the experimental determination of mode I NSIFs using valid gage locations of sharp V-notched configurations

1. A perfect linear relationship between the measured strain and the applied load has been observed in all the repeated experiments of the present investigation.
2. The trends of the measured mode I NSIFs have been found in accordance with the theoretical predictions.
3. Measured normalized mode I NSIFs from all the repeated experiments have been found nearly equal to each other indicating excellent calibration of the present experimental set up.
4. It has been demonstrated that two parameters r_{min} and r_{max} of a sharp V-notched configuration are essential for the correct assessment of the valid gage locations.
5. The results of the present investigation clearly establishes that the valid gage locations are those locations that satisfy the condition $r_{min} \le r \le r_{max}$. Further, it has also been substantiated that the radial locations that do not satisfy the above condition are invalid gage locations.
6. The results of this investigation clearly show that very accurate NSIFs K_I^V can be obtained from the strain gage readings located at valid gage locations
7. Depending on the r_{max} value of a configuration these valid locations can be at distant locations from the tip of a notch.

8. Further, the present results also show that highly erroneous NSIFs K_I^V can results from the readings of the strain gages that are located at invalid radial locations. The results clearly show that invalid gage locations constitute 3D stress-strain zones, 3D to 2D transition zones and plane stress dominance zones wherein measured strains are dominated by the more number of higher order Williams' coefficients than considered in the present investigation.
9. The present results clearly indicate the necessity of knowing *a priori* the values of $r_{\min}$ and $r_{\max}$ of a sharp V-notched configurations for accurate measurement of NSIFs.
10. Finally, the presented results clearly indicate excellent performance of the proposed single strain gage technique with valid gage locations for the accurate determination of NSIFs K_I^V.

9.3 Scope for future work

1. The proposed single strain gage technique can also be extended to plane strain problems.
2. There is future scope for extending the proposed methodology to mode II and mixed-mode (I/II) loading conditions i.e., inclined notches and non-symmetric notched geometries.
3. Experiments could be performed with the specimen made of metallic materials to study the effect of plasticity in the determination of NSIFs using the strain gages placed at valid locations.
4. The proposed procedure can be extended for the determination of mode I NSIFs in orthotropic panels with sharp V-notches.
5. The extent of 3D and 3D-2D transition zones by Li and Guo [119], and Nakamura and Parks [114] have been primarily studied for mode I configurations. It is not clear whether or not the same $r_{\min}$ value can be used for the say mixed mode (I/II) problems. Therefore, it is necessary to study the $r_{\min}$ under mixed mode (I/II) loading conditions.

6. It is important to study whether or not the same r_{min} value i.e., 1.5 times the thickness can be recommended for other geometries of the sharp V-notched bodies other than those considered in the present investigation.
7. Similarly, it is also necessary to study the determination of r_{max} values under mixed mode (I/II) loading conditions.
8. It is important to make an attempt to obtain a fit or empirical relation between of the form $r_{max} = r_{max}(a/b, \gamma)$ for different benchmark geometries.

References

[1] **C. E. Inglis**, Stresses in a plate due to the presence of cracks and sharp corners, *Transactions of the Royal Institute of Naval Architects* (1913), 60, 219–214.

[2] **A. A. Griffith**, The phenomenon of rupture and flow in solids, *Philosophical Transactions Series A* (1920), 221, 163–198.

[3] **S. Y. Yarema**, On the contribution of G. R. Irwin to fracture mechanics, *Materials Science* (1996), 31, 617-623.

[4] **H. M. Westergaard**, Bearing pressures and cracks, *Journal of Applied Mechanics* (1939), 61, 49-53.

[5] **M. L. Williams**, On the stress distribution at the base of a stationary crack, *Journal of Applied Mechanics* (1957), 24, 109–114.

[6] **G. R. Irwin**, Analysis of stresses and strains near the end of a crack traversing a plate, *Journal of Applied Mechanics* (1957), 24, 361-364.

[7] **D. Leguillon** and **Z. Yosibash**, Failure initiation at V-notch tips in quasi-brittle materials, *International Journal of Solids and Structures* (2017), 122-123, 1–13.

[8] **H. Mohammadi**, **H. Salavati**, **Y. Alizadeh**, **F. Berto** and **S. V. Panin**, Fracture investigation of V-notch made of tungsten-copper functionally graded materials, *Physical Mesomechanics* (2017), 20, 457–464.

[9] **N. Razavi**, **P. Ferro**, **F. Berto** and **J. Torgersen**, Fatigue strength of blunt V-notched specimens produced by selective laser melting of Ti-6Al-4V, *Theoretical and Applied Fracture Mechanics* (2018), 97, 376–384.

[10] **F. Stojceveski**, **A. Hendlmeier**, **J. D. Randall**, **C. L. Arnold**, **M. K. Stanfield**, **D. J. Eyckens**, **R. Alexander** and **L. C. Henderson**, Effect of tow size and interface interaction on interfacial shear strength determined by iosipescu (V-Notch) testing in epoxy resin, *Materials* (2018), 11 (9), 1786.

[11] **W. Reitz**, Failure of bolt threads exposed to shear stress, *Journal of Failure Analysis and Prevention* (2013), 13, 551-554.

[12] **K. Reed**, Equipment Failure: Crane Gearbox Failure, 2016, https://www.taproot.com/equipment-failure-crane-gearbox-failure/(accessed14 August 2024).

[13] **K. Tomari**, **S. Tonogai**, **T. Harada**, **H. Hamada**, **K. Lee**, **T. Morii**, and **Z. Maekawa**, The V-notch at weld lines in polystyrene injection moldings, *Polymer Engineering and Science* (1990), 30, 931-936.

[14] **M. L. Dunn**, **W. Suwito** and **S. Cunningham**, Stress intensities at notch singularities, *Engineering Fracture Mechanics* (1997), 57, 417–430.

[15] **A. Rezaee** and **A. Adnan**, On the elastic stress singularities and mode I notch stress intensity factor for 3D printed polymers, *Engineering Fracture Mechanics* (2018), 204, 235–245.

[16] **Y. Verreman** and **B. Nie**, Early development of fatigue cracking at manual fillet welds, *Fatigue and Fracture of Engineering Materials and Structures* (1996), 19, 669–681.

[17] **P. Lazzarin** and **R. Tovo**, A notch intensity factor approach to the stress analysis of welds, *Fatigue and Fracture of Engineering Materials and Structures* (1998), 21, 1089–1103.

[18] **P. Lazzarin** and **P. Livieri**, Notch stress intensity factors and fatigue strength of aluminium and steel welded joints, *International Journal of Fatigue* (2001), 23, 225–232.

[19] **M. L. Williams**, Stress singularities resulting from various boundary conditions in angular corners of plates in extension, *Journal of Applied Mechanics* (1952), 19, 526–528.

[20] **R. J. Hartranft** and **G. C. Sih**, Effect of plate thickness on the bending stress distribution around through cracks, *Journal of Mathematics and Physics* (1968), 47, 276–291.

[21] **R. J. Hartranft** and **G. C. Sih**, The use of eigenfunction expansions in the general solution of three-dimensional crack problems, *Journal of Mathematics and Mechanics* (1969), 19, 123–138.

[22] **A. R. Torabi**, Estimation of tensile load-bearing capacity of ductile metallic materials weakened by a V-notch: The equivalent material concept, *Materials Science and Engineering: A* (2012), 536, 249– 255.

[23] **A. Seweryn**, Brittle fracture criterion for structures with sharp notches, *Engineering Fracture Mechanics* (1994), 47, 673–681.

[24] **P. Lazzarin** and **R. Zambardi**, A finite-volume-energy based approach to predict the static and fatigue behavior of components with sharp V-shaped notches, *International Journal of Fracture* (2001), 112, 275–298.

[25] **F. J. Gómez** and **M. Elices**, Fracture of components with V-shaped notches, *Engineering Fracture Mechanics* (2003), 70, 1913–1927.

[26] **P. Livieri**, A new path independent integral applied to notched components under mode I loadings, *International Journal of Fracture* (2003), 123, 107–125.

[27] **D. Leguillon** and **Z. Yosibash**, Crack onset at a v-notch. Influence of the notch tip radius, *International Journal of Fracture* (2003), 122, 1–21.

[28] **M. R. Ayatollahi** and **A. R. Torabi**, Brittle fracture in rounded-tip V-shaped notches, *Materials* and *Design* (2010), 31, 60-67.

[29] **M. R. Ayatollahi**, **A. R. Torabi** and **P. Azizi**, Experimental and theoretical assessment of brittle fracture in engineering components containing a sharp V-notch, *Experimental Mechanics* (2011), 51, 919–932.

[30] **F. Berto**, **P. Lazzarin** and **R. Afshar**, Simple new expressions for the notch stress intensity factors in an array of narrow V-notches under tension, *International Journal of Fracture* (2012), 176, 237–244.

[31] **R. J. Sanford**, *Principles of Fracture Mechanics*, Upper Saddle River, NJ: Prentice Hall, (2003).

[32] **A. J. Rosakis**, **A. T. Zehinder** and **R. Narashim**, Caustics by reflection and their application to elastic-plastic and dynamic fracture mechanics, *Optical Engineering* (1988), 27, 278596.

[33] **M. Mahinfalah** and **L. Zackery**, Photoelastic determination of mixed mode stress intensity factors for sharp reentrant corners, *Engineering Fracture Mechanics* (1995), 52, 639-645.

[34] **M.R. Ayatollahi** and **M. Nejati**, Experimental evaluation of stress field around the sharp notches using photoelasticity, *Materials* and *Design* (2011), 32, 561-569.

[35**] L. Shi** and **S.O. Oyadiji**, Determination of notch stress intensity factors under mode I loading using the 3D-DIC and finite element over-deterministic methods, *Engineering Fracture Mechanics* (2024), 296, 109852.

[36] **J.W. Dally** and **R.J. Sanford,** Strain-gage methods for measuring the opening-mode stress- intensity factor, K_I, *Experimental Mechanics* (1987), 27, 381–388.

[37] **P. Lazzarin**, **P. Livieri**, **F. Berto** and **M. Zappalorto**, Local strain energy density and fatigue strength of welded joints under uniaxial and multiaxial loading, *Engineering Fracture Mechanics* (2008), 75, 1875-1889.

[38] **P. Lazzarin**, **F. Berto**, **F. J. Gomez** and **M. Zappalorto**, Some advantages derived from the use of the strain energy density over a control volume in fatigue strength assessments of welded joints, *International Journal* of *Fatigue* (2008), 30, 1345-1357.

[39] **A. Carpinteri**, Stress-singularity and generalized fracture toughness at the vertex of re-entrant corners, *Engineering Fracture Mechanics* (1987), 26, 143–155.

[40] **M.L. Dunn**, **W. Suwito** and **S. Cunningham**, Fracture initiation at sharp notches: correlation using critical stress intensities, *International Journal of Solids and Structures* (1997), 34, 3873–3883.

[41] **M.L. Dunn**, **W. Suwito**, **S. Cunningham** and **C.W. May**, Fracture initiation at sharp notches under mode I, mode II, and mild mixed mode loading, *International Journal of Fracture* (1997), 84, 367–381.

[42] **Z. Yosibash, A. Bussiba** and **I. Gilad**, Failure criteria for brittle elastic materials, *International Journal of Fracture* (2004), 125, 307–333.

[43] **Z. Yosibash**, **E. Priel** and **D. Leguillon**, A failure criterion for brittle elastic materials under mixed-mode loading, *International Journal of Fracture* (2006), 141, 291–312.

[44] **S.Q. Hou** and **J.Q. Xu**, An evaluation method for brittle fracture from a singular point with arbitrary singularities, *International Journal of Mechanical Sciences* (2014), 88, 202–207.

[45] **M.P. Savruk** and **A. Kazberuk**, Two-dimensional fracture mechanics problems for solids with sharp and rounded V-notches, *International Journal of Fracture* (2010), 161, 79–95.

[46] **F. Berto** and **P. Lazzarin**, Recent developments in brittle and quasi-brittle failure assessment of engineering materials by means of local approaches, *Materials Science and Engineering: R: Reports* (2014), 75, 1–48.

[47] **W. Shi,** Equivalence of the notch stress intensity factor, tip opening displacement and energy release rate for a sharp V-notch, *International Journal of Solids and Structures* (2014), 51, 904-909.

[48] **A. R. Torabi** and **S. M. Abedinasab**, Mode II notch fracture toughness measurement for key-hole notches by the disk test, *Journal of Strain Analysis for Engineering Design* (2015), 50, 264–275.

[49] **N. Hasebe** and **Y. Kutanda**, Calculation of stress intensity factor from stress concentration factor, *Engineering Fracture Mechanics* (1978), 10, 215–221.

[50] **D. J. Hart**, A note on the plate width and notch angle correction factors for single edge V-notched plates in tension, *Engineering Fracture Mechanics* (1976), 8, 47–48.

[51] **B. Zhao**, **L. Fuyuan** and **W. Qingtong**, Determining K_I of a V-notch from the existing results of a linear crack, *Engineering Fracture Mechanics* (1988), 31, 923–929.

[52] **Z. Zhao** and **H. G. Hahn**, Determining the SIF of a V-notch from the results of a mixed-mode crack, *Engineering Fracture Mechanics* (1992), 43, 511–518.

[53] **B. Loua** and **N. Barltrop**, Universal hybrid method and approximate closed-form solution for V-notched and V-notch-cracked plate under tensile and in-plane bending, *Theoretical and Applied Fracture Mechanics* (2020), 108, 102579.

[54] **M. K. Hussain** and **K. S. R. K. Murthy**, A point substitution displacement technique for estimation of elastic notch stress intensities of sharp V-notched bodies, *Theoretical and Applied Fracture Mechanics* (2018), 97, 87–97.

[55] **M. K. Hussain** and **K. S. R. K. Murthy**, Calculation of mixed mode (I/II) stress intensities at sharp V-notches using finite element notch opening and sliding displacements, *Fatigue and Fracture of Engineering Materials and Structures* (2019), 42, 1130-1147.

[56] **M. K. Hussain** and **K.S.R.K. Murthy**, Comparison of methods for estimating notch stress intensities at sharp V-notches, *Journal of Mechanics of Materials and Structures* (2022), 17, 123-147.

[57] **A. Visentin**, **A. Campagnolo** and **G. Meneghetti**, Analytical expressions to estimate rapidly the notch stress intensity factors at V-notch tips using the Peak Stress Method, *Fatigue and Fracture of Engineering Materials and Structures* (2023), 46, 1572-1595.

[58] **G. Meneghetti** and **P. Lazzarin**, Significance of the elastic peak stress evaluated by FE analyses at the point of singularity of sharp V-notched components, *Fatigue and Fracture of Engineering Materials and Structures* (2007), 30, 95–106.

[59] **M. Lepore, K. Solberg** and **F. Berto,** A comparison between numerical and approximate methods for rapid calculation of NSIFs, *Theoretical and Applied Fracture Mechanics* (2019), 101, 67-79.

[60] **M. R. Mehraban, M. R. Ayatollahi, B. Bahrami** and **F. Berto,** Higher order stress terms in sharp notch problems under pure-out-of-plane loading, *Fatigue and Fracture of Engineering Materials and Structures* (2022), 45, 500-513.

[61] **S. De Miranda** and **F. Ubertini**, Stress analysis around holes or notches by special finite elements, *International Journal for Numerical Methods in Engineering* (2006), 66, 85–116.

[62] **M. Zappalorto** and **P. A. Carraro**, An efficient energy-based approach for the numerical assessment of mode I NSIFs in isotropic and orthotropic notched plates, *Theoretical and Applied Fracture Mechanics* (2020), 108, 102612.

[63] **D. H. Chen**, Stress intensity factors for V-notched strip under tension or in-plane bending, *International Journal* of *Fracture* (1994), 70, 81–97.

[64] **M. Stern**, **E.B. Becker** and **R.S. Dunham**, A contour integral computation of mixed-mode stress intensity factors, *International Journal of Fracture* (1976), 12, 359–368.

[65] **M.R. Ayatollahi** and **M. Nejati**, Determination of NSIFs and coefficients of higher order terms for sharp notches using finite element method, *International Journal of Mechanical Sciences* (2011), 53, 164–177.

[66] **B. Gross** and **A. Mendelson**, Plane elastostatic analysis of V-notched plates, *International Journal of Fracture Mechanics* (1972), 8, 267–276.

[67] **Y. Liu**, **Z. Wu**, **Y. Liang** and **X. Liu**, Numerical methods for determination of stress intensity factors of singular stress field, *Engineering Fracture Mechanics* (2008), 75, 4793–4803.

[68] **G. Meneghetti**, **A. Campagnolo**, **M. Avalle**, **D. Castagnetti**, **M. Colussi**, **P. Corigliano**, **M. De Agostinis**, **E. Dragoni**, **V. Fontanari**, **F. Frendo**, **L. Goglio**, **G. Marannano, G. Marulo, F. Moroni, A. Pantano, A. Rebora, A. Scattina, A. Spaggiari** and **B. Zuccarello,** Rapid evaluation of notch stress intensity factors using the peak stress method: Comparison of commercial finite element codes for a range of mesh patterns, *Fatigue and Fracture of Engineering Materials and Structures* (2018), 41, 1044-1063.

[69] **S.H. Ju** and **H.Y. Chung**, Accuracy and limit of a least squares method to calculate 3D notch SIFs, *International Journal of Fracture* (2007), 148, 169–183.

[70] **P. Lazzarin**, **F. Berto** and **M. Zappalorto**, Rapid calculations of notch stress intensity factors based on averaged strain energy density from coarse meshes: theoretical bases and applications, *International Journal* of *Fatigue* (2010), 32, 1559–1567.

[71] **T. Kondo, M. Kobayashi** and **H. Sekine**, Strain gage method for determining stress intensities of sharp-notched strips, *Experimental Mechanics* (2001), 41, 1-7.

[72] **T. Kondo, Y. Kurabe, T. Sasaki, T. Kurahashi** and **Y. Miyashita,** Use of strain gages for determining generalized stress intensity factors of sharp V-notched plates under transverse bending, *Engineering Fracture Mechanics* (2014), 124–125, 248-261.

[73] **L. Peng**, **Z. Yue**, **X. Yue**, **J. Liu**, **Y. Qiao**, **C. Chen**, **S. Xu** and **P. Qiu**, V-notch crack toughness of PMMA by strain gages and its comparison with caustics results under impact loading, *Mechanics of Advanced Materials and Structures* (2021), 29, 5378-5392.

[74] **M. Shozu**, **Y. Kawagishi**, **T. Sasaki** and **Y. Hirose**, Effect of specimen configuration for caustics method, In *ISOPE International Ocean and Polar Engineering Conference* (1995) (pp. ISOPE-I). ISOPE.

[75] **J. Galkiewicz** and **A. Neimitz**, Analysis of the stress field in front of a notch, *Materials Science* (1998), 34, 714–723.

[76] **W. Xu**, **X. F. Yao**, **M. Q. Xu**, **G. C. Jin** and **H. Y. Yeh**, Fracture characterizations of V-notch tip in PMMA polymer material, *Polymer Testing* (2004), 23, 509–515.

[77] **J.N. Prassianakis** and **P.S. Theocaris**, Stress intensity factors at V-notched elastic, symmetrically loaded, plates by the method of caustics, *Journal of Physics D: Applied Physics* (1980), 13, 1043-1053.

[78] **A. Yazdanmehr** and **N. Soltani**, Evaluation of stress intensity factors of rounded V and U notches under mixed mode loading, using the experimental method of caustics, *Theoretical and Applied Fracture Mechanics* (2014), 74, 79-85.

[79] **L. Yang**, **H. Hu**, **Y. Song** and **Y.J. Chao**, Determination of stress intensity factor of sharp V-notch under pure shear loading by the caustic method, *Applied Optics* (2020), 59, 10168-10176.

[80] **W. Liu**, **L. Li**, **P. Xu** and **Z. Yue**, Evaluation of generalized stress intensity factors at blunt V-notch tip in polymer materials using transmitted caustics, *Mechanics of Advanced Materials and Structures* (2022), 29, 2845-2856.

[81] **W. Liu**, **Z. Ma**, **L. Li** and **Z. Yue**, Photoelastic evaluation of stress fields and notch stress intensity factors for blunt V-notches, *Theoretical and Applied Fracture Mechanics* (2020), 110, 102806.

[82] **M. R. Ayatollahi**, **M. M. Mirsayar** and **M. Dehghany**, Experimental determination of stress field parameters in bi-material notches using photoelasticity, *Materials and Design* (2011), 32, 4901– 4908.

[83] **S. N. Murthy** and **P. R. Rao**, Determination of mode I notch stress intensity factor by the photoelastic technique, *Engineering Fracture Mechanics* (1985), 21, 557–562.

[84] **A. R. Torabi**, **B. Bahrami** and **M. R. Ayatollahi**, Experimental determination of the notch stress intensity factor for sharp V-notched specimens by using the digital image correlation method, *Theoretical and Applied Fracture Mechanics* (2019), 103, 102244.

[85] **A. R. Torabi**, **B. Bahrami** and **M. R. Ayatollahi**, On the use of digital image correlation method for determining the stress field at blunt V-notch neighbourhood, *Engineering Fracture Mechanics* (2020), 223, 106768.

[86] **B. Bahrami**, **M. R. Ayatollahi** and **A. R. Torabi**, Application of digital image correlation method for determination of mixed mode stress intensity factors in sharp notches, *Optics and Lasers in Engineering* (2020), 124, 105830.

[87] **L. Shi** and **S.O. Oyadiji**, Determination of notch stress intensity factors for V-notched specimens under mode I loading using the 3D-Digital image correlation and strain energy approach, *Theoretical and Applied Fracture Mechanics* (2024), 130, 104307.

[88] **X. Dai, H. Ye, T. Yuan, X. Shao, Z. Zu, X. Cheng, H. Yun, Y. Wang, F. Yang** and **X. He,** Strain determination based on strain gauge-guided radial basis function and digital image correlation, *Optics and Lasers in Engineering* (2020), 126, 105894.

[89] **S.H. Ju**, Calculation of Notch H-integrals using image correlation experiments, *Experimental Mechanics* (2010), 50, 517-525.

[90] **S.H. Ju**, **H.Y. Chung** and **S.H. Liu**, Determining 2D notch SIFs by the image-correlation method, *Journal of the Chinese Institute of Engineers* (2011), 34, 503-514.

[91] **M.R.Y. Dehnavi**, **I. Eshraghi** and **N. Soltani**, Investigation of fracture parameters of edge V-notches in a polymer material using digital image correlation, *Polymer Testing* (2013), 32, 778-784.

[92] **Y. Yuan**, **W. Hao** and **Y. Ma**, Stress field at V-notch tip in polymer materials using digital gradient sensing, *Mechanics of Advanced Materials and Structures* (2017), 24, 350–356.

[93] **D. Chen, R. Zhang** and **R. Guo,** Studying V-notch stress intensity factor by digital gradient sensing method, *Acta Mechanica Solida Sinica* (2019), 32, 378–392.

[94] **X. F. Yao, H. Y. Yeh** and **W. Xu,** Fracture investigation at V-notch tip using coherent gradient sensing (CGS), *International Journal of Solids and Structures* (2006), 43, 1189-1200.

[95] **K. Ravi-chandar**, *Fracture mechanics*, In: W.N. Sharpe Jr.editor, Springer handbook of experimental solid mechanics, New York, (2008), pp. 125–158.

[96] **J. W. Dally** and **D. B. Barker**, Dynamic measurements of initiation toughness at high loading rates, *Experimental Mechanics* (1988), 28, 298-303.

[97] **A. Shukla**, **B. D. Agarwal** and **B. Bhushan**, Determination of stress intensity factor in orthotropic composite materials using strain gages, *Engineering Fracture Mechanics* (1989), 32, 469–477.

[98] **J. W. Dally** and **J. R. Berger**, A strain gage method for determining K_I and K_{II} in a mixed mode stress field, *Proceeding of the 1986 SEM Spring Conference on Experimental Mechanics* (1986), 603-613.

[99] **S. K. K. Hanna** and **A. Shukla**, Development of stress field equations and determination of stress intensity factor during dynamic fracture of orthotropic composite materials, *Engineering Fracture Mechanics* (1994), 47, 345–359.

[100] **H. Sarangi, K. S. R. K. Murthy** and **D. Chakraborty**, Experimental verification of optimal strain gage locations for the accurate determination of mode I stress intensity factors, *Engineering Fracture Mechanics* (2013), 110,189–200.

[101] **H. Sarangi, K. S. R. K. Murthy** and **D. Chakraborty**, Optimum strain gage location for evaluating stress intensity factors in single and double ended cracked configurations, *Engineering Fracture Mechanics* (2010), 77, 3190-3203.

[102] **H. Sarangi, K. S. R. K. Murthy** and **D. Chakraborty**, Radial locations of strain gages for accurate measurement of mode I stress intensity factor, *Materials and Design* (2010), 31, 2840-2850.

[103] F. **Mejni, T. Kanit, J. M. Nianga** and **A. Imad,** An examination of techniques based on two strain gages for the determination of stress intensity factor K_I, *Engineering Fracture Mechanics* (2020), 236, 107191.

[104] **A. Talha, F. Mejni, R. Boutarfa** and **N. Benseddiq,** A strain gage technique for measuring the mode II stress intensity factors, *Engineering Fracture Mechanics* (2024), 304, 110166.

[105] **Q. Li, C. Huang, Z. Gao, K. Wang, W. Xu** and **H. Li,** Strain gauge experimental study on mode I rock fracture characteristics under impact loading, *Engineering Fracture Mechanics* (2021), 253, 107858.

[106] **J. Wei** and **J.H. Zhao**, A two-strain-gage technique for determining mode I stress-intensity factor, *Theoretical and Applied Fracture Mechanics* (1997), 28, 135–140.

[107] **L. Parnas**, **ÖG Bilir** and **E Tezcan**, Strain gage methods for measurement of opening mode stress intensity factor, *Engineering Fracture Mechanics* (1996), 55, 485–492.

[108] **S. Swamy**, **M.V. Srikanth**, **K.S.R.K. Murthy** and **P.S. Robi**, Determination of mode I stress intensity factors of complex configurations using strain gages, *Journal of Mechanics of Materials and Structures* (2008), 3, 1239–1255.

[109] **Z. P. Bažant** and **L.F. Estenssoro**, Surface singularity and crack propagation, *International Journal of Solids and Structures* (1979), 15, 405–426.

[110] **L. P. Pook**, **F. Berto** and **A. Campagnolo**, State of the art of corner point singularities under in-plane and out-of-plane loading, *Engineering Fracture Mechanics* (2017), 174, 2–9.

[111] **N.T. Younis** and **B. Kang**, Averaging effects of a strain gage, *Journal of Mechanical Science and Technology* (2011), 25, 163–169.

[112] **N.T. Younis** and **J. Mize**, Discrete averaging effects of a strain gage at a crack tip, *Engineering Fracture Mechanics* (1996), 55, 147–153.

[113] **R. Chona**, **G.R. Irwin** and **R.J. Sanford**, The influence of specimen size and shape on the singularity-dominated zone, ASTM STP, 791 (1983) 3–13.

[114] **T. Nakamura** and **D.M. Parks**, Three-dimensional stress field near the crack front of a thin elastic plate, *Journal of Applied Mechanics* (1988), 55, 805–813.

[115] **T. Nakamura** and **D.M. Parks**, Antisymmetrical 3-D stress field near the crack front of a thin elastic plate, *International Journal of Solids and Structures* (1989), 25, 1411-1426.

[116] **Z. Li**, **W. Guo** and **Z. Kuang**, Three-dimensional elastic stress fields near notches in finite thickness plates, *International Journal of Solids and Structures* (2000), 37, 7617-7632.

[117] **R. C. de Oliveira Góes**, **J. T. P. de Castro** and **L. F. Martha**, 3D effects around notch and crack tips, *International Journal of Fatigue* (2014), 62, 159-170.

[118] **A. J. Rosakis** and **K. Ravi-Chandar**, On crack-tip stress state: An experimental evaluation of three-dimensional effects, *International Journal of Solids and Structures* (1986), 22, 121-134.

[119] **Z. Li** and **W. Guo**, Three-dimensional elastic stress fields ahead of blunt V-notches in finite thickness plates, *International Journal of Fracture* (2001), 107, 53–71.

[120] **T. M. Maccagno** and **J. F. Knott**, The fracture behaviour of PMMA in mixed modes I and II, *Engineering Fracture Mechanics* (1989), 34, 65-68.

[121] **B. Mukherjee** and **D. J. Burns**, Growth of part through thickness fatigue cracks in sheet Polymethylmethacrylate, *Engineering Fracture Mechanics* (1972), 4, 665-685.

[122] **F. G. Katsamanis** and **C. G. Delides**, Fracture surface energy measurements of PMMA, A new experimental approach, *Journal of Physics D: Applied Physics* (1988), 21, 79-86.

[123] **M. Treifi, S. O. Oyadiji** and **D. K. L. Tsang**, Computations of the stress intensity factors of double-edge and centre V-notched plates under tension and anti-plane shear by the fractal-like finite element method, *Engineering Fracture Mechanics* (2009), 76, 2091–2108.

This page is left blank intentionally

Appendix - A

$$f_1(\theta,\beta,\lambda_1,\nu,\gamma)=\lambda_1\begin{Bmatrix}\cos^2\beta\left[\cos\theta(\lambda_1-3)+\cos\theta(\lambda_1-1)\left[2\kappa+\cos\lambda_1(2\pi-\gamma)\right]\right]-\\ \cos\theta(\lambda_1-3)\sin^2\beta+2\kappa\cos\theta(\lambda_1-1)\sin^2\beta-\\ \cos\theta(\lambda_1-1)\cos\lambda_1(2\pi-\gamma)\sin^2\beta-\\ \sin\theta(\lambda_1-3)\sin 2\beta-\cos\lambda_1(2\pi-\gamma)\sin\theta(\lambda_1-1)\sin 2\beta-\\ \lambda_1\cos^2\beta\cos\theta(\lambda_1-3)+\lambda_1\cos^2\beta\cos\gamma\cos\theta(\lambda_1-1)+\\ \lambda_1\cos\theta(\lambda_1-3)\sin^2\beta-\lambda_1\cos\gamma\cos\theta(\lambda_1-1)\sin^2\beta+\\ \lambda_1\sin\theta(\lambda_1-3)\sin 2\beta-\lambda_1\cos\gamma\sin\theta(\lambda_1-1)\sin 2\beta\end{Bmatrix} \quad \text{(A.1)}$$

$$f_2(\theta,\beta,\lambda_2,\lambda_2^*,\gamma,\nu,r)=\begin{Bmatrix}((-\cos[2\beta+\theta(\lambda_2-3)]+\cos\gamma\cos[2\beta+\theta(\lambda_2-1)])\cos[\log[r]\lambda_2^*]\cosh[\theta\lambda_2^*]+\\ (-\sin[2\beta+\theta(\lambda_2-3)]+\cos\gamma\sin[2\beta+\theta(\lambda_2-1)])\sin[\log[r]\lambda_2^*]\sinh[\theta\lambda_2^*])\lambda_2^2+\\ \lambda_2(\cosh[\theta\lambda_2^*]((\cos[2\beta+\theta(\lambda_2-3)]+2\kappa\cos[\theta(\lambda_2-1)])\cos[\log[r]\lambda_2^*]+\\ \cos[2\beta+\theta(\lambda_2-1)]\cos[(2\pi-\gamma)\lambda_2]\cos[\log[r]\lambda_2^*]\cosh[(2\pi-\gamma)\lambda_2^*]+\\ \cos[2\beta+\theta(\lambda_2-1)]\sin[(2\pi-\gamma)\lambda_2]\sin[\log[r]\lambda_2^*]\sinh[(2\pi-\gamma)\lambda_2^*])+\\ (\cos[(2\pi-\gamma)\lambda_2]\cosh[(2\pi-\gamma)\lambda_2^*]\sin[2\beta+\theta(\lambda_2-1)]\sin[\log[r]\lambda_2^*]+\\ (\sin[2\beta+\theta(\lambda_2-3)]+2\kappa\sin[\theta(\lambda_2-1)])\sin[\log[r]\lambda_2^*]-\\ \cos[\log[r]\lambda_2^*]\sin[2\beta+\theta(\lambda_2-1)]\sin[(2\pi-\gamma)\lambda_2]\sinh[(2\pi-\gamma)\lambda_2^*])\sinh[\theta\lambda_2^*]+\\ ((2\cos[2\beta+\theta(\lambda_2-3)]-2\cos\gamma\cos[2\beta+\theta(\lambda_2-1)])\cosh[\theta\lambda_2^*]\sin[\log[r]\lambda_2^*]+\\ \cos[\log[r]\lambda_2^*](-2\sin[2\beta+\theta(\lambda_2-3)]+2\cos\gamma\sin[2\beta+\theta(\lambda_2-1)])\sinh[\theta\lambda_2^*])\lambda_2^*)+\\ \lambda_{22}(\cosh\left[\theta\lambda_2^*\right]((-\cos[2\beta+\theta(\lambda_2-3)]-2\kappa\cos[\theta(\lambda_2-1)])\sin[\log[r]\lambda_2^*]-\\ \cos[2\beta+\theta(\lambda_2-1)]\cos[(2\pi-\gamma)\lambda_2]\cosh[(2\pi-\gamma)\lambda_2^*]\sin[\log[r]\lambda_2^*]+\\ \cos[2\beta+\theta(\lambda_2-1)]\cos[\log[r]\lambda_2^*]\sin[(2\pi-\gamma)\lambda_2]\sinh[(2\pi-\gamma)\lambda_2^*])+\\ (\cos[(2\pi-\gamma)\lambda_2]\cos[\log[r]\lambda_2^*]\cosh[(2\pi-\gamma)\lambda_2^*]\sin[2\beta+\theta(\lambda_2-1)]+\\ \cos[\log[r]\lambda_2^*](\sin[2\beta+\theta(\lambda_2-3)]+2\kappa\sin[\theta(\lambda_2-1)])+\\ \sin[2\beta+\theta(\lambda_2-1)]\sin[(2\pi-\gamma)\lambda_2]\sin[\log[r]\lambda_2^*]\sinh[(2\pi-\gamma)\lambda_2^*])\sinh[\theta\lambda_2^*]+\\ ((\cos[2\beta+\theta(\lambda_2-3)]-\cos\gamma\cos[2\beta+\theta(\lambda_2-1)])\cos[\log[r]\lambda_2^*]\cosh[\theta\lambda_2^*]+\\ (\sin[2\beta+\theta(\lambda_2-3)]-\cos\gamma\sin[2\beta+\theta(\lambda_2-1)])\sin[\log[r]\lambda_2^*]\sinh[\theta\lambda_2^*])\lambda_2^*)\end{Bmatrix} \quad \text{(A.2)}$$

$$f_2^*(\theta,\beta,\lambda_2,\lambda_2^*,\gamma,\nu,r)=\left\{\begin{array}{l}((\cos[2\beta+\theta(\lambda_2-3)]-\cos\gamma\cos[2\beta+\theta(\lambda_2-1)])\cosh[\theta\lambda_2^*]\sin[\log[r]\lambda_2^*]\\+\cos[\log[r]\lambda_2^*](-\sin[2\beta+\theta(\lambda_2-3)]+\cos\gamma\sin[2\beta+\theta(\lambda_2-1)])\sinh[\theta\lambda_2^*])\lambda_2^2\\+\lambda_2^*(\cosh[\theta\lambda_2^*]((-\cos[2\beta+\theta(\lambda_2-3)]-2\kappa\cos[\theta(\lambda_2-1)])\cos[\log[r]\lambda_2^*]-\\\cos[2\beta+\theta(\lambda_2-1)]\cos[(2\pi-\gamma)\lambda_2]\cos[\log[r]\lambda_2^*]\cosh[(2\pi-\gamma)\lambda_2^*]-\\\cos[2\beta+\theta(\lambda_2-1)]\sin[(2\pi-\gamma)\lambda_2]\sin[\log[r]\lambda_2^*]\sinh[(2\pi-\gamma)\lambda_2^*])+\\(-\cos[(2\pi-\gamma)\lambda_2]\cosh[(2\pi-\gamma)\lambda_2^*]\sin[2\beta+\theta(\lambda_2-1)]\sin[\log[r]\lambda_2^*]+\\(-\sin[2\beta+\theta(\lambda_2-3)]-2\kappa\sin[\theta(\lambda_2-1)])\sin[\log[r]\lambda_2^*]+\\\cos[\log[r]\lambda_2^*]\sin[2\beta+\theta(\lambda_2-1)]\sin[(2\pi-\gamma)\lambda_2]\sinh[(2\pi-\gamma)\lambda_2^*])\sinh[\theta\lambda_2^*]+\\((-\cos[2\beta+\theta(\lambda_2-3)]+\cos\gamma\cos[2\beta+\theta(\lambda_2-1)])\cosh[\theta\lambda_2^*]\sin[\log[r]\lambda_2^*]+\\\cos[\log[r]\lambda_2^*](\sin[2\beta+\theta(\lambda_2-3)]-\cos\gamma\sin[2\beta+\theta(\lambda_2-1)])\sinh[\theta\lambda_2^*])\lambda_2^*)+\\\lambda_2(\cosh[\theta\lambda_2^*]((-\cos[2\beta+\theta(\lambda_2-3)]-2\kappa\cos[\theta(\lambda_2-1)])\sin[\log[r]\lambda_2^*]-\\\cos[2\beta+\theta(\lambda_2-1)]\cos[(2\pi-\gamma)\lambda_2]\cosh[(2\pi-\gamma)\lambda_2^*]\sin[\log[r]\lambda_2^*]+\\\cos[2\beta+\theta(\lambda_2-1)]\cos[\log[r]\lambda_2^*]\sin[(2\pi-\gamma)\lambda_2]\sinh[(2\pi-\gamma)\lambda_2^*])+\\(\cos[(2\pi-\gamma)\lambda_2]\cos[\log[r]\lambda_2^*]\cosh[(2\pi-\gamma)\lambda_2^*]\sin[2\beta+\theta(\lambda_2-1)]+\\\cos[\log[r]\lambda_2^*](\sin[2\beta+\theta(\lambda_2-3)]+2\kappa\sin[\theta(\lambda_2-1)])+\\\sin[2\beta+\theta(\lambda_2-1)]\sin[(2\pi-\gamma)\lambda_2]\sin[\log[r]\lambda_2^*]\sinh[(2\pi-\gamma)\lambda_2^*])\sinh[\theta\lambda_2^*]+\\((2\cos[2\beta+\theta(\lambda_2-3)]-2\cos\gamma\cos[2\beta+\theta(\lambda_2-1)])\cos[\log[r]\lambda_2^*]\cosh[\theta\lambda_2^*]+\\(2\sin[2\beta+\theta(\lambda_2-3)]-2\cos\gamma\sin[2\beta+\theta(\lambda_2-1)])\sin[\log[r]\lambda_2^*]\sinh[\theta\lambda_2^*])\lambda_2^*)\end{array}\right\}\quad(A.3)$$

List of Publications

The following publications have been made using the present work.

International Journals

1. **Pranjol Paul**, **K. S. R. Krishna Murthy** and **Debabrata Chakraborty**, A strain gage technique for mode I notch stress intensity factor of sharp V-notched configurations, *Theoretical and Applied Fracture Mechanics* (2018), 94, 57–70.
2. **Pranjol Paul**, **K. S. R. Krishna Murthy** and **Debabrata Chakraborty**, A finite element simulation for notch stress intensity factors of sharp center V-notched tensile configuration using strain gauge technique, *International Journal of Computational Materials Science and Surface Engineering* (2023), 11, 272–287.
3. **Pranjol Paul**, **K. S. R. Krishna Murthy** and **Debabrata Chakraborty**, Experimental studies on the extent of 3D and 2D stress-strain states at sharp V-notches, *Theoretical and Applied Fracture Mechanics* (2024), 129, 104199.
4. **Pranjol Paul**, **K. S. R. Krishna Murthy** and **Debabrata Chakraborty**, Experimental determination of mode I notch stress intensity factors using valid strain gage locations, *Theoretical and Applied Fracture Mechanics* (2024), 133, 104573.

Conferences

1. **Pranjol Paul**, **K. S. R. Krishna Murthy** and **Debabrata Chakraborty**, Effect of material properties on optimal radial strain gage locations in sharp V-notched configurations, *3rd International Conference on Design, Analysis, Manufacturing and Simulation (ICDAMS-2018)*, *Chennai, Saveetha University, Chennai, Tamil Nadu, India, 6th -7th April 2018*.
2. **Pranjol Paul**, **K. S. R. Krishna Murthy** and **Debabrata Chakraborty**, Influence of the notch length on the optimal radial location of strain gage in a single edged notched plate, *1st International Conference on Emerging Trends*

in Mechanical Engineering (ICETME-2018), JNTUA, Ananthapurama, Andhra Pradesh, 20th -22nd December 2018.

3. **Pranjol Paul**, **K. S. R. Krishna Murthy** and **Debabrata Chakraborty**, A two-dimensional numerical case study for approximation of notch stress intensity factor of sharp V-notched plates under uniaxial tension, *12th International Conference on Structural Integrity and Failure (SIF2021), "Advances in Failure Analysis", Monash University, Melbourne, Australia, 5th -8th December 2021*.
4. **Pranjol Paul**, **K. S. R. Krishna Murthy** and **Debabrata Chakraborty**, Mode-I notch stress intensity factors for sharp center V-notched tensile configuration using strain gage technique: a numerical assessment, *International Conference on Advanced Materials and Computational Methods in Mechanical Engineering (ICAMCMME–2022), Osmania University, Hyderabad, Telangana, 11th -12th November 2022.*

Book Chapters

1. **Pranjol Paul**, **K. S. R. Krishna Murthy** and **Debabrata Chakraborty** (2020). Influence of the Notch Length on the Optimal Radial Location of Strain Gage in a Single Edged Notched Plate. In: Vijayaraghavan, L., Reddy, K., Jameel Basha, S. (eds) *Emerging Trends in Mechanical Engineering*. Lecture Notes in Mechanical Engineering. Springer, Singapore, https://doi.org/10.1007/978-981-32-9931-3_53.

About the Author

Mr. Pranjol Paul was born to Mr. Bivash Chandra Paul and Ms. Annapurna Paul in the year 1983. He completed his Class-X and Class-XII from Central Board of Secondary Education in 1999 and 2001 respectively securing 1st division in both examinations. He completed his Bachelor of Engineering in Mechanical Engineering securing 1st class from Jorhat Engineering College (then affiliated to Dibrugarh University) in the year 2005. During 2005-2008, he worked as an Assistant Project Engineer under R&D projects of Prof. D. Chakraborty and Prof. R. Tiwari in the Department of Mechanical Engineering, IIT Guwahati. Later in 2008, he joined as a Scientific Officer in the Department of Mechanical Engineering, IIT Guwahati and has been working since then. He got enrolled in the PhD programme in the Department of Mechanical Engineering, Indian Institute of Technology Guwahati as a part-time research scholar in the year 2010 and has been a PhD student during 2010-2024. His areas of academic interest are stress-strain analysis of isotropic materials using strain gages and fracture mechanics.